Surface Characterisation
of
Semiconductor Materials.

by

Linda Hart

A thesis submitted for the degree of
Doctor of Philosophy
of the
University of Warwick

June 1990

Abstract

Several well-established x-ray characterisation techniques have been developed to obtain high resolution for applications where high strain sensitivity and surface sensitivity are important. X-ray methods are compared with other characterisation methods and a range of x-ray techniques is reviewed. The double-axis diffractometer and its capabilities are described. Dynamical x-ray diffraction theory for distorted crystals, and the theory of diffuse scattering from randomly distributed defects are reviewed. X-ray reflectivity theory is also covered.

Several complementary characterisation techniques have been developed: Double-axis diffractometry using a four-reflection beam conditioner to measure surface scattering in the rocking-curve tails, topography using highly strain sensitive conditions at grazing incidence, with both a conventional x-ray source and synchrotron radiation, and energy dispersive reflectometry using a high-energy x-ray source. A range of samples has been characterised, including silicon wafers machined and polished under different conditions and from different manufacturers, silicon epiwafers, and ion implanted silicon.

In the rocking-curve analysis, modelling and simulation were used to determine the residual surface strain-depth profiles. Silicon wafers polished using a mechanical-chemical technique were found to have a lattice expansion of 4 to 8 parts per million near the surface, decreasing linearly to zero at up to one micron depth. Topography was used to detect strains of order 10^{-7} in polished silicon wafers. Strains were measured at the edges of polished areas which had been etched away, enabling strain relaxation. Energy dispersive reflectometry enabled determination of surface roughness of polished silicon wafers, down to Ångstrom resolution.

The techniques developed can be used widely in the characterisation of semiconductor materials. Rocking-curve analysis in particular is an extremely useful tool for the assessment of wafer quality and monitoring and development of the wafer production process.

Acknowledgements

Firstly, I would like to thank Prof. Keith Bowen for being an excellent supervisor! I would also like to thank Dr. Graham Fisher for the supply of samples, assistance with the reflectivity experiments and many useful discussions.

I am grateful to Prof. M. Hart for all his helpful advice and for the use of the high energy x-ray source at Manchester University, and to Dr. Stewart Cummings for help with the reflectivity experiments.

I would like to thank Prof. Brian Tanner for the use of the simulation program at Durham University and for the ion implanted samples, and Dr. Stephan Green for his help with the simulations. I gratefully acknowledge Dr. Simon Miles for the use of his reflectivity simulation program.

I am also grateful to Dr. Charles Thomas and Dr. Mike Capano for their help with the topography at Daresbury Laboratory, and to Dr. Ian Kirkman for the densitometer traces.

I would like to thank Dr. Stuart Smith for the useful discussions, and the technical staff of the materials and metrology areas in the Engineering Department, particularly Chris Fountain, Steve Wallace, Bob Bridgeland and Dave Robinson.

I am grateful to Alan Woods of Whickham Ion Beam Systems for the implantaton of the silicon and aluminium samples.

I would like to thank Prof. Linn Hobbs for arranging my visit to M.I.T. Financial support from the Science and Engineering Research Council, the University of Warwick and Prof. M. Hart is gratefully acknowledged.

I would also like to thank Mrs. S.M. Hart for lending me her car so that I could work late into the night.

Finally, I would like to thank Henry Bloomfield, without whom I would never have finished writing this thesis.

Contents

Chapter 1

1. Introduction.

As semiconductor device technology develops, the processes involved require increasingly high quality of semiconductor wafers. It is therefore relevant to investigate even the highest-quality wafer production processes, to assess the resultant material quality and to determine paths for its further improvement. Electronic device performance depends on the quality and homogeneity of the semiconductor wafers used. The surface and sub-surface, where device fabrication takes place, are particularly important.

It is useful to have a number of complementary characterisation techniques available for the assessment of material quality. X-ray methods are non-destructive and may therefore be combined with other methods (optical, electrical, etc.) and used for quality control. It is possible to characterise a wide range of surface properties using several complementary techniques. X-ray diffractometry (rocking curve analysis) gives average strain-depth profiles, down to nanometre resolution, and an indication of dislocation density and damage. Defect type, size and concentration can be determined from diffuse scattering intensity. X-ray topography of the near-surface region enables determination of the distribution of strains, misorientations and defects. X-ray reflectometry can be used to determine surface layer density, thickness and interface roughness down to the Ångstrom level.

In Chapter 2, the theory of the double-crystal diffractometer, and dynamical diffraction theory and its application to the study of distorted crystals are treated. Chapter 3 is a review of diffuse scattering theory for crystals with randomly distributed defects. Chapter 4 covers x-ray reflectivity theory. Several techniques are applied to the characterisation of commercial silicon wafer surfaces. These are already of very high quality and require methods with extreme sensitivity to strain and surface properties. General experimental procedures are described in Chapter 5. In Chapter 6, results of

high resolution double-crystal rocking-curve analysis are reported. The rocking curves are analysed using simulations incorporating strain-depth profiles, and diffuse scattering, which is treated in detail in Chapter 3. Highly strain and surface sensitive topography, using both conventional and synchrotron radiation is described in Chapter 7. In Chapter 8, an energy dispersive x-ray reflectometry technique is described.

The characterisation techniques proposed can be applied to a wide range of semiconductor materials, including Si, GaAs, InP, epitaxial layers, ion implanted and mechano-chemically polished wafers. Examples of several applications are given, but the main body of experimental work is concentrated on the detailed survey of residual surface strain or damage caused by polishing of silicon wafers. This includes the comparison of wafers in various stages of the polishing process and from a number of different manufacturers.

1.1 Semiconductor materials.

Silicon, used widely for VLSI integrated circuit memory chips for microprocessors, is now grown to a very high perfection. Most other bulk crystals grown for the electronics industry are much less perfect. These include III-V compounds such as GaAs, InP and InSb, II-VI compounds such as CdTe, and lithium niobate, garnets, sapphire and quartz. The growth of heteroepitaxial layers can be used to obtain precisely controlled electrical or magnetic properties. These include electro-optic devices for use in fibre optic communication systems. Examples of epitaxial layers grown for laser structures, where the band gap is precisely engineered, are InGaAsP on InP, AlGaAs on GaAs and CdHgTe on CdTe.

The techniques developed in this thesis were tested on silicon, since highly perfect silicon crystals are the most widely available. Silicon is also used to make x-ray optical elements, such as beam conditioners for use with synchrotron radiation sources, and to make micromechanical devices, such as miniature cantilever beams in pressure transducers and accelerometers (Petersen, 1982; Angell, Terry and Barth, 1983). It is

therefore important to investigate the processes by which silicon components and wafers are produced.

1.2 Machining and polishing processes.

Silicon single crystals are grown either by slow pulling from the melt (Czochralski) or by progressive melting and freezing of a small zone moving along a polycrystalline rod (float-zone). Crystals are now grown to 6" (15cm) diameter for use in the electronics industry.

Silicon is very strong but brittle and can be machined with diamond. A circular diamond saw, a band saw or a wire saw can be used, either with embedded diamond particles, or using an abrasive slurry. Material is removed under high loads by cracking and chipping (Stickler and Booker, 1963; Puttick and Shahid, 1977). In general, if material is removed by chipping, few partial cracks remain and the residual strain is low. This depends on the direction of abrasion. For (111) silicon, chip formation is greatest for $[11\bar{2}]$ directions and least for $[\bar{1}\bar{1}2]$ (Badrick et al, 1977). The resulting surface is plastically deformed and distorted and may contain cracks and dislocations. The mechanism for material removal and surface damage caused by diamond machining has been investigated by Smith (1990). Sawing damage is tens of microns thick and must be removed by lapping, polishing and etching. Ion beam milling can be used to give a virtually damage free surface.

Lapping is used to obtain a flat surface. A coarse abrasive such as 20 μm silicon carbide is used, in either free rolling or fixed particle abrasion. The resulting depth of damage is typically several microns. However, the residual strain after lapping may be greater than that after cutting (Chapter 6). Abrasion results in the formation of cracks or dislocations. This depends on the abrasive particle size, which determines whether material is removed by a brittle or ductile fracture mechanism (Puttick, Shahid, Hosseini, 1979).

Polishing uses smaller abrasive particles. Material is removed by the generation and movement of dislocations, leading to plastic deformation and shearing. Silicon can be polished by hand using diamond paste, down to 0.25 μm particle size, on a cloth-faced wheel, or alumina, down to 0.05 μm particle size. The damage depth is a few tens of nanometres (Johansson, Schweitz and Lagerlöf, 1989).

Commercial silicon wafers are polished using alkaline (pH 8.5-11) colloidal silica (marketed under the tradenames Syton and Nalco), on a porous polyurethane pad. Colloidal silica polishing slurries are concentrated aqueous suspensions of silica with particle size about 0.05 μm. The addition of potassium hydroxide stabilises the suspension (preventing coagulation) and combines free abrasive lapping with chemical polishing so that the silica particles abrade the native oxide, the alkali attacks the silicon underneath, the oxide regrows and the cycle repeats itself until the surface becomes flat and highly reflective. This is called mechanical-chemical polishing and it results in a very low level of residual surface strain and damage. This is the main subject of investigation in Chapters 6 to 9.

If the silicon is cut into complex shapes, such as multiple reflection beam conditioners, it cannot be lapped or polished so easily. Machining damage in silicon can then be removed by etching in 5% hydrofluoric acid in nitric acid. GaAs and InP can be etched in bromine in methanol.

Silicon wafers go through a number of processes- cutting with an inside diameter saw; lapping flat; etching to remove damage and, finally, polishing and cleaning. (001) silicon wafers can be cleaved along (110) planes using a diamond scribe. There are two main stages in the polishing process- a rough polish for stock removal (a few tens of microns) and a final polish for surface finish (removal of about a micron). The wafers are typically polished on one side, using an alkaline colloidal silica on a polyurethane pad. Polishing removal rates range from 0.1 to 10 microns per minute, depending on the temperature, pressure, colloidal silica and polishing pad. These factors may also affect

the final residual strain and damage in the wafer surface. This is investigated in Chapter 6.

1.3 Review of characterisation techniques.

A range of x-ray techniques, including diffractometry, topography and reflectometry, will be reviewed in application to surface characterisation of semiconductor materials. Several other (non x-ray) techniques will first be mentioned briefly, in order to give a general overview of characterisation methods.

Techniques for surface strain analysis include scattering of optical, x-ray, electron and ion beams. The penetration of a particular beam into a material depends on its interaction with the atoms and hence its absorption. Comparing x-ray and electron diffraction, x-rays have the lower absorption and hence higher penetration. X-ray diffraction (XRD) can be used non-destructively to characterise large, thick samples, such as semiconductor wafers up to several inches in diameter. For transmission electron microscopy (TEM), samples must be sectioned and thinned, as the penetration depth of electrons is less than a micron. The main advantage of using electrons is that they can be focussed to give a much higher spatial resolution than x-rays (~ 1nm for electrons compared to ~ 1μm for x-rays). X-ray topography can be used to image large-scale lattice distortions and deformations and long-range strain fields from defects. However, if the defect density is high, the images overlap. TEM can be used to image much smaller defects at higher defect densities, but with much lower strain sensitivity. X-ray and electron diffraction techniques are therefore complementary.

The strain sensitivity of a diffraction technique depends on the range of reflection or rocking curve width. Electron diffraction rocking curves are broad (~1°), while x-ray double-crystal rocking curves can be extremely narrow (~1 arc second), giving high strain sensitivities of 10^{-4} to 10^{-5}. The strain sensitivity is therefore much higher for XRD than for TEM, as shown in figure 1.1, which compares various techniques for surface strain analysis (after D.K. Bowen, unpublished).

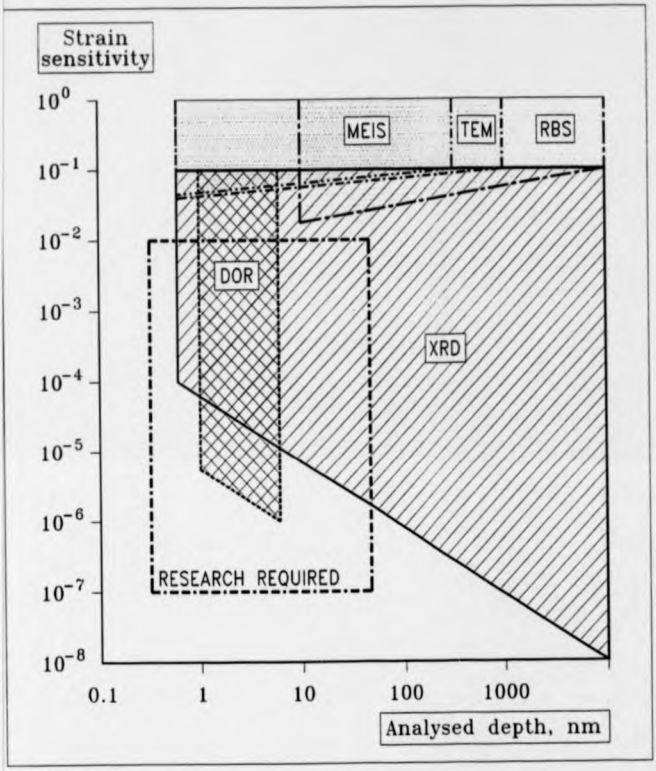

Fig. 1.1: Techniques for surface strain analysis

The techniques are x-ray diffraction (XRD), differential optical reflectometry (DOR), Rutherford back-scattering spectroscopy (RBS), medium energy ion scattering (MEIS) and transmission electron microscopy (TEM).

Rutherford back-scattering spectroscopy (RBS) and medium energy ion scattering (MEIS) are both techniques used to measure impurity depth profiles. The sample is bombarded with an ion beam and the energy distribution of back-scattered ions is measured. If the sample is aligned in a low index direction, channelling of ions occurs along lattice planes. The back-scattered intensity from lattice atoms in the direction of a lattice row is therefore a minimum due to ion blocking. An angular shift in the position of the minima gives a direct measure of lattice strain (Feldman, Mayer and Picraux, 1982; Kavanagh et al, 1988). Channelling measurements enable determination of strain and damage depth profiles and lattice location of impurities. The strain sensitivity is relatively low.

Differential optical reflectometry (DOR) is a technique which can be used to characterise surface layers down to a thickness of nanometres. The strain sensitivity is relatively high (10^{-1}-10^{-6}). The difference between the reflectivities of two samples is measured using an oscillating light beam at near normal incidence, ranging through ultraviolet, visible and infrared light. This can be used to assess surface properties, including strain and damage (Hummel, 1983). Infra-red spectroscopy or imaging can be used to detect defects such as carbon and oxygen clusters, by absorption. Ellipsometry is an optical technique involving the measurement of polarisation of light reflected from a sample. It can be used to measure refractive index and hence electron density, giving information on surface properties. Optical techniques, like x-ray methods, are non-destructive.

Surface morphology can be measured by optical microscopy, scanning electron microscopy or engineering metrology.

1.3.1 Double-crystal x-ray diffractometry.

Double-crystal diffractometry is widely used for the characterisation of epitaxial layers. A plot of the change in diffracted intensity with angle, called a rocking curve, is obtained by rocking a sample crystal through the Bragg angle with respect to a perfect reference crystal. Rocking curve profiles are highly sensitive to variations in lattice parameter with depth in the top few microns of the crystal.

The interpretation of rocking curves is now well understood. For simple layer structures, the lattice parameter mismatch or strain between layer and substrate can be determined directly from the angular separation of peaks in the rocking curve. If the structure is more complicated, comparison with simulated rocking curves becomes necessary. Several methods for calculating theoretical rocking curves have been used. For thin, weakly diffracting layers, kinematical theory (Speriosu, 1981) may be used. Speriosu, Paine, Nicolet and Glass (1982) successfully modelled Si-implanted Si, Ge and GaAs with strained and damaged layers around 0.5 μm thick. Speriosu, Nicolet, Tandon and Yeh (1985) applied the theory to rocking curves of 0.25 μm AlGaAs layers on GaAs. Kyutt, Petrashen and Sorokin (1980) investigated boron-doped silicon using a semi-kinematical theory where diffraction in the bulk crystal was calculated using dynamical theory, and in the layer using kinematical theory. This has been applied by Tapfer and Ploog (1986) to III-V heteroepitaxial structures.

If the layer thickness is a significant fraction of the extinction depth of x-rays (several microns), dynamical theory must be used (Takagi, 1969; Taupin, 1964), taking into account multiple scattering of x-rays. Burgeat and Taupin (1968) used dynamical theory to calculate rocking curve profiles of boron and phosphorus diffused silicon. This theory was also successfully applied to diffused and doped epitaxial silicon by Fukuhara and Takano (1977) and to ion-implanted silicon by Larson and Barhorst (1980). Halliwell, Lyons and Hill (1984) extended this method to interpret rocking curves from III-V heteroepitaxial structures. Hill, Tanner, Halliwell and Lyons (1985) applied it to

single and multiple homogeneous layers, graded layers (with a lattice parameter gradient), and multilayers of alternating composition (superlattices).

Supplementary methods have also been used to verify the theoretical models. These include ion milling (Speriosu, 1981) and selective etching of surface layers (Bowen, Davies and Swaminathan, 1986), followed by engineering metrology of layer thickness.

1.3.2 Dislocation density and damage.

Crystals which are damaged or deformed contain dislocations which give rise to a mosaic crystal structure, composed of slightly misorientated crystal blocks. This causes a broadening of the rocking curve. X-ray line broadening has been treated by Stokes and Wilson (1944) and Warren and Averbach (1950). An estimate of an upper limit of the dislocation density is given by Hirsch (1956) as $w^2 / 9b^2$, where w is the rocking-curve width and b is the dislocation Burgers vector. Krivoglaz (1969) and Wilkens (1970) derived kinematical theories relating line broadening to dislocation size and density. Gani et al (1984) measured rocking-curve widths after successive etching to assess surface damage caused by diamond machining. Macrander et al (1986) and Brown et al (1989) measured dislocation density from rocking curve broadening and peak shift in epitaxial layers with large mismatches. Local changes in lattice strain and orientation cause peak shifts which can be mapped by taking rocking curves from different parts of the sample. A complete analysis of residual elastic strains is possible if a number of reflections from different lattice planes is measured (Mayo, Chaudhuri and Weissmann, 1983).

In rocking-curve simulation, atomic disorder or damage may be modelled by a Debye-Waller factor. This takes into account random displacements of atoms from their lattice positions, and causes a decrease in the diffracted intensity. If the damage varies with depth, the model must have several layers, each with a different strain and Debye-Waller factor. This was used by Speriosu (1981) to model strain and damage distributions in ion-implanted garnets, and by Cembali et al (1985) for Si-implanted

silicon. The Debye-Waller parameter was varied proportionally with strain. If the crystal is so damaged that it becomes completely amorphous, there is no diffraction from the damaged layer. Dislocation loop size and concentration may be related to strain and Debye-Waller parameter (Dederichs, 1973; Larson, 1974). This was used by Zaumseil et al (1987) to characterise dislocations in ion-implanted and annealed silicon. A number of ion-implantation processes causing lattice damage may be characterised by x-ray diffractometry (Servidori, 1987).

Etching can be used as a surface characterisation method, but it is destructive. Dislocation density can be measured by counting etch pits. Damage can also be assessed by measuring etching rates, which are sensitive to the state of polish of a surface (Ives and Leung, 1988). This method is described in Chapter 5.

1.3.3 Thin layer interference fringes.

Thin surface layers (less than a few microns thick) give rise to interference fringes in the tails of the Bragg reflection peak, with fringe spacing depending on layer thickness. These Pendellösung fringes were first observed by Batterman and Hildebrandt (1968) in thin silicon crystals. They were used to measure the thickness of garnet epitaxial layers by Stacy and Janssen (1974), GaAlAs layers by Bartels and Nijman (1978) and InGaAs layers by Macrander and Strege (1985). Multiple layers give rise to more complex interference effects and require fitting of theoretical simulations with experimental curves. Rocking curves from multiple layer structures with very thin layers have been simulated using dynamical theory by Chu and Tanner (1986), Fewster and Curling (1987) and Tanner and Halliwell (1988). Tapfer, Ospelt and von Känel (1990) were able to detect extremely thin layers of Ge on Si, down to a monolayer (Ångstroms) thick. They used double crystal diffractometry and a beam conditioner with two successive asymmetric reflections to produce an incident beam with extremely low divergence.

1.3.4 Asymmetric x-ray diffraction.

Symmetric reflections, where the Bragg planes are parallel to the surface, can be used to measure mismatch for layers thicker than 0.1 μm. For layers thinner than 0.1 μm, the layer peak intensity reduces and the peak broadens. Symmetric reflections only give information on strains perpendicular to the surface. Highly asymmetric reflections, where the Bragg planes are inclined at an angle to the surface, give enhanced layer intensity and narrower layer peaks (Tanner and Hill, 1986). Asymmetric reflections give information on strains both perpendicular and parallel to the surface. Lee, Bowen and Salerno (1987) measured rocking curves from GaAs on Si, with a misorientated substrate. They varied the glancing angle, and hence the penetration depth, by rotating a slightly miscut sample about its surface normal.

Epitaxial layers thinner than 200 Å have been measured using asymmetric reflections (Bates et al, 1988). The grazing angle may be tuned to very low values by using synchrotron radiation (Tanner and Hill, 1986), or with characteristic radiation, by using skew asymmetric reflections and rotating about the diffraction vector (Miles et al, 1989). Below 1° incidence, the specularly reflected wave becomes significant and the theory must be modified (Hartwig, 1978). Brühl, Pietsch and Lengeler (1988) used the semi-kinematical theory, taking account of refraction, to simulate rocking curves from single layers, with grazing angles down to 0.35°.

Several other grazing incidence techniques should also be mentioned here.

Grazing incidence x-ray diffraction.

Grazing incidence x-ray diffraction below the critical angle for total external reflection, in a plane parallel to the surface, is used to study surfaces and interfaces. X-ray total external reflection Bragg diffraction was first used by Marra, Eisenberger and Cho (1979) to measure variations in lattice parameter in thin layers of Al on GaAs. The angle of incidence is below the critical angle and the incident beam is specularly

reflected from the surface and simultaneously diffracted through an angle 2θ from planes perpendicular to the surface. Aleksandrov et al (1985) used this technique to measure thin amorphous layers on silicon. The change in diffracted intensity with grazing angle was measured, enabling detection of surface layers down to Ångstroms thick.

Grazing incidence asymmetric Bragg diffraction in a plane perpendicular to the surface has been used to analyse magnetic iron oxide thin films (Lim et al, 1987; Toney et al, 1988). Synchrotron radiation is used. The angle of incidence is fixed and the detector is scanned through 2θ in a plane normal to the surface to measure diffraction from Bragg planes inclined to the surface. The penetration depth is varied by changing the grazing angle. A similar technique, using a position sensitive detector, was applied to the analysis of ion-implanted and worn surface films (Pons et al, 1988).

1.3.5 X-ray topography.

Introduction.

X-ray topography may be used to image many different types of defects in single crystals, for a wide range of materials. X-ray topographs give high strain sensitivity (10^{-5} to 10^{-6}) but low spatial resolution (~ 1μm). In transmission topography, the bulk crystal is imaged, while in reflection, only the surface region is imaged. Penetration depth depends on the grazing angle, reflection and wavelength of radiation used. If the sample is deformed or distorted, single crystal or white radiation topography using synchrotron radiation may be applied. This gives a strain sensitivity of 10^{-4} or 10^{-5}. For the study of near perfect crystals, a much higher strain sensitivity is required. This is possible using double-crystal plane-wave topography.

White radiation topography.

Synchrotron radiation can be used in a wide range of x-ray topography experiments (Hart, 1975). White radiation topography may be applied to survey experiments or dynamic experiments because of the short exposures, enabling a large number of

topographs to be taken. Detailed strain analysis is possible, by using a number of different reflections. Interface dislocations in strained layers may be characterised using this method (Capano et al, 1990). White radiation topography can also be applied to the study of deformations in dynamic experiments (Dudley, Miltat and Bowen, 1984).

Section topography.

If a narrow slit is used in transmission topography, a section through the crystal can be mapped. If the crystal is perfect, interference fringes may be seen. If the crystal is strained or distorted, the interference fringes become more complex. These may be compared with theoretical simulations (Epelboin, 1988). Cui, Green and Tanner (1989) characterised precipitates in silicon using this method. If the crystal is highly defective or damaged, the fringes disappear (Patel, 1973). The thickness of a damaged surface layer may be measured using this method (Auleytner et al, 1980).

Anomalous Transmission.

In transmission, there are two waves in the crystal, the forward diffracted and diffracted beams, which interact to produce two wavefields, one with antinodes at the atomic planes, which is preferentially absorbed, and one with nodes at the atomic planes which is preferentially transmitted. This results in an increase in the transmitted intensity even if the crystal is relatively thick. If there are defects in the crystal, this anomalously transmitted intensity is reduced. This has been used by Patel (1973) for oxygen precipitates in heat-treated silicon and Kitano et al (1986) to show dislocations in GaAs.

Double-crystal topography.

Double-crystal topography can be used to measure very low lattice strains. Hart (1968) and Bonse and Hartmann (1981) measured lattice strains down to 10^{-8} in high quality float-zone crystals, using high order reflections and short wavelength radiation in the non-dispersive arrangement. If good quality reference crystals of the same material as the sample are not available, high strain sensitivity can only be achieved by using

multiple crystal beam conditioners to reduce the wavelength spread and angular divergence. Hashizume, Iida and Kohra (1975) used such a system to measure growth bands in garnets and lattice strains in lithium niobate crystals. Lattice tilts and dilations can be separated by taking topographs rotated by 180° (Kikuta, Kohra and Sugita, 1966; Tanner, Barnett and Hill, 1985). If the range of Bragg angles over the sample is greater than the rocking-curve width, only a narrow contour will be imaged. Multiple exposures can be taken at different angles to build up a Bragg angle contour map or zebra pattern (Renninger, 1962, 1965; Hart, 1981). Jenichen et al (1985, 1988) used a reference crystal of tuneable curvature for double-crystal topography of curved samples.

Synchrotron radiation has several advantages- high intensity, low divergence, and tuneable wavelength and polarisation. Reviews are given by Sauvage (1980) and Miltat and Sauvage (1984). Synchrotron radiation has been used to study misfit dislocations in a III-V epilayer and substrate (Petroff et al, 1980) and strains in GaAs crystals (Ishikawa, Kitano and Matsui, 1985). Ishikawa, Kitano and Matsui (1987) used triple-crystal topography to map areas of equal lattice spacing in Si-implanted GaAs wafers. Kitano et al (1987) used synchrotron radiation to take topographs of a 6" silicon crystal. They used grazing incidence below the critical angle to obtain high surface sensitivity.

In Chapter 7, the use of high order reflections in the non-dispersive geometry to obtain high strain sensitivity, together with grazing incidence for surface sensitivity is described. This is applied to the detection of residual surface strain in polished silicon wafers.

1.3.6 Triple-axis diffractometry.

X-ray scattering from very thin surface layers is found far from the Bragg peak, in the tails of the Bragg reflection curve (Afanas'ev et al, 1984). This may be measured using double or triple axis diffractometry. Triple axis techniques use either a slit or an analyser crystal in front of the detector to measure the diffracted intensity in a θ-2θ scan. For the measurement of scattering from surfaces, triple-crystal diffractometry has several

advantages over double-crystal. Much higher resolution and signal to noise may be obtained. This is necessary for the measurement of very thin surface layers. The lattice parameter variation, layer thickness and interface roughness may be determined using kinematical theory (Andrews and Cowley, 1985; Lucas et al, 1988). Interface roughness or atomic disorder is modelled using a Debye-Waller factor (Afanas'ev et al, 1986; Cowley and Ryan, 1987). Triple-crystal diffractometry removes the effects of sample curvature. It is also possible to map the scattering intensity around the Bragg reflection in two dimensions in reciprocal space (Iida and Kohra, 1979; Ryan et al, 1987). The main advantage of triple-axis diffractometry is that it can be used to separate dynamical diffraction from incoherent diffuse scattering (Eisenberger et al, 1972; Iida and Kohra, 1979). This can be used either to measure the dynamically diffracted intensity (Zaumseil et al, 1987) or to measure the diffuse scattering from defects (Lomov, Zaumseil and Winter, 1985).

Triple-crystal diffractometry requires rather long data collection times. The x-ray source can be a conventional sealed tube (Fewster, 1989), a rotating anode (Cowley and Ryan, 1987) or synchrotron radiation (Stevenson et al, 1988). It is unnecessary to use this technique unless dynamical and diffuse scattering must be separated. Double-crystal diffractometry may be used to measure scattering from surfaces if a multiple reflection beam conditioner is used to obtain high angular resolution and good signal to noise. In Chapter 6, the use of double-crystal diffractometry with a four-reflection beam conditioner, to characterise polished silicon wafers, doped epiwafers and ion-implanted silicon, is reported.

1.3.7 Diffuse scattering.

Diffuse scattering from randomly distributed defects may be measured using double- or triple- axis diffractometry. Diffuse scattering gives information on defect size, symmetry and concentration. This is especially useful when defects are too small to be resolved by topography. Diffuse scattering has been measured from defects in silicon

crystals (Patel, 1975; Iida, 1979) and lapped and polished silicon surfaces (Iida and Kohra, 1979; Kashiwagura, Harada and Ogino, 1983). Diffuse scattering will be discussed in detail in Chapter 3 and used in the rocking-curve analysis in Chapter 6.

1.3.8 X-ray reflectivity.

Near the critical angle for total external reflection, the penetration depth is very low. A plot of the change in reflectivity with angle or energy will give information on the variation of electron density with depth near the surface. Thin surface layers give rise to interference fringes (Kiessig, 1931), with fringe spacing and amplitude depending on layer thickness and density. The reflected intensity is inversely proportional to the scattering angle to the fourth power. Surface or interface roughness, or small variations in density, will change the gradient of the curve and smear out any interference fringes. By comparing experimental reflectivity curves with theoretical simulations, surface layer thickness and roughness may be determined for both crystalline and amorphous layers. Segmüller (1973) measured the thickness of amorphous silicon (a few thousand Ångstroms thick) on sapphire, using a double-crystal diffractometer with a slit in front of the detector. Cowley and Ryan (1987) used a triple-crystal diffractometer to measure surface oxide layers on silicon wafers, down to tens of Ångstroms thick. Lucas et al (1988) used triple-crystal reflectometry to characterise a heteroepitaxial single quantum well structure. They used a model with three layers of different thickness, density and interface roughness.

Most information on very thin surface layers is found a long way from the critical angle, where the intensity is low. Angle dispersive reflectometry therefore requires long data collection times. Naudon et al (1989) proposed an angle dispersive technique using a line source perpendicular to the sample and a position sensitive detector to measure the reflected intensity. The line source acts as a set of point sources at different angles of incidence, hence enabling measurement of the complete reflectivity curve, in a much shorter time.

X-ray reflectivity curves can be measured in either angle dispersive or energy dispersive modes. Bilderback and Hubbard (1982) used standard x-ray sources and a solid state detector to measure energy dispersive reflectivity curves up to 50 keV, for a range of materials. An energy dispersive technique using a high-energy x-ray source to measure reflectivity curves up to 80 keV is described in Chapter 8.

Chapter 2

2. X-ray diffraction theory.

2.1 Introduction.

X-rays are diffracted from planes of atoms in a crystal lattice according to Bragg's law

$$n\,\lambda = 2\,d\,\sin\theta \qquad 2.1$$

where λ is the wavelength, θ is the Bragg angle and d is the interplanar spacing.

For cubic crystals,

$$d = \frac{a}{\sqrt{h^2 + k^2 + l^2}}$$

where a is the lattice parameter of the unit cell and h,k,l are the Miller indices of the Bragg reflection planes.

Bragg's law states that the condition for constructive interference to occur is that the path difference between rays diffracted from adjacent planes is equal to a whole number of wavelengths (equation 2.1).

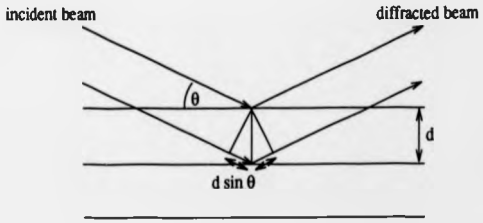

Figure 2.1 Bragg condition for constructive interference.

If a crystal is rocked through the Bragg angle and the diffracted intensity plotted, the shape of the resulting "rocking curve" will depend on the perfection of the crystal

lattice. Unfortunately, single crystal rocking curves are broadened by source size, beam divergence and wavelength spread. The auto-correlation, a double crystal rocking curve, in the non-dispersive setting, can be used to overcome these effects and is easily measured. The x-rays are first reflected from a "perfect" reference crystal set at the Bragg angle and then from the sample crystal, which is rotated through the Bragg angle to obtain a rocking curve. This is called double-crystal diffractometry and is widely used for the characterisation of semiconductor epitaxial layers.

2.2 Theory of the double-crystal diffractometer.

The theory of the double-crystal diffractometer is given in Compton and Allison (1935) and Pinsker (1978). Some important results are presented here. A simple graphical representation of multiple-crystal diffraction is the DuMond diagram (DuMond, 1937).

2.2.1 The DuMond diagram.

The DuMond diagram is a plot of Bragg's law (wavelength versus Bragg angle) over the range of Bragg reflection, as shown in figure 2.2(a). The plot is part of a sine curve with line width representing the rocking curve width. In double-crystal diffraction, by convention, the first crystal rotates the beam in a positive sense and if the second crystal rotates the beam in the opposite sense, this is called (+,–) geometry (figure 2.3(a)). If the two crystals have identical Bragg plane spacings, the DuMond diagram is as shown in figure 2.2(b). As the second crystal is rotated, the second curve slides over the first. When the crystals are parallel, the curves overlap and the Bragg condition is satisfied for both crystals for all wavelengths simultaneously. If the second crystal is only slightly displaced, no wavelengths are diffracted. This setting is therefore non-dispersive in wavelength.

The intensity of the double-crystal rocking curve is the area under the overlap as the second crystal DuMond diagram slides over the first. This is the correlation of the two

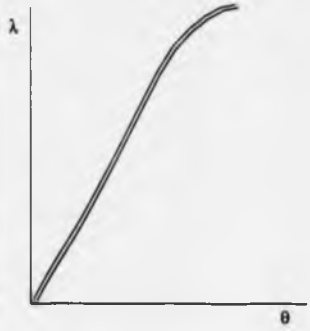

(a) DuMond diagram for first crystal.

(b) (+,–) non-dispersive setting.

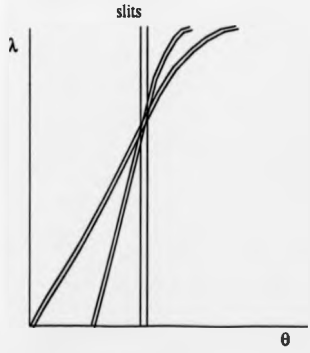

(c) (+,–) dispersive setting.

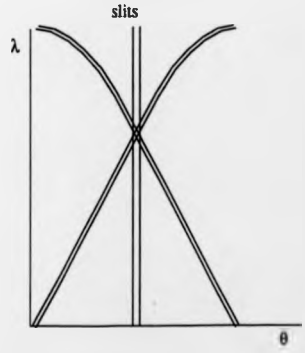

(d) (+,+) dispersive setting.

Figure 2.2 DuMond diagrams for double-crystal diffractometer.

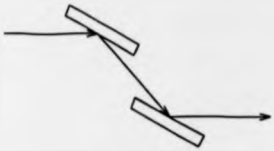

(a) (+,–) non-dispersive parallel setting.

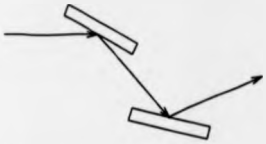

(b) (+,–) dispersive setting.

(c) (+,+) dispersive setting.

Figure 2.3 Double-crystal diffractometer settings.

Bragg reflection curves calculated from dynamical diffraction theory (see section 2.4). For the parallel (+,–) geometry, the double-crystal rocking curve is given by

$$I(\omega) = K \int_{-\infty}^{+\infty} R(\theta)\, R(\theta - \omega)\, d\theta \qquad 2.2$$

where $R(\theta)$ is the Darwin-Prins reflection curve for a perfect crystal, θ and ω are angular deviations from the reflecting positions of the first and second crystals and K is a

constant proportional to the power of the incident x-ray beam. $I(\omega)$ is about 1.4 times as wide as $R(\theta)$. (The correlation of two identical Gaussian curves would give a curve exactly $\sqrt{2}$ times wider.) The auto-correlation of $R(\theta)$ is symmetric even if $R(\theta)$ is asymmetric. In practice, separate contributions from both π and σ polarisation states are required.

Because the shape of the rocking curve is not affected by beam divergence or wavelength spread, rocking curves taken in the non-dispersive geometry can be very narrow (less than 1 arc second for perfect silicon using high order reflections and short wavelengths), giving high sensitivity to lattice strain. For this reason, all the experiments reported in this thesis were performed using the non-dispersive setting.

2.2.2 Wavelength dispersion.

If the two crystals are not identical, or have different Bragg plane spacings (figure 2.3(b)), the DuMond diagrams will have different slopes, as shown in figure 2.2(c). As the second crystal is rotated, diffraction occurs at different wavelengths. This setting is therefore dispersive in wavelength. In practice, the collimation defines the angular range and both crystal curves must overlap with this for diffraction to occur. In experiments using characteristic wavelengths, the $K\alpha_1$ and $K\alpha_2$ lines are sometimes resolved in the rocking curve.

If both first and second crystals rotate the beam in the positive sense, this is called the (+,+) setting (figure 2.3(c)). The DuMond diagram in figure 2.2(d) shows that this setting is also dispersive in wavelength.

Wavelength dispersion broadens the rocking curve. The broadening may be calculated as follows.

Differentiation of Bragg's law (equation 2.1) gives the dispersion

$$\frac{d\theta}{d\lambda} = \frac{1}{\lambda}\tan\theta \qquad 2.3$$

The dispersion for two crystals is given by the sum of the partial derivatives

$$\frac{\partial\theta_1}{\partial\lambda} \pm \frac{\partial\theta_2}{\partial\lambda} = \frac{1}{\lambda}(\tan\theta_1 \pm \tan\theta_2) \qquad 2.4$$

where the upper sign corresponds to the (+,+) setting, the lower sign corresponds to the (+,–) setting and θ_1 and θ_2 are Bragg angles for the first and second crystals.

Therefore, the rocking curve is broadened by

$$\delta\theta = \frac{\delta\lambda}{\lambda}(\tan\theta_1 \pm \tan\theta_2) \qquad 2.5$$

which, for the non-dispersive case, is zero if $\theta_1 = \theta_2$.

2.2.3 Geometric broadening of the rocking curve.

Figure 2.4 shows the axes of rotation of a double-crystal diffractometer. The dispersion plane is the horizontal plane containing the incident and diffracted beams. The reference and sample crystals are mounted on the first and second rotation axes, ω, perpendicular to the dispersion plane. The axes in the dispersion plane are the tilt, χ, in the surface plane of the crystal (shown only for the sample crystal), and the azimuth, α, perpendicular to the surface plane of the crystal.

Tilt.

X-ray beams, in practice, have a finite angular divergence. If the Bragg planes in the first and second crystals are not parallel, divergent rays will be diffracted at different angles as the second crystal is rotated. This causes broadening of the rocking curve and a reduction in intensity. However, the integrated intensity (the area under the rocking curve) remains constant. The tilt angle must be adjusted to give maximum rocking curve intensity and minimum width. Several methods of tilt optimisation are described in Chapter 5.

An approximation to the tilt broadening for the non-dispersive setting is given by Schwarzchild (1928)

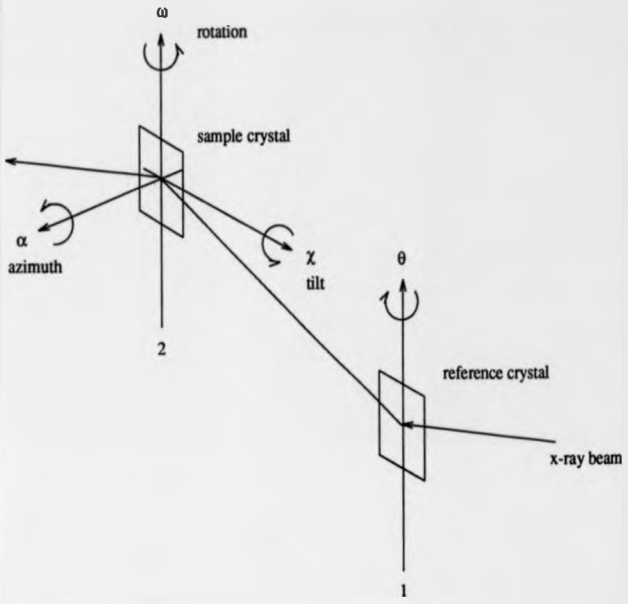

Figure 2.4 Double-crystal diffractometer axes.

$$\delta\theta = \chi\,\psi \qquad 2.6$$

neglecting higher powers of χ and ψ, where χ is the angle of tilt between the two crystals and ψ is the beam divergence perpendicular to the dispersion plane (usually called the vertical divergence if the dispersion plane is horizontal). Vertical divergence is defined as the height of the collimator slits divided by the distance between them. The effects of the approximation of equation 2.6 are explained by Schnopper (1965).

If the beam divergence is very low, such as with synchrotron radiation, the tilt broadening will be negligible. Tilt optimisation is then only necessary when measuring very narrow silicon rocking curves. In the dispersive setting, broadening due to tilt

misalignment is small compared to broadening caused by wavelength dispersion.

Divergence.

Vertical divergence alone has a small effect on the rocking curve width, given by Yoshimura (1985) for the non-dispersive setting

$$w = \frac{w_0}{1-(\psi^2/\cos^2\theta)^{1/2}} \qquad 2.7$$

where w is the rocking curve half width and w_0 is the half width for zero divergence.

Curvature.

Sample curvature broadens the rocking curve since the crystal will diffract over a wider angular range if the incident beam is wide compared to the sample curvature. A good approximation to the rocking curve can be obtained by correlating the theoretical curve with a rectangular function of width equal to the change in angle of incidence from one side of the beam to the other, given by

$$\delta\theta = \frac{x}{R\sin\theta} \qquad 2.8$$

where x is the width of the beam in the dispersion plane, R is the radius of curvature of the sample and θ is the angle of incidence (Bragg angle). The broadening can be reduced by using a small beam diameter (less than 1 mm) or, if possible, a thick sample which will have less curvature.

Surface unevenness.

Surface unevenness is modelled by dividing the surface into small regions with various inclinations, ϕ to the Bragg planes. The crystal lattice remains perfect. Bubáková, Drahokoupil and Fingerland used an optical method to measure the unevenness of a ground and etched crystal surface. They found a Gaussian distribution of ϕ, with standard deviation depending on the degree of surface unevenness. The theoretical Bragg reflection curve is multiplied by the Gaussian surface unevenness

curve. This results in a broadening of the rocking curve.

2.2.4 Interpretation of rocking curves.

Information on crystals with epitaxial layers may be obtained directly from the rocking curve. If there is a difference in diffraction angle between the surface layer and the substrate, caused either by mismatch (δd) or tilt ($\delta\theta$), there will be two peaks in the rocking curve.

Mismatch.

A change in the lattice parameter normal to the Bragg planes, will produce a change in the Bragg angle,

$$\frac{\delta d}{d} = -\delta\theta \cot\theta \qquad 2.9$$

This is the "experimental" mismatch,

$$m^* = \frac{\delta a}{a} = \frac{\delta d}{d}$$

The surface layer is constrained by the underlying crystal and can only be strained perpendicular to the surface, producing a tetragonal distortion. If the layer were removed from the substrate and allowed to relax, the mismatch would be

$$m = \frac{a_l - a_s}{a_s}$$

where a_l and a_s are the lattice parameters of the layer and substrate. This can be calculated from isotropic elasticity theory

$$m = m^* \frac{(1-\nu)}{(1+\nu)}$$

where ν is Poisson's ratio. For most semiconductors, $(1+\nu)/(1-\nu)$ is approximately equal to 2. For silicon in the [001] direction, $(1+\nu)/(1-\nu) = 1.77$.

For a single layer, mismatch can be determined directly from the rocking curve,

provided the layer thickness is greater than 0.5 μm and less than about 5 μm. If the mismatch is very small, or if it changes with depth, computer simulation of the rocking curve becomes necessary.

For a solid solution, the lattice parameter is linearly proportional to the concentration (Vegard's law).

If the mismatch is large, the strain will be relieved when the layer reaches a certain critical thickness, by the generation of misfit dislocations at the layer-substrate interface. This relaxation may be determined by measuring components of the strain parallel and perpendicular to the surface. An asymmetric reflection must therefore be used.

Tilt.

If the Bragg planes are misorientated with respect to the surface, the misorientation angle can be determined by rotating the sample through 180°, giving a shift in the Bragg peak position of twice the misorientation angle.

If the surface layer is tilted relative to the substrate, the layer peak will be shifted relative to the substrate peak. The mismatch may then be determined by rotating the sample through 180° and taking the average peak shift.

$$\delta\theta = (\delta\theta_0 + \delta\theta_{180}) / 2 \qquad 2.10$$

To find the tilt, the sample must also be rotated through 90°.

$$\delta\theta_0 - \delta\theta = \chi \cos\alpha \qquad 2.11a$$

$$\delta\theta_{90} - \delta\theta = -\chi \sin\alpha \qquad 2.11b$$

From equations 2.11 (a) and (b),

$$\tan\alpha = -\frac{(\delta\theta_{90} - \delta\theta)}{(\delta\theta_0 - \delta\theta)} \qquad 2.12$$

where α is the angle of rotation about the surface normal from the position of zero tilt, and χ is the angle of tilt between the layer and substrate. The tilt can be calculated by

substitution of equation 2.12 into equation 2.11 (a) or (b).

Layer thickness.

For a simple layer structure, the layer thickness may be determined from the relative integrated intensities (area under the peak) of the layer and substrate peaks.

If the layer is thin (less than a few microns), the outward going wave from the back surface of the layer is significant as well as the inward going wave, and interference occurs between the two wavefields in the crystal (section 2.4). Oscillations appear in the rocking curve tails as the angle of incidence changes. These are called Pendellösung fringes. For thick layers, the outward going wave is absorbed and there is no interference.

The thickness of the layer, t may be obtained from the angular separation of the Pendellösung fringes (Batterman and Hildebrandt, 1968).

$$\delta\theta = \frac{\lambda \sin(\theta + \phi)}{t \sin 2\theta} \qquad 2.13$$

where θ is the Bragg angle and ϕ is the angle between the Bragg planes and the surface. The fringe period is inversely proportional to the layer thickness. For very thin layers, the fringes appear a long way from the Bragg peak.

For multiple layers, the interference fringes from each layer are superimposed and more difficult to analyse. More complicated layer structures, such as graded layers (where the mismatch gradually changes with depth from the surface), produce complex interference patterns. Comparison with simulated rocking curves then becomes necessary.

2.2.5 Asymmetric reflections.

Symmetric reflections, where the Bragg planes are parallel to the surface, are only useful for measuring layers thicker than about 0.2 μm. Below this thickness, the layer peak becomes very broad and weak. If the mismatch is small, it may be difficult to

distinguish the layer peak from the tail of the substrate peak and long counting times may be necessary. Symmetric reflections only measure strains perpendicular to the surface. Asymmetric reflections, where the Bragg planes are inclined at an angle to the surface, measure strains both perpendicular and parallel to the surface.

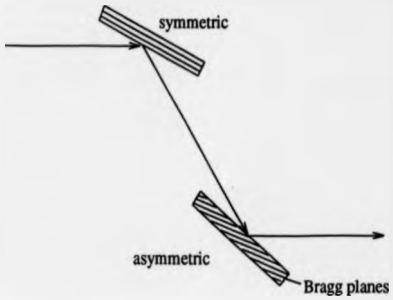

Figure 2.5 Asymmetric reflection.

If an asymmetric Bragg reflection is used, the extinction distance is reduced and the x-ray path length inside the crystal is increased, thus reducing the penetration depth by absorption. Diffraction from the surface layers is therefore enhanced. The lower the glancing angle, the more enhanced the diffraction from the surface layer is. For (001) silicon and CuKα radiation, the 044, 244 and 113 asymmetric reflections may be used, giving glancing angles of 8.4°, 8.8° and 2.8°. The beam path may be reversed to give either glancing incidence or glancing exit (figure 2.6). Glancing exit gives narrower rocking curves than glancing incidence.

Extreme grazing angles (less than a few degrees) may be obtained by several different techniques.

If the Bragg planes are misoriented with respect to the surface, the grazing angle, and hence the penetration depth, may be tuned by rotation of the crystal about its surface

Figure 2.6 Asymmetric reflections.

a.) Glancing incidence. b.) Glancing exit.

normal (Lee, Bowen and Salerno, 1987).

By using skew reflections (where the incident and diffracted beams are in a plane inclined at an angle to the surface), the grazing angle may be tuned by rotation of the sample about the normal to the diffracting planes. If a reflection is used where the angle between the surface and the Bragg planes, ϕ, is greater than the Bragg angle, θ, ($\phi > \theta$), the Bragg cone of possible incident and exit beams is embedded in the surface and it is possible to obtain grazing angles down to zero (Lyons and Halliwell, 1985; Miles, Green, Tanner, Halliwell and Lyons, 1988). However, as the grazing angle is reduced, the intensity decreases.

If synchrotron radiation is available, the wavelength may be tuned by choosing the Bragg angle to give a low angle of incidence or exit. The penetration depth can then be easily varied by slightly changing the Bragg angle. The high intensity of synchrotron radiation is also an advantage when using grazing incidence down to the critical angle for total external reflection, where the diffracted intensity is low.

2.2.6 Selection of experimental conditions.

Penetration depth and hence surface sensitivity may be varied by choosing a particular wavelength and reflection. A strong (low order) reflection and long wavelength will give a low extinction depth of several microns.

Asymmetric reflections reduce the extinction depth and also increase the path length

inside the crystal, thus reducing the penetration depth. Table 2.1 gives rocking curve widths, w for glancing incidence and exit (w_{gi} and w_{ge}), extinction depths, ξ_h and absorption lengths, $\sin(\theta-\phi)/\mu$ for (001) silicon and CuKα_1 radiation, calculated from dynamical theory (section 2.4). The structure factors used in the calculations include a Debye-Waller factor for silicon at room temperature (Aldred and Hart, 1973).

Table 2.1 Plane wave rocking curve parameters for (001) silicon with CuKα_1 radiation.

Si (001) CuKα1							
hkl	θ	ϕ	θ−ϕ	w gi(")	w ge(")	ξh(μm)	sin(θ−ϕ)/μ
113	28.06	25.24	2.82	9.30	0.57	6.60	3.49
004*	34.56	0.00	34.56	2.30	2.30	16.77	40.21
224	44.01	35.26	8.75	3.66	0.57	17.09	10.78
115	47.47	15.79	31.68	1.12	0.66	51.03	37.22
044	53.35	45.00	8.35	2.36	0.35	27.76	10.29

*(symmetric reflection)

Extreme grazing angles can only be obtained with characteristic radiation if skew reflections are used. The grazing angle can be tuned to very low if synchrotron radiation is available. If the angle of incidence is near the critical angle for total external reflection (0.2° for silicon at 1.5 Å wavelength), the penetration depth may be extremely low (down to nanometres).

To obtain high strain sensitivity, a high order reflection and short wavelength can be used to give a narrow, steep-sided rocking curve. The non-dispersive geometry should also be used. Table 2.2 gives rocking curve widths, w, for (001) silicon and MoKα_1 radiation.

Table 2.2 Plane wave rocking curve parameters for (001) silicon with MoKα_1 radiation.

Si (001) MoKα1							
hkl	θ	ϕ	θ–ϕ	w gi(")	w ge(")	ξh(μm)	sin(θ–ϕ)/μ
004*	15.14	0.00	15.14	1.21	1.21	12.50	174.14
115	19.84	15.79	4.04	1.53	0.19	17.40	47.00
008*	31.49	0.00	31.49	0.25	0.25	68.06	348.27
088	47.63	45.00	2.63	0.31	0.01	93.68	30.58
884	51.59	48.19	3.40	0.21	0.01	143.91	39.57

*(symmetric reflections)

A topograph taken on the flank of the rocking curve will show high contrast for small strains or misorientations.

If both high strain sensitivity and surface sensitivity are required, a compromise must be made. Instead of using a strong reflection with low extinction depth, a highly asymmetric reflection may be used to obtain a low penetration depth. However, the diffracted intensity then becomes rather weak, especially if the reflection is a high order one. If grazing incidence is used, a narrow, high intensity incident beam is required. This may be achieved by using the same reflection at the reference crystal, but in grazing exit.

2.3 Topography.

2.3.1 Introduction.

X-ray topography may be used to image defects in single crystals. This is similar to electron microscopy, but x-rays give much higher strain sensitivity (10^{-5} to 10^{-6}) and much lower spatial resolution (~ 1μm). An advantage of using x-rays is that they have a low absorption and can therefore be used non-destructively (without sectioning or thinning).

A topograph is a map of the diffracted intensity over the surface of a crystal. The crystal is set at the diffracting position and a photographic plate is placed in the diffracted beam. Figure 2.7 shows single-crystal topography for both transmission and reflection.

Figure 2.7 Single-crystal topography.

a.) Transmission.

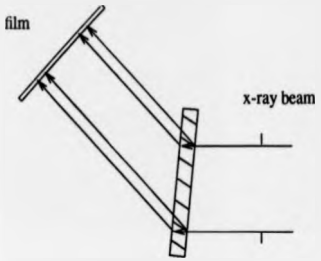

b.) Reflection.

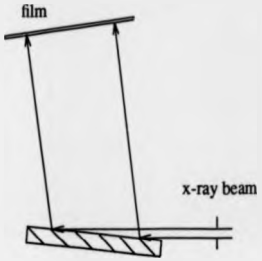

Near a defect, the crystal planes are slightly misorientated and the diffracted intensity changes. Several types of contrast occur in single crystal transmission topography, depending on the crystal thickness, t, and the linear absorption coefficient, μ, (Authier, 1970; Bowen and Hall, 1975).

For thin, weakly absorbing crystals ($\mu t \ll 1$), the divergent incident beam is kinematically (incoherently) scattered from the area around the defect and the intensity is increased. This is called a direct image.

For thick crystals ($\mu t \gg 1$), the misorientation around the defect will cause a reduction in the dynamically diffracted intensity. This is called a dynamical image.

In the intermediate range ($\mu t \sim 1$), two wavefields are present in the crystal and interference effects will occur. These are called intermediary images.

In reflection topography, the contrast is mainly from direct images. Topographs are usually shown as negatives, with high x-ray intensity giving dark images.

Synchrotron radiation is used for white radiation topography, where several different reflections can be recorded simultaneously. For high strain sensitivity, the sample crystal can be compared with a reference crystal, in double-crystal topography. Details of interpretation of defect contrast in topographs may be found in Tanner (1976) and Tanner and Bowen (1980). A wide range of defects in crystals will give contrast on topographs, including dislocations, stacking faults, precipitates, growth bands and swirl.

2.3.2 White radiation topography.

White radiation topography is similar to Laue photography, except that each Laue spot is broadened so that the whole crystal is imaged. White beam synchrotron radiation is used and diffraction occurs simultaneously for all allowed reflections, at different wavelengths and Bragg angles. Each Laue spot may consist of several superimposed harmonic reflections, which occur at the same Bragg angle for different multiples of wavelength. The theory of white radiation topography is treated by Miltat (1980).

The advantages of using white radiation topography are that exposures are short and several different reflections can be recorded on one photographic plate. Strains down to 10^{-4} or 10^{-5} can be detected. White radiation topography can be used for survey experiments, where large numbers of samples or a number of different reflections are required. It can also be used for dynamic experiments, such as in situ measurements of distortion in strained crystals (Bowen, 1988).

2.3.3 Double-crystal topography.

In double-crystal topography, the sample crystal is compared with a reference crystal, which should be of the highest quality available. Double-crystal topography is sensitive to strains in the range 10^{-5} to 10^{-8} and can therefore be used for the study of high-quality semiconductor crystals. It can be used to map variations in lattice parameter and tilt over an area of the crystal. If a wide beam is required to image a large area of the sample, an asymmetric reflection can be used at the reference crystal. Experimental set-

ups for double-crystal topography with symmetric and asymmetric reference crystals are shown in figure 2.8.

Figure 2.8 Double-crystal topography.

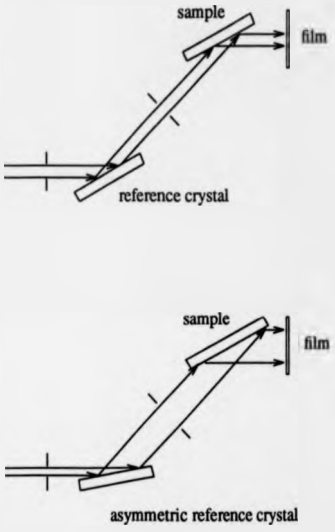

Grazing incidence may be used at the sample to increase the surface sensitivity and also to expand the beam to give better resolved images. Grazing exit cannot be used in topography because of the beam contraction it produces.

Both conventional x-ray sources and synchrotron radiation can be used for double-crystal topography. With synchrotron radiation, the exposures are much shorter and the divergence is low, giving high strain sensitivity. This also means that any defects in the reference crystal are imaged almost as well as those in the sample.

With conventional x-ray sources, images from defects in the reference crystal are blurred. The geometric resolution is given by $d = hb/a$ (figure 2.9), where h is the source

height, a is the source-specimen distance and b is the specimen-film distance. To obtain high resolution, the specimen-film distance should be as small as possible. The film should be perpendicular to the diffracted beam.

Figure 2.9 Geometric resolution.

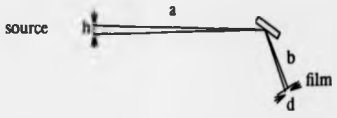

In the non-dispersive geometry, double images from the $K\alpha_1$ and $K\alpha_2$ lines are sometimes seen. This can be be avoided by using an asymmetric reflection at the reference crystal in order to decrease the divergence.

The spatial resolution on a topograph is also limited by the grain size of the film used. Ilford L4 nuclear plates give the highest resolution, of about 0.25 μm. Resolution decreases with increasing film speed.

Image contrast.

The main type of contrast observed in double-crystal topography is due to differences in orientation between the reference and sample crystals. Double-crystal topographs will show strain contrast and orientation contrast if there are local changes in lattice spacing or tilt. Contrast, or change in intensity is given by (Bonse, 1962)

$$\frac{\Delta I}{I} = k \left(\tan\theta_B \frac{\delta d}{d} + \underline{n}_1 . \underline{n}_2 \, \delta\theta \right) \qquad 2.14$$

where k = rocking curve slope

θ_B = Bragg angle

$\frac{\delta d}{d}$ = fractional change in Bragg plane spacing

$\delta\theta$ = tilt

$\underline{n}_g$ = unit vector parallel to goniometer axis

$\underline{n}_t$ = unit vector parallel to tilt axis

If the crystal is set on the steepest part of the rocking curve flank, the intensity can go up or down, depending on the sign of the strain. Images on opposite sides of the peak will have opposite contrast. To distinguish between tilts and dilations, two topographs are taken, rotated by 180° about the surface normal (Kikuta, Kohra and Sugita, 1966). Tilt and dilation can also be separated using triple-crystal topography (Ishikawa, Kitano and Matsui, 1987). A third reference crystal is used to define the direction of the diffracted beam reaching the film. If the third crystal is fixed and the sample rotated, a map of parts of the crystal with equal lattice spacing will be obtained. The third crystal may be set at several different positions on the rocking curve to obtain several maps, each at a different lattice spacing (Bragg angle).

For high strain sensitivity, the rocking curve should be very narrow and steep-sided. This is obtained by using high order reflections at short wavelengths. The highest strain sensitivity is obtained in the non-dispersive geometry, where the same reflection is used at the reference crystal and sample crystal. High order reflections are usually weak and, consequently the exposures are long (up to several days with a conventional x-ray source). Automatic servo control is then necessary to prevent drift off the flank of the rocking curve.

The tilt setting should be very carefully adjusted. If the sample is not correctly tilted with respect to the reference crystal, the sample may not diffract over the whole illuminated area and the image will be distorted.

If the sample curvature produces a range of Bragg angles larger than the rocking curve width, only a narrow contour the width of the rocking curve will diffract at a given Bragg angle. The sample may then be scanned or rotated in steps in order to build up a Bragg angle contour map or "zebra pattern" (Renninger, 1962, 1965).

In double-crystal topography, defect contrast is very high and defect images are broad. It can therefore be used to image individual dislocations in crystals with low dislocation densities. If the dislocation density is high, the images will overlap, but the tilts and dilations can still be mapped. Defects in the epilayer and substrate can be separated by taking topographs on each peak. However, the long range strain fields of dislocations may extend through both layer and substrate.

2.4 Dynamical theory of x-ray diffraction.

Introduction.

There are two general theories used to explain diffracted x-ray intensities.

The kinematical theory may be used if the scattering from each small volume element can be considered as being independent. This is applicable to crystals which are small, thin, imperfect or mosaic (composed of small, slightly misorientated crystal blocks). The kinematical theory predicts an integrated intensity proportional to the square of the structure factor.

The dynamical theory is used for large, perfect or near-perfect crystals where it becomes necessary to account for multiple scattering. There is a continual exchange of energy between the incident and diffracted beams, which must be considered as components of a total wavefield. Within the range of total reflection, the incident beam is rapidly attenuated as it passes through the crystal and the penetration depth is much smaller than that normally caused by absorption. This is known as primary extinction, an effect of dynamical diffraction which produces an integrated intensity proportional to the structure factor, much lower than that predicted by the kinematical theory.

Darwin (1914) was the first to consider dynamical diffraction for the Bragg case. Ewald and von Laue further developed the dynamical theory to include the Laue (transmission) and Bragg (reflection) cases and to describe the total wavefield inside the crystal. Introductions to dynamical theory may be found in James (1948, 1963), Zachariasen (1945), Pinsker (1978) and reviews by Batterman and Cole (1964), Authier (1970) and Hart (1971, 1980).

The basic problem is to solve simultaneously Bragg's law and Maxwell's equations in a periodic medium, the crystal. Bragg diffraction occurs when the Laue equation (2.15) is satisfied inside the crystal.

$$\underline{K}_0 + \underline{h} = \underline{K}_h \qquad 2.15$$

where $\underline{K}_0$ and $\underline{K}_h$ are the forward diffracted and diffracted wave vectors, 0 is the origin of the reciprocal lattice and $\underline{h}$ is the reciprocal lattice vector. The Laue equation states that inside the crystal there are two waves with difference in wave vector equal to the reciprocal lattice vector. Therefore, a standing wavefield is set up inside the crystal with the same spacing and orientation as the Bragg planes. The relative phases and amplitudes of the two coherent waves must also satisfy Maxwell's equations. When a set of solutions for possible waves in an infinite perfect crystal has been found, it is necessary to determine which of these are excited by the incident wave, and whether they are physically viable.

2.4.1 The periodic complex electric susceptibility.

The electron density at any point in the crystal, $\rho(r)$ may be represented as a Fourier sum over the reciprocal lattice.

$$\rho(r) = \frac{1}{V}\sum_{\underline{h}} F_h \exp(-2\pi i\, \underline{h}.\underline{r}) \qquad 2.16$$

where V is the volume of the unit cell and F_h is the Fourier coefficient, called the structure factor.

By inversion, the structure factor can be expressed as the Fourier transform of the electron density.

$$F_h = \int_V \rho(r) \exp(2\pi i\, \underline{h}.\underline{r})\, dV \qquad 2.17$$

The refractive index, n, the dielectric constant, κ and the electric susceptibility, χ, are all related to the electron density.

$$n^2 - 1 = \kappa - 1 = \chi = \frac{-4\pi e^2}{m\omega^2}\rho(r) \qquad 2.18$$

Since the electric susceptibility, χ is proportional to the electron density, it can be expanded in the same way, as a Fourier sum over the reciprocal lattice.

$$\chi = \sum_{\underline{h}} \chi_h \exp(-2\pi i\, \underline{h}.\underline{r}) \qquad 2.19$$

By comparison of equations (2.16) and (2.19), the Fourier coefficient of the electric susceptibility, χ_h can be related to the structure factor.

$$\chi_h = \frac{-\lambda^2 e^2}{\pi V mc^2} F_h = \frac{-\lambda^2 r_e}{\pi V} F_h \qquad 2.20$$

where r_e is the classical electron radius.

Calculation of χ_h shows that the refractive index for x-rays in crystals is less than unity by several parts in 10^6. χ_h appears in all the important results of dynamical theory, such as formulae for intensity, rocking curve width and extinction depth.

2.4.2 The structure factor.

The structure factor, F_h may be written as the sum of the atomic scattering amplitudes, f, over the n atoms in the unit cell.

$$F_h = \sum_n f_n \exp(2\pi i \, \underline{h}.\underline{r}_n) \qquad 2.21$$

If the x-ray frequency is near a resonant frequency for electrons (at an absorption edge) or if the crystal is a strong absorber, corrections must be added to the atomic scattering factors, so that f in equation (2.21) becomes $(f + f' + if'')$, where f' and f'' are the dispersion corrections due to resonance and absorption. The structure factor then becomes complex.

$$F_h = \sum_n (f_n + f'_n + if''_n) \exp(2\pi i \, [hx_n + ky_n + lz_n]) \qquad 2.22$$

where x, y and z are the coordinates of the atoms in the unit cell.

It can be shown that F_h and $F_{\bar{h}}$ are complex conjugates and equal if the crystal structure is centrosymmetric.

For silicon, which has the diamond cubic structure, for example

$$F_{111} = F_{\bar{1}\bar{1}\bar{1}} = -4\sqrt{2}\,(f_{111} + f' + if'')$$
$$F_{400} = F_{\bar{4}\bar{0}\bar{0}} = -8\,(f_{400} + f' + if'')$$
$$F_{440} = F_{\bar{4}\bar{4}\bar{0}} = +8\,(f_{440} + f' + if'')$$

2.4.3 The Debye-Waller factor.

If the atoms in the crystal lattice are displaced from the lattice sites, either dynamically by thermal vibration or statically by defects (point defects or dislocations) or atomic disorder, the atomic scattering factors must be multiplied by a Debye-Waller factor

$$(f + f' + if'') \exp(-B(\sin\theta/\lambda)^2) \qquad 2.23$$

where $B = 8\pi^2 \overline{u_n^2}$

$\overline{u_n^2}$ is the mean square displacement of a lattice point in a direction perpendicular to the reflecting planes. The mean square displacements are averaged over all the atoms in the crystal.

The thermal Debye parameter, B was measured by Aldred and Hart (1973) for silicon at room temperature, $B = 0.46$ Å^2. For the silicon 004 reflection, this gives a Debye-Waller factor, $\exp(-B(\sin\theta/\lambda)^2) = 0.94$. This is a significant correction factor, which is very often overlooked. Its effect is to slightly reduce the rocking curve width and intensity, as shown in figure 2.10. Thermal vibrations and static displacements also increase the intensity of diffuse scattering away from the Bragg peak. Thus, the total scattering remains constant. Diffuse scattering is treated in Chapter 3, using the kinematical theory.

2.4.4 Solution of Maxwell's equations.

The fundamental problem of dynamical theory is to find wave vectors in a crystal which satisfy both Maxwell's equations and Bragg's law.

Maxwell's equations are

$$\nabla \times E = -\frac{1}{c}\frac{\partial B}{\partial t} \qquad 2.24a$$

$$\nabla \times H = \frac{1}{c}\frac{\partial D}{\partial t} \qquad 2.24b$$

Figure 2.10. Effect of thermal vibrations at room temperature.

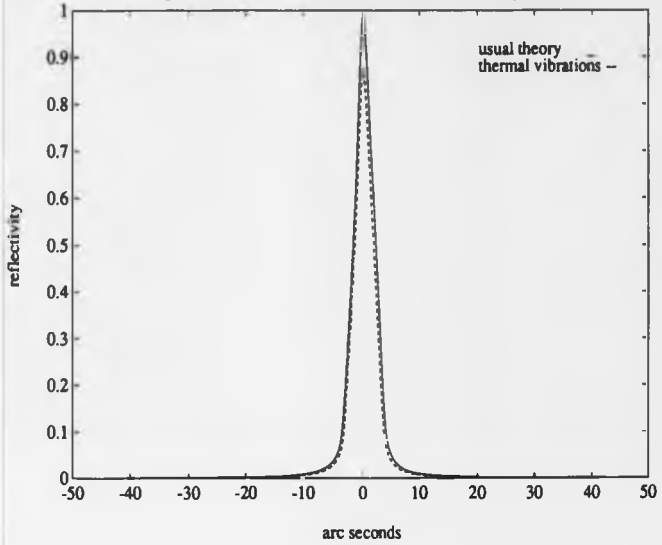

For Bragg reflection, the solutions are of the form

$$D = \sum_h D_h \exp(-2\pi i \, \underline{K}_h . \underline{r}) \qquad 2.25$$

These are known as Bloch waves, where $\underline{K}_h$ are the wave vectors and D_h are the amplitudes. When there is only one Bragg reflection, only two beams are considered, the forward diffracted and diffracted beams. Equation (2.25) then becomes

$$D = D_0 \exp(-2\pi i \, \underline{K}_0 . \underline{r}) + D_h \exp(-2\pi i \, \underline{K}_h . \underline{r}) \qquad 2.26$$

The solution of Maxwell's equations under these conditions (Batterman and Cole, 1964) gives

$$0 = [k^2(1+\chi_0) - \underline{K}_0 . \underline{K}_0] \, D_0 + [k^2 C \, \chi_{\bar{h}}] \, D_h \qquad 2.27a$$

$$0 = [k^2 C \chi_h] D_0 + [k^2(1+\chi_0) - \underline{K}_h \cdot \underline{K}_h] D_h \qquad 2.27b$$

where $k = \frac{1}{\lambda}$

and $C = 1$ for σ polarisation (electric field perpendicular to incidence plane)

$C = |\cos 2\theta|$ for π polarisation (electric field parallel to incidence plane)

For a non-trivial solution, the determinant of coefficients of D_0 and D_h (terms in brackets) must equal zero.

$\underline{K}_0$ and $\underline{K}_h$ are linked by the Laue equation (2.15). The differences between the wave vectors inside the crystal and the mean refracted incident beam are given by parameters α_0 and α_h, where

$$\alpha_0 = \frac{1}{2k} [\underline{K}_0 \cdot \underline{K}_0 - k^2(1+\chi_0)] \qquad 2.28a$$

$$\alpha_h = \frac{1}{2k} [\underline{K}_h \cdot \underline{K}_h - k^2(1+\chi_0)] \qquad 2.28b$$

Substituting into the determinant of coefficients of equations (2.27),

$$\alpha_0 \alpha_h = \frac{1}{4} k^2 C^2 \chi_h \chi_{\bar{h}} \qquad 2.29$$

This is the fundamental equation of the dispersion surface which determines the possible wave vectors and amplitudes inside the crystal.

2.4.5 The dispersion surface.

The dispersion surface is shown geometrically in figure 2.11. Outside the crystal, the wave vectors $\underline{K}_0$ and $\underline{K}_h$ meet at the Laue point, L, (in the Laue case) at the intersection between two reflection spheres of radius k around the reciprocal lattice points 0 and h. Inside the crystal, the wave vectors are corrected for the mean refractive index and the two spheres have radius $k(1+\chi_0/2)$. Near the intersection of the spheres, the wave vectors deviate from the mean refracted value and there is a range of possible solutions, all of which satisfy the Laue condition. For a particular position of an allowed

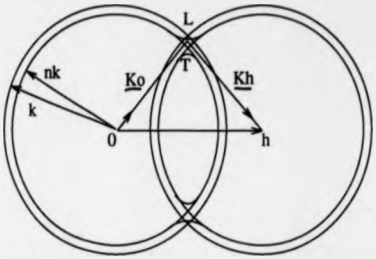

Figure 2.11 Construction of the dispersion surface for wave vectors Ko and Kh inside the crystal.

pair of wave vectors, the amplitude ratio, $R = D_h/D_0$ may be determined by

$$R = \frac{D_h}{D_0} = \frac{2\alpha_0}{C\,\chi_h\,k} = \frac{C\,\chi_h\,k}{2\alpha_h} \qquad 2.30$$

or

$$R^2 = \frac{\alpha_0}{\alpha_h}\,\frac{\chi_h}{\chi_{\bar{h}}} \qquad 2.31$$

Each tie point on the dispersion surface determines both the wave vectors and the amplitude ratio of the component plane waves of the Bloch wave (equation 2.26). Therefore, any wave propagating in the crystal is totally characterised by the tie point. Figure 2.12 shows the two branches of the dispersion surface (there are in fact two branches for each polarisation state). α_0 and α_h are the perpendicular distances from the tie point, T, to the spheres around 0 and h. The spheres may be approximated as planes and the dispersion surface is then a hyperboloid. The amplitude ratio, R is negative on branch 1 and positive on branch 2.

2.4.6 Excitation by external incident waves.

Since the Bragg (reflection) case is more widely used in double-crystal diffractometry than the Laue (transmission) case, only the Bragg case will be considered

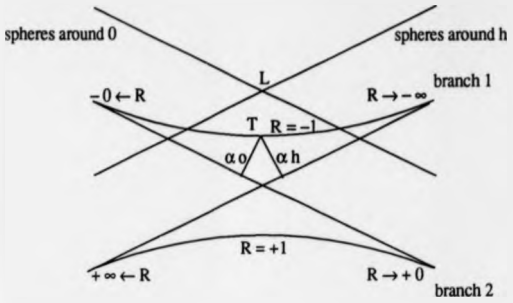

Figure 2.12 The dispersion surface.

here.

When the crystal is excited by a plane wave, the wave vector and amplitude must be matched outside and inside the crystal. Since the refractive index for x-rays is so close to unity, external reflection may be ignored, provided the angle of incidence is not near the critical angle for total external reflection. Therefore, to a good approximation, all the field vectors are continuous across the crystal surface and, in the Bragg case, the incident and diffracted amplitudes are identical outside and inside the crystal.

$$D_0{}^i = D_0 \qquad 2.32a$$

$$D_h{}^e = D_h \qquad 2.32b$$

where $D_0{}^i$ and $D_h{}^e$ are the incident and exit amplitudes of the external wave.

The difference in wave vectors inside and outside the the crystal must lie along the surface normal.

$$\underline{K}_0{}^i - \underline{K}_0 = qk\hat{n} \qquad 2.33a$$

$$\underline{K}_h{}^e - \underline{K}_h = -qk\hat{n} \qquad 2.33b$$

where $\underline{K}_0{}^i$ and $\underline{K}_h{}^e$ are the external incident and exit wave vectors, $\hat{n}$ is the surface

normal and q depends on the particular pair of allowed wave vectors. The boundary conditions imposed by the crystal surface govern the selection of tie points.

Figure 2.13 Dispersion surface and boundary construction.
Symmetric Bragg case.

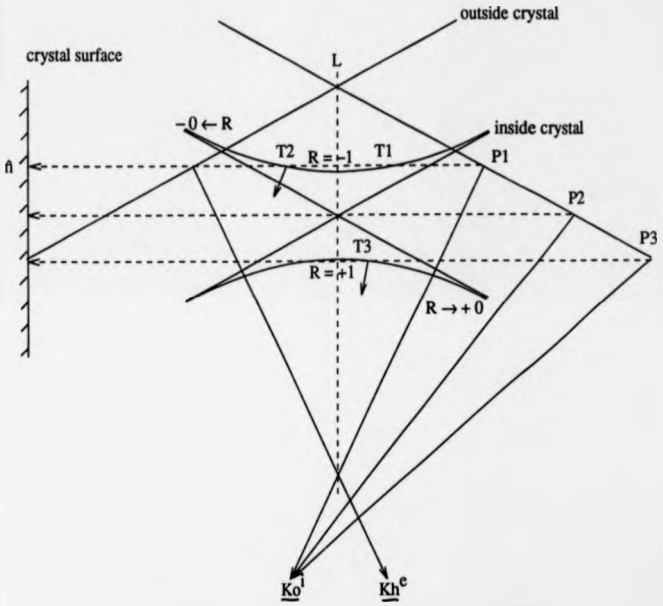

The boundary construction for the symmetric Bragg case is shown in figure 2.13. The crystal surface is perpendicular to the reciprocal lattice vector, $\underline{h}$. For the symmetric Laue case, the crystal surface would be parallel to $\underline{h}$. The incident wave vectors, $\underline{K}_0{}^i$ are drawn from the intersections with the surface normals, n, of the external reflection sphere around 0. Similarly, the exit wave vectors, $\underline{K}_h{}^e$ are drawn from the intersections with the sphere around h. As the tail of the incident wave vector moves away from L (the Laue

point), the angle of incidence increases. It can be seen that the angle of incidence at the centre of the reflection range is higher in the Bragg case than in the Laue case.

For an angle of incidence defined by point P_1, the tie points, T_1 and T_2 lie on the surface normal, n, on the same branch of the dispersion surface. The direction of energy flow is perpendicular to the dispersion surface so, at T_1, the energy flow is directed out of the crystal and at T_2, it is directed into the crystal. For thick crystals, only the point T_2 represents a physically viable solution, since the energy flow out of the crystal at T_1 is attenuated by absorption and would have to be impossibly large to reach the surface. Similarly, at point P_3, the tie point T_3 is excited since the energy flow is directed into the crystal. Therefore, for thick crystals, only tie points where the energy flow is into the crystal are excited. These correspond to the low-angle side of branch 1 and the high-angle side of branch 2. There is only one wavefield in the crystal.

For thin crystals, however, there is reflection from the back surface of the crystal, and the energy flow out of the crystal is large. In this case, two wavefields are excited in the crystal and interference may occur. As the angle of incidence changes, the tie-points move along the dispersion surface and Bragg case Pendellösung oscillations may be observed.

At point P_2, no tie points are selected and there are no propagating waves in the crystal since the energy flow is parallel to the Bragg planes. There is total reflection for the range of incident angles where the surface normal does not intersect the dispersion surface. The waves are then evanescent.

2.4.7 Bragg reflection curve for a perfect crystal.

The intensity of the diffracted beam, I_h / I_0, is given by

$$\frac{I_h}{I_0} = \frac{|D_h{}^e|^2}{|D_0{}^i|^2} = \frac{|D_h|^2}{|D_0|^2} = |R|^2 \qquad 2.34$$

From equation (2.30) for the amplitude ratio, R, it can be shown (Batterman and Cole,

Figure 2.14 Darwin-Prins Reflectivity Curve.

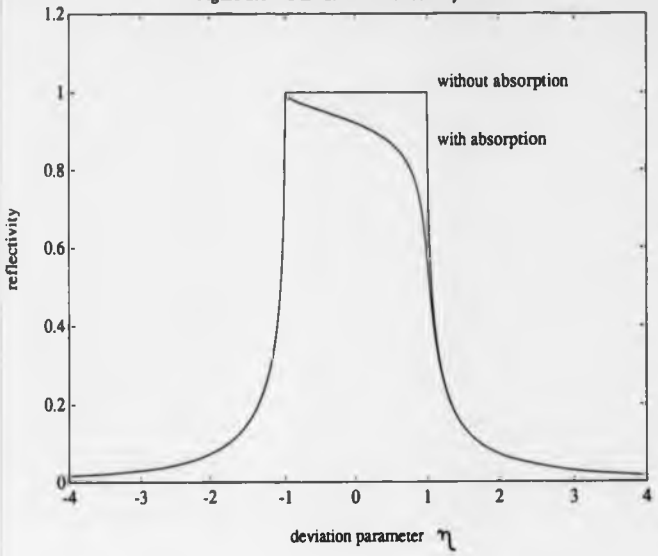

Figure 2.15 Reflectivity curves for both polarisations. Si 004 CuKα,

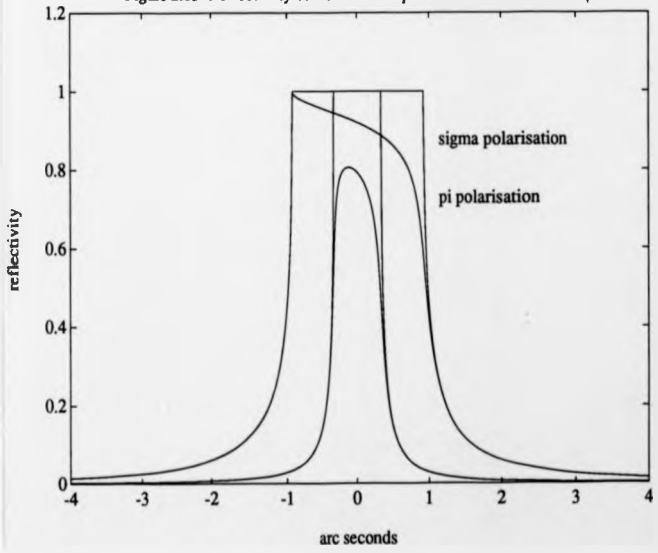

1964) that the intensity, I is given by

$$I = |R|^2 = |\eta \pm \sqrt{(\eta^2 - 1)}|^2 \qquad 2.35$$

where η is the deviation parameter from the exact Bragg angle,

$$\eta = \frac{\sin 2\theta}{C\sqrt{\chi_h \chi_{\bar{h}}}} \sqrt{\frac{\gamma_0}{|\gamma_h|}}\ \Delta\theta$$

and $\frac{\gamma_0}{|\gamma_h|}$ is the asymmetry factor of the surface,

where $\gamma_0 = \frac{1}{k}(\underline{K}_0.\underline{n})$ and $\gamma_h = \frac{1}{k}(\underline{K}_h.\underline{n})$.

The + sign in equation (2.35) is for branch 1 and the – sign is for branch 2.

In the range $-1<\eta<+1$, there is total reflection. If there is no absorption, the reflectivity is unity within this range, as shown in figure 2.14. This is the Darwin curve. With absorption, η becomes complex and anomalous dispersion occurs, where absorption is lower than usual for branch 1 of the dispersion surface and higher than usual for branch 2. The reflection curve becomes asymmetrical, as shown in figure 2.14 (the Darwin-Prins curve). This effect is explained in the following section. Figure 2.15 shows Bragg reflection curves for σ and π polarisations, for the silicon 004 reflection with $CuK\alpha_1$ radiation.

2.4.8 Anomalous dispersion.

From the Laue equation (2.15) and the equation for the Bloch wave (2.26), the intensity of the total wavefield in the crystal is

$$|D|^2 \propto (1 + R^2 + 2RC\cos 2\pi \underline{h}.\underline{r}) \qquad 2.36$$

where $R = D_h/D_0$

This shows that the standing wavefield intensity is modulated with the lattice periodicity, $d = 1/|h|$, normal to the Bragg planes. The sign of R depends on whether the component plane waves D_0 and D_h of the Bloch wave are in phase or π out of phase. On branch 1 of

the dispersion surface, R is negative and there are antinodes between the planes of atoms. On branch 2, R is positive and the antinodes are in the planes of atoms. Therefore, the branch 1 wavefield is preferentially transmitted and the branch 2 wavefield is preferentially absorbed. These effects are greatest for σ polarisation, which is perpendicular to the dispersion plane.

2.4.9 Rocking-curve width and extinction depth.

The range of Bragg reflection and the extinction distance may be determined geometrically (figure 2.16).

Figure 2.16 Extinction distance and range of Bragg reflection.

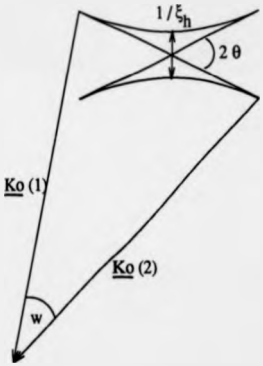

Bragg reflection occurs only across the hyperbolic region of the dispersion surface. The angular range of reflection is proportional to the dispersion surface diameter and inversely proportional to the reciprocal lattice vector.

The plane wave rocking-curve width for a symmetric reflection is

$$w = \frac{2C\sqrt{\chi_h \chi_{\bar{h}}}}{\sin 2\theta} \qquad 2.37$$

where θ is the Bragg angle

and C is the polarisation factor

$C = \frac{1}{2}(1 + |\cos 2\theta|)$ for unpolarised radiation.

The double-crystal rocking-curve width is about 1.4 times w.

For an asymmetric reflection, w is multiplied by $\sqrt{\frac{|\gamma_h|}{\gamma_0}}$, where γ_0 and γ_h are the cosines of the angles of the incident and diffracted beams with the inward surface normal, shown in figure 2.17.

Figure 2.17 Asymmetric Bragg reflection.

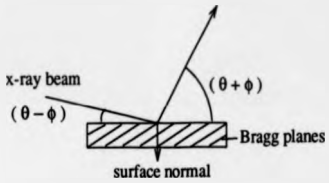

$$\gamma_h = \sin(\theta + \phi)$$
$$\gamma_0 = \sin(\theta - \phi)$$

where θ is the Bragg angle and ϕ is the angle between the Bragg planes and the crystal surface.

The extinction distance, ξ_h is given by the reciprocal of the dispersion surface diameter.

For the symmetric Bragg case,

$$\xi_h = \frac{\lambda \sin\theta}{C\sqrt{\chi_h \chi_{\bar{h}}}} \qquad 2.38$$

For asymmetric reflections, ξ_h is multiplied by $\frac{\sqrt{|\gamma_h|\gamma_0}}{\sin\theta}$, to give the general formula

$$\xi_h = \frac{\lambda \sqrt{\gamma_h |\gamma_0|}}{C \sqrt{\chi_h \chi_{\bar{h}}}} \qquad 2.39$$

The extinction distance, ξ_h is the depth at which the intensity is reduced to $e^{-2\pi}$ of the incident intensity. The contribution to the diffracted intensity decreases exponentially away from the surface. The effect of absorption is to slightly decrease the penetration depth at glancing angles.

At low glancing angles and just below an absorption edge, absorption is the governing effect and the penetration depth at which the intensity is reduced to e^{-1} is

$$d_{e^{-1}} = \frac{\sin(\theta - \phi)}{\mu} \qquad 2.40$$

where μ is the linear absorption coefficient.

At extreme grazing incidence (but not at grazing exit), below the critical angle for total external reflection (0.2° for silicon at 1.5 Å wavelength), the rocking curve becomes very weak and broad (Kishino and Kohra, 1971) and the penetration depth is given by (Vineyard, 1982)

$$d_{e^{-1}} = \frac{\lambda}{4\pi (\psi_c^2 - \psi^2)^{1/2}} \qquad 2.41$$

where ψ_c is the critical angle and ψ is the angle of incidence, $\psi = (\theta - \phi)$.

2.5 Dynamical theory for distorted crystals.

Introduction.

If the crystal is distorted, for example, if it has epitaxial layers with different lattice parameters, the theory must be modified. If the scattering is weak (for thin layers far from the Bragg peak), the kinematical theory may be used. However, for thick or strongly absorbing crystals, this is unsatisfactory. Dynamical theory could be used to calculate the rocking curve from a layered crystal by matching the wave vectors at each interface, though this would be extremely complicated for multiple layers. It is much

simpler to use the differential equations of Takagi (1962, 1969) and Taupin (1964).

2.5.1 Takagi's theory.

Takagi's theory can be applied to both deformed and distorted crystals, and perfect crystals. It takes account of multiple scattering and assumes that x-rays propagate as a plane wave in the crystal, with scattering both into and out of the diffracted beam.

For a layered crystal, it is assumed that there is a single wave vector throughout, so that matching at each interface is unnecessary. The theory can therefore be used for calculating rocking curves from layered crystals, though it does not explain physically what occurs inside the crystal.

2.5.2 The Takagi-Taupin equations.

The Takagi-Taupin equations are two partial differential equations describing the total wave amplitudes, D_0 and D_h, in the forward and diffracted beam directions, s_0 and s_h.

$$\frac{i\lambda}{\pi}\frac{\partial D_0}{\partial s_0} = \chi_0 D_0 + C\,\chi_{\bar{h}} D_h \qquad 2.42a$$

$$\frac{i\lambda}{\pi}\frac{\partial D_h}{\partial s_h} = (\chi_0 - \alpha_h) D_h + C\,\chi_h D_0 \qquad 2.42b$$

A good approximation to the value of α_h (Pinsker, 1978) is

$$\alpha_h = -2\,\Delta\theta \sin 2\theta$$

where $\Delta\theta$ is the deviation from the exact Bragg angle and is negative for deviations on the low-angle side of the Bragg peak.

If the variation of wave amplitudes is considered with respect to depth only, the Takagi-Taupin equations can be used to calculate the reflectivity of a layered crystal. The solution of the Takagi-Taupin equations describes the ratio of amplitudes of the diffracted and incident waves as a function of depth.

The complex amplitude ratio, X is defined as

$$X = \frac{D_h}{D_0} \qquad 2.43$$

Differentiating with respect to depth, z below the surface,

$$\frac{dX}{dz} = \frac{1}{D_0}\frac{\partial D_h}{\partial z} - \frac{D_h}{D_0^2}\frac{\partial D_0}{\partial z} \qquad 2.44$$

Substituting into the Takagi-Taupin equations, with $z = s_0\gamma_0 + s_h\gamma_h$,

$$\frac{dX}{dz} = \frac{i\pi}{\lambda\gamma_0}\left[C\chi_{\bar{h}}X^2 + (\chi_0 - \frac{\gamma_0}{\gamma_h}\chi_0 + \frac{\gamma_0}{\gamma_h}\alpha_h)X - C\frac{\gamma_0}{\gamma_h}\chi_h \right] \qquad 2.45$$

where γ_0 and γ_h are the direction cosines of the incident and diffracted beams relative to the surface normal.

If the crystal is divided into a number of laminae of constant lattice parameter, equation (2.45) can be solved analytically for each lamina. If the amplitude ratio is known at a depth w, $X(w) = k$, then the amplitude ratio above this depth is given by

$$X = \frac{k\sqrt{B^2 - EA} + i(Bk + E)\tan(D\sqrt{B^2 - EA}\ (z - w))}{\sqrt{B^2 - EA} - i(Ak + B)\tan(D\sqrt{B^2 - EA}\ (z - w))} \qquad 2.46$$

where $A = C\chi_{\bar{h}}$, $B = (1 - b)\frac{\chi_0}{2} + \alpha_h\frac{b}{2}$, $D = \frac{\pi}{\lambda\gamma_0}$, $E = -Cb\chi_h$.

and $b = \frac{\gamma_0}{\gamma_h}$ ($b = -1$ for a symmetric reflection).

The amplitude ratio deep inside the crystal is $k = 0$. The reflectivity of the thick substrate crystal is then

$$X = \frac{-B + \sqrt{B^2 - EA}\ \ \mathrm{sign}(\mathrm{Im}(\sqrt{B^2 - EA}))}{A} \qquad 2.47$$

The substrate reflectivity is first calculated using equation (2.47) and the change in reflectivity through the layers is then found. The amplitude ratios are matched at each boundary, starting at the substrate, and the reflectivity at each layer interface is calculated from equation (2.46), in order to obtain the reflectivity at the surface of the crystal. The

intensity, I is then

$$I = \frac{|X|^2}{|b|} \qquad 2.48$$

A rocking-curve simulation program for layered crystals was developed by Halliwell, Lyons and Hill (1984) and Hill (1985), and further developed by Miles (1989). Full derivations of the solution to the Takagi-Taupin equations for layered crystals can be found in Hill's and Miles's theses (Durham University, 1985, 1989).

For the simulations in this thesis, two implementations of the Takagi-Taupin equations were used. The Durham University program was used for the earlier work (courtesy of Prof. B.K.Tanner) and the Bede Scientific Instruments RADS (Rocking Curve Analysis by Dynamical Simulation) program was used for the majority of the simulations.

Chapter 3

3. Diffuse scattering theory.

3.1 Scattering from thin surface layers.

Information on very thin sub-surface layers (down to a thickness of nanometres) may be found in the tails of the Bragg reflection curve.

Afanas'ev et al (1984) give the following approximation to the thickness, t of the layer contributing to the scattering in the tails of the rocking curve at an angular deviation, $\Delta\theta$ from the exact Bragg position.

$$t = \frac{\xi_A w}{\Delta\theta} \qquad 3.1$$

where w is the rocking curve width and ξ_A is the extinction length, calculated from dynamical theory (Chapter 2).

When the exact Bragg condition is satisfied, x-rays are diffracted and the penetration depth of x-rays into the crystal, which is governed by extinction, is much smaller than the penetration depth away from the Bragg angle, which is governed by absorption. However, away from the Bragg peak, the reflected waves from the bulk crystal destructively interfere and most of the scattering comes from the surface and sub-surface layers. The further away from the Bragg peak, the thinner the layer contributing to to the scattered intensity becomes (equation 3.1).

This scattering is called a "surface truncation rod" (Andrews and Cowley, 1985; Robinson, 1986). This is because it forms a rod or streak in reciprocal space close to each Bragg reflection and perpendicular to the crystal surface. It contains information on how the crystal lattice terminates at the surface. Diffuse scattering from imperfections in the bulk crystal is not concentrated along a rod or streak, but is anisotropically distributed around the Bragg reflection, depending on the type of defect (Dederichs, 1971; Trinkhaus, 1972) (section 3.2). Thermal diffuse scattering from vibrations of the lattice

is almost isotropically distributed around each reciprocal lattice point and can therefore be easily distinguished.

Diffuse scattering is caused by imperfections of the crystal lattice, including atomic disorder, point defects (vacancies and interstitials), dislocations and mosaicity. Surface imperfections can be characterised with respect to the depth below the surface, but it is more difficult to determine their distribution in three dimensions (other than by x-ray topography or transmission electron microscopy).

Scattering in a plane in reciprocal space may be measured using a triple-axis diffractometer, where the sample crystal and detector are rotated in a θ-2θ scan (section 3.1.2). Modelling and simulation of the resulting intensity distribution gives quantitative information on the surface and sub-surface regions, for example, disturbed layer thickness and surface or interface roughness (on an atomic scale).

Triple-axis measurements require long data collection times to map even a small area of reciprocal space. Double-axis measurements are much faster, but give only the integrated scatter along a line in reciprocal space. It is therefore more difficult to separate diffuse scattering from the dynamical diffraction peak and the information obtained is less quantitative. However, the angular resolution and signal-to-noise ratio may be greatly improved by the use of a multiple-reflection beam conditioner (section 3.1.1). This makes double-axis diffractometry a feasible technique for the measurement of surface scattering.

3.1.1 Multiple-reflection beam conditioners.

Kirkpatrick and DuMond (1937) first proposed the use of more than two successive reflections to obtain higher resolution. Angular resolution and signal-to-noise ratio may be greatly improved by the use of multiple-reflection beam conditioners (figure 3.1). Bonse and Hart (1965) first used grooved silicon and germanium crystals to obtain tailless multiple-reflection curves. The shape of a multiple-reflection curve is essentially

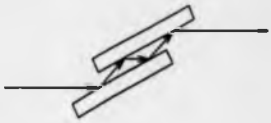

Figure 3.1 Bonse-Hart four-reflection beam conditioner.

a single-reflection curve raised to a power equal to the number of reflections. The resulting curve is not much narrower, but is considerably sharper due to the suppression of the tails and may therefore be used in double- or triple- axis diffractometry to obtain higher resolution. Theoretical double-axis rocking curves calculated for the silicon 004 reflection with $CuK\alpha_1$ radiation using pairs of single-reflection and four-reflection beam conditioners are shown in figure 3.2.

Spectral resolution may be improved by beam conditioners using two grooved crystals rotated in opposite directions in the (+,+) geometry (Beaumont and Hart, 1974; Bartels, 1983).

3.1.2 The triple-axis diffractometer.

Triple-axis diffractometry may be used if very high resolution is required, such as in the measurement of surface scattering, where information would otherwise be lost in the background noise (Cowley and Ryan, 1987). The triple-axis diffractometer has a third axis to enable rotation of the sample crystal and detector in a θ-2θ scan. The direction of the beam reaching the detector is defined by a slit or analyser crystal in front of the detector. This enables separation of diffuse scatter from the dynamical Bragg diffraction peak. An analyser crystal is much preferable to a slit, which causes a reduction in the measured intensity and also measures any x-rays scattered at different angles, due to sample curvature or surface waviness. Alternatively, a position-sensitive detector may

Figure 3.2. Four-reflection beam conditioner. Theoretical rocking curves.

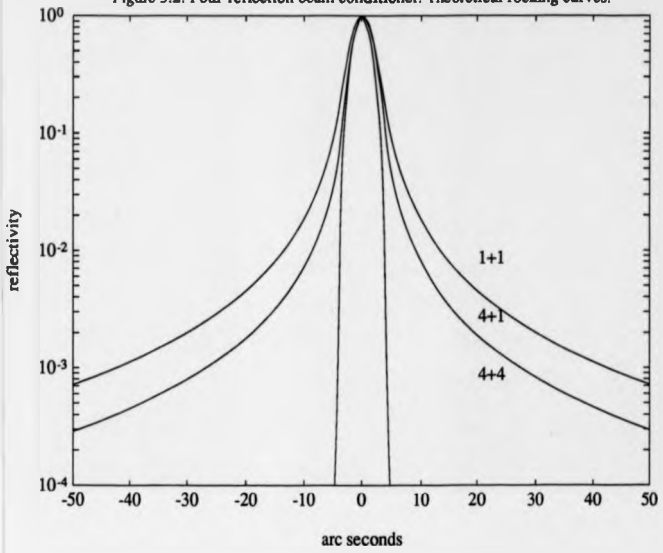

be used without scanning. For triple-crystal diffractometry, the three crystals are positioned in the (+,–,+) geometry as shown in figure 3.3. The monochromator and analyser crystals may be replaced by multiple-reflection beam conditioners in order to increase the resolution (Zaumseil and Winter, 1982). The angle of the diffracted beam from the sample is defined by diffraction from the analyser, which is scanned through 2θ for each position θ of the sample. This extra information enables a map of the intensity distribution in reciprocal space to be obtained. Double-axis diffractometry gives only the integrated intensity along a line in reciprocal space.

If the sample is fixed and the analyser scanned, the intensity along a line in reciprocal space may be measured. Diffuse scattering can be separated from the dynamical diffraction peak by setting the sample slightly off the Bragg angle and

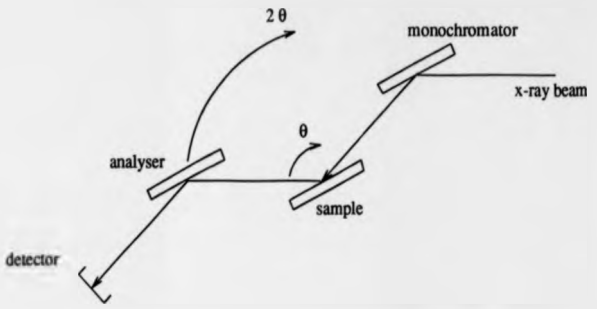

Figure 3.3 Triple-axis diffractometer.

scanning the analyser (Iida and Kohra, 1979; Zaumseil and Winter, 1982). This is much faster than using a θ-2θ scan. The analyser removes the effects of sample curvature and surface waviness which would otherwise broaden the rocking curve and smear out any surface layer interference fringes.

3.2 Diffuse scattering from defects.

Introduction.

Several types of defects exist in crystal lattices. These include intrinsic defects (point defects- vacancies and interstitials; extended defects- dislocations, stacking faults) and extrinsic defects (impurity atoms- substitutional or interstitial; precipitates). Defects may be characterised by x-ray topography only if their strain fields are larger than the resolution of the topograph, about 1 μm (Köhler and Möhling, 1983). If the defect density is high, the strain fields overlap and cannot be resolved separately on an x-ray topograph. They can then only be distinguished if there is an inhomogeneous distribution of defects, such as that found in swirl and growth striations. However, it is possible to measure an averaged value of the diffracted intensity from a crystal with randomly distributed defects and to obtain from this, information quantitatively characterising the

defects, such as their mean size, concentration and the strength and symmetry of their displacement fields. The intensity of diffuse x-ray scattering from defects may be measured using triple-axis diffractometry (Iida and Kohra, 1979; Iida, 1979; Lomov, Zaumseil and Winter, 1985) or by double-axis diffractometry (Thomas, Baldwin and Dederichs, 1971; Patel, 1975).

The theory of elastic x-ray scattering at static displacements of lattice atoms was first discussed by Huang (1947), who found that the Bragg peak intensity weakened and that diffusely scattered intensity appeared close to the Bragg peak. This is similar to the effects of diffuse scattering due to thermal vibrations of the crystal lattice. However, scattering from dynamic thermal displacements of lattice atoms is inelastic, as is scattering by electrons (Compton scattering), which is negligible close to a Bragg peak. This incoherent intensity can be readily subtracted from the dynamical diffraction peak.

Diffuse scattering is observed away from the Bragg peak, where the kinematical theory may be applied, even in nearly perfect crystals (Krivoglaz, 1969). However, it has been shown (Thomas, Baldwin and Dederichs, 1971) that in the range of total reflection for nearly perfect crystals, diffuse scattering is affected by dynamical theory. Outside this range, the difference between the results of the kinematical and dynamical theories is negligible (Holý, 1984). Scattering from randomly distributed defects and from the static displacements they introduce may be treated using the kinematical approximation in the theory of diffuse scattering (Krivoglaz, 1969; Dederichs, 1971, 1973; Trinkhaus, 1972; Peisl, 1976) or, if the crystal is nearly perfect, using dynamical theory by separating the coherent and incoherent intensities (Kato, 1980; Holý, 1984; Holý and Gabrielyan, 1987). The coherent and incoherent intensities are often referred to as dynamical and kinematical components of the diffracted intensity. This is justifiable, since the incoherent scattering away from the Bragg peak may be treated kinematically to a very good approximation.

The diffuse scattering intensity depends on the concentration of defects and on the

strength and symmetry of the displacement fields they create. Diffuse scattering will be treated first using the results of kinematical theory.

3.2.1 Kinematical theory of diffuse scattering.

Following the treatment of Peisl (1976), the scattering vector, $\underline{k}$ for elastic scattering of x-rays from atoms, is defined as

$$\underline{k} = \underline{K}_A - \underline{K}_0 \qquad 3.2$$

where $|\underline{K}_0| = |\underline{K}_A| = \frac{2\pi}{\lambda}$.

Figure 3.4 Scattering vector k in reciprocal space.

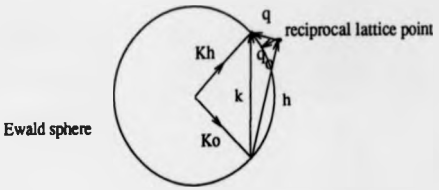

From the kinematical theory, the total scattered intensity (in electron units) is the square of the sum of the scattering amplitudes, f over the n atoms in the crystal, with appropriate phase shifts for atoms n at positions $\underline{r}_n$.

$$I = |\sum_n f_n \exp(i\, \underline{k}.\underline{r}_n)|^2 \qquad 3.3$$

The scattering factor, f includes a static Debye-Waller factor, e^{-L}, which accounts for the weakening of the peak intensity due to static displacements of the lattice atoms.

In an ideal crystal lattice, the atoms scatter in phase when $\underline{k} = \underline{h}$, the reciprocal lattice vector. This is Bragg scattering. If there are defects introduced into the crystal, the lattice atoms are shifted to new positions, $\underline{r}_n + \underline{u}_n$.

The scattered intensity is then

Figure 3.5 Displacement of lattice atoms by defect.

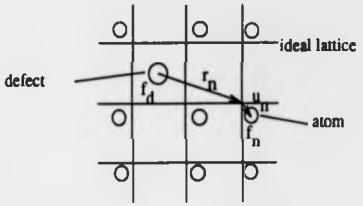

$$I = |\sum_n f_n \exp(i\,\underline{k}.(\underline{r}_n + \underline{u}_n)) + \sum_d f_d|^2 \qquad 3.4$$

where d is the number of defects and f_d is the scattering amplitude for a defect atom.

Defects generally have two effects on the Bragg peak.

1.) The Bragg peak is shifted owing to the change in lattice parameter of the "average" lattice, $\frac{\Delta d}{d} = -\Delta\theta \cot\theta$.

2.) The peak intensity decreases and diffuse scattering intensity appears close to the Bragg peak owing to deviations from the average lattice.

The diffuse scattering intensity is obtained by subtraction of the Bragg scattering intensity from the total intensity due to randomly distributed defects in an average lattice.

$$I = N|f_d + \sum_n f_n \exp(i\,\underline{k}.(\underline{r}_n + \underline{u}_n)) - \sum_n f_n \exp(i\,\underline{k}.\underline{r}_n)|^2 \qquad 3.5$$

where N is the number of defects (for small defect concentrations).

For small defects (point defects), equation (3.5) may be approximated to

$$I = N|f_d + i f\,(\underline{k}.\vec{\underline{U}})|^2 \qquad 3.6$$

where $\vec{\underline{U}}$ is the Fourier transform of the displacement field $\underline{u}(r)$,

$$\vec{\underline{U}} = \int_V \underline{u}(r) \exp(i\,\underline{k}.\underline{r})\, dV \qquad 3.7$$

which may be written as the sum of displacements over the n displaced atoms,

$$\underline{U} = \sum_n \underline{u}_n \exp(i\, \underline{k}.\underline{r}_n). \qquad 3.8$$

The square of the first term in equation 3.6, $I = N|f_d|^2$ is the scattering from the the defect, which appears far from the Bragg peak. The scattering amplitude is $f_d = f$ for a self-interstitial and $f_d = -f$ for a vacancy.

The square of the second term, $I = N f^2 |\underline{k}.\underline{U}|^2$ is the scattering from the distortion field of the defect (called Huang scattering), which appears close to the Bragg peak. This is coherent scattering from the displacement field at long distances from the defect, where the displacements are small. Information on the strength and symmetry of the displacement field and hence the defect, may be obtained from the diffuse scattering intensity distribution. The diffuse scattering is even closer to the Bragg peak for larger defects (or clusters of defects). The scattering intensity is is proportional to $1/q^2$, where q is the distance from the reciprocal lattice point and $\underline{q} = \underline{k} - \underline{h}$ (figure 3.4). Huang scattering is analogous to thermal diffuse scattering, which also appears close to the Bragg peak.

For large displacements (defect clusters with strong displacement fields), the diffuse scattering intensity distribution has an asymmetric component, proportional to $1/q$ (Dederichs, 1971). For defects in the bulk crystal, interstitial clusters give more intensity at higher Bragg angles and vacancy clusters give more intensity at lower Bragg angles. (See section 3.2.3 for surface defects).

The mixed squared term from equation 3.6 describes the interference between the scattering from the defect and from its displaced neighbouring atoms. This may also give rise to a shift of the diffuse scattering intensity with respect to the Bragg peak. Between Bragg reflections, both scattering intensities are of the same order of magnitude and information on the position of the defect atom and displacements of atoms close to the defect may be obtained (Haubold, 1975).

If the lattice distortion is very large, such as that near a cluster of defects or a

dislocation loop, equation 3.6 is no longer valid. The scattering is incoherent and the intensities from small volume elements around the defect are added. This is called asymptotic scattering, since it comes from displacements close to the defect and therefore appears at some distance from the Bragg peak. Information on the defect size, strength and orientation may be obtained from this scattering intensity, which is proportional to $1/q^4$. Dederichs (1971) gives intensity formulae for scattering from defect clusters and dislocation loops. Asymptotic scattering is useful in the case where there are different types of defect which expand and contract the lattice by the same amount. The overall change in lattice parameter is zero, but the asymptotic scattering still gives information on displacements close to the defects.

If the defects are infinitely extended (dislocation lines), the crystal becomes mosaic and there is broadening of the Bragg peak (Krivoglaz, 1969). This broadening is proportional to the square root of the dislocation density. The theory has been developed by Krivoglaz and Ryaboshapka (1962) and Wilkens (1970), but will not be discussed here.

3.2.2 Determination of defect properties.

The diffuse scattering intensity distribution close to the Bragg peak (Huang scattering) depends on the Fourier transform of the displacement field.

$$I_{Huang} = N f^2 |\underline{k}.\underline{U}|^2 \qquad 3.9$$

Information on the displacement field enables determination of the defect type and orientation.

The displacement field $\underline{u}(r)$ at a long distance away from a point defect is,

as $r \rightarrow \infty$

$$\underline{u}(r) \propto \frac{1}{r^2}$$

This corresponds to a Fourier transform $\underline{\tilde{U}}(q)$ close to the reciprocal lattice point, as $q \rightarrow 0$

$$\underline{\tilde{U}}(q) \propto \frac{1}{q}$$

Therefore, from equation 3.9, the Huang scattering intensity is proportional to k^2 / q^2.

If the defects all have the same orientation in the crystal, the elastic dipole tensor of the displacement field may be directly determined from the diffuse scattering intensity near one Bragg reflection. For example, totally uniform defects in a cubic lattice, in the simplest case, give a scattering intensity from (h00) Bragg planes in the [q00] direction of

$$I = N \frac{|F|^2}{V^2} \left[\frac{P_{11}}{C_{11}} \right]^2 \left[\frac{k}{q} \right]^2 \qquad 3.10$$

where F is the structure factor, V is the volume of the unit cell, P_{11} is the component of the elastic dipole tensor and C_{11} is the elastic constant of the crystal for the (100) orientation in the [100] direction (see appendix). The absolute concentration of defects, N can be determined, since the Huang scattering intensity and the change in lattice parameter are differently related to the dipole tensor, P.

$$I_{Huang} \propto N P^2 \qquad \frac{\Delta a}{a} \propto N P$$

If the defects have random orientations, three different Bragg reflections are required to totally characterise the defect structure (Trinkhaus, 1972; Peisl, 1976).

From equation 3.9, the Huang scattering intensity depends on $\underline{k}.\underline{\tilde{U}}$, so there should be zero intensity when $\underline{k}$ is perpendicular to $\underline{\tilde{U}}$ and maximum intensity when $\underline{k}$ is parallel to $\underline{\tilde{U}}$. For an isotropic defect in an isotropic crystal, equal intensity contours will be in the form of spheres touching the reciprocal lattice point, with zero intensity in a plane perpendicular to to the reciprocal lattice vector. This is shown in figure 3.6.

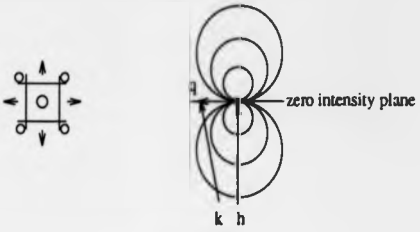

Figure 3.6 Isotropic distortion. Equal intensity contours in reciprocal space.

If the defect and its displacement field are anisotropic, averaging over different defect orientations results in the superposition of several differently orientated intensity distributions in reciprocal space. The zero intensity planes may intersect along one axis to produce scattering intensity distributions with zero intensity lines or, more generally, along several axes to produce scattering intensity in all directions. For example, a tetragonal distortion in an isotropic cubic crystal gives different diffuse scattering intensities around different reciprocal lattice points, as shown in figure 3.7 (after Peisl, 1976). Elastically anisotropic crystals (such as silicon) produce distorted scattering intensity distributions.

Diffuse scattering intensity in reciprocal space can be measured using triple-axis diffractometry. The type of defect may be deduced from the symmetry of the scattering intensity distribution by comparison with theory. Lomov, Zaumseil and Winter (1985) measured diffuse scattering from [111] oriented stacking faults in annealed silicon wafers.

If the diffuse scattering is measured using double-axis diffractometry, the intensity is integrated along a line in reciprocal space. The deviation from the Bragg peak is given by $\Delta\theta = q_0 / h\cos\theta$, where q_0 is the minimum value of q, from figure 3.4, and the intensity is integrated over all q on the Ewald sphere. The information obtained from the

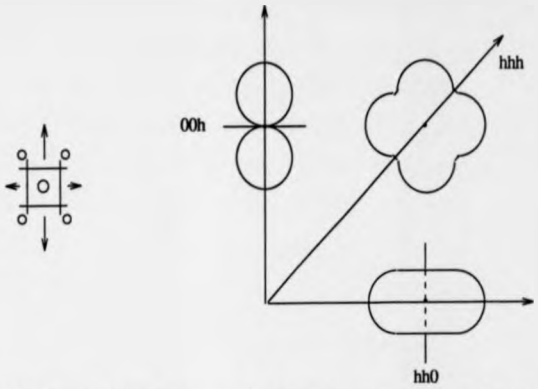

Figure 3.7 Tetragonal distortion. Equal intensity contours in reciprocal space.

rocking curve is less quantitative, but the symmetry of the scattering intensity can still be determined. The dependence of the scattering tails on $1/q^2$ or $1/q^4$ can also be determined, giving information on the defect size and strength. Patel (1975) measured diffuse scattering from oxygen clusters in heat-treated silicon and Lal and Bhagavannarayana (1989) compared scattering from defects in Czochralski and float-zone silicon.

3.2.3 Surface diffuse scattering.

If defects are present only at the surface of the crystal, the diffuse scattering intensity is distributed along a rod or streak in reciprocal space, perpendicular to the surface, as discussed in section 3.1. This has been investigated only in the last few years (Andrews and Cowley, 1985; Robinson, 1986). The diffuse scattering may be shifted with respect to the Bragg peak due to lattice expansion or contraction by the defects. This depends on the size and concentration of the defects, and whether they are in the bulk crystal or only near the surface.

In the bulk crystal, the lattice is constrained in all directions by the surrounding

crystal. Defects which expand the unit cell (interstitials and larger substitutional impurity atoms) will compress the surrounding lattice and the diffuse scattering near the Bragg peak will have higher intensity on the high-angle side of the peak. Conversely, defects which contract the unit cell (vacancies and smaller substitutional atoms) will expand the surrounding lattice and the intensity will be higher on the low-angle side of the Bragg peak.

Figure 3.8 Defects in bulk crystal: Lattice compression.

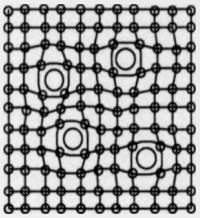

Surface defects will have a different effect, since the crystal is unconstrained in the direction normal to the surface and is therefore able to expand or contract freely in this direction, producing a tetragonal distortion (involving Poisson's ratio). Defects which expand the unit cell will therefore give higher intensity on the low-angle side of the Bragg peak and vice versa. This is opposite to the shift of the diffuse scattering intensity caused by defects in the bulk crystal.

Figure 3.9 Surface defects: Lattice expansion.

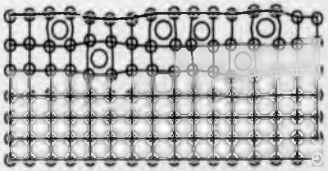

Diffuse scattering from the surface of mechanochemically polished silicon has been measured by Kashiwagura, Harada and Ogino (1983) and Harada et al (1987). They found rod-shaped scattering near the reciprocal lattice point, which was shifted to the low-angle side. This disappeared on etching. Kashihara, Kawamura, Kashiwagura and Harada (1987) describe the rod-shaped scattering in terms of a lattice expansion and atomic density modulation at the crystal surface. Rocking-curve analysis of polished silicon wafers using a four-reflection beam conditioner (Hart, Bowen and Fisher, 1989) also gave a lattice expansion and defects or atomic disorder at the surface.

Iida and Kohra (1979) used triple-axis diffractometry with a five-reflection monochromator, by scanning the analyser at various sample positions, to measure diffuse scattering from surfaces of silicon crystals which had been mechanically damaged (lapped and scratched). They were able to separate the effects of lattice dilation, tilt and surface unevenness. The lapped crystal was successively etched and found to have heavily distorted, mosaic and strained layers. The etching treatment resulted in a highly uneven surface which broadened the rocking curve. The scratched crystals gave strong diffuse scattering and a weakening of the dynamical peak.

Zaumseil and Winter (1982) used one- and five-reflection monochromators and analysers to measure diffuse scattering from finely ground and mechano-chemically polished silicon wafers. The ground wafer gave strong diffuse scattering which disappeared on etching. The diffuse scattering from the polished wafers remained after etching and was therefore deduced to be thermal diffuse scattering.

3.2.4 Dynamical theory for randomly disturbed crystals.

If the defects are small (not resolvable by topography) and the crystal is nearly perfect, it is necessary to use dynamical theory to calculate intensities close to or in the range of the Bragg reflection. Kato (1980) first introduced a general statistical theory of dynamical x-ray diffraction in randomly disturbed crystals, which involved separate consideration of coherent and incoherent parts of the total diffracted intensity. Holy

(1983, 1984) derived formulae for the diffracted intensity from crystals with randomly distributed defects, based on the solution of the Takagi equations. Following the treatment of Holý and Gabrielyan (1987), the coherent and incoherent (or partially coherent) intensities will be considered.

Coherent intensity.

Assuming an incident plane wave, an averaged value for the amplitude of the wavefield in a crystal with randomly distributed defects is derived from the differential equations of Takagi (1969). A dispersion relation is formulated and the wave vectors of the coherent plane waves propagating in the crystal are determined from the boundary conditions at the crystal surface. The amplitude ratio and the coherent intensity can then be calculated. This is analogous to the dynamical theory for a perfect crystal described in Chapter 2.

To an approximation, if diffuse scattering is neglected, the coherent amplitude is equivalent to the amplitude from a perfect crystal multiplied by a static Debye-Waller factor, e^{-L}, (called a "quasiperfect" crystal), where

$$e^{-L} = \exp\left[-2\pi i\, \underline{h}.\underline{u}(r)\right] \qquad 3.11$$

The intensity is multiplied by e^{-2L}.

For a random defect distribution, e^{-L} is statistically averaged over all defect configurations. For displacements u_h, perpendicular to the reflecting planes, e^{-L} reduces to

$$e^{-L} = \exp\left[-8\pi^2 (1/2d)^2 \overline{u_h^2}\right] \qquad 3.12$$

since $\overline{e^{iu}} \simeq e^{-\frac{1}{2}\overline{u^2}}$ and $|h| = 1/d$.

When diffuse scattering is not neglected, the dynamical theory predicts a decrease in the coherent intensity due to diffuse scattering of x-rays in other directions. This is called diffuse absorption and it takes effect only in the range of total reflection.

Incoherent intensity.

The degree of coherence of the diffracted wave in a crystal with randomly distributed defects is described by an averaged coherence function (Holý, 1983) which depends on the correlation function of deformation fields of the defects. Diffusely scattered divergent waves arise in the disturbed crystal by diffraction of the incident plane wave. The diffracted intensities and their angular distributions can be determined from iterative solutions of the Takagi equations. Figure 3.10 shows the first and second iterations of the incoherent intensity, the coherent intensity for a quasiperfect crystal and the total intensity for silicon with a random distribution of spherical precipitates of radius 24 nm and total volume 1% (after Holý, 1984). The incoherent (or partially coherent) intensity distribution is asymmetric in the range of total reflection, due to anomalous dispersion.

Figure 3.10 Incoherent and coherent intensities ($CuK\alpha_1$, Si symmetric 422 reflection).
-- first iteration _ coherent intensity
.. second iteration _. total intensity

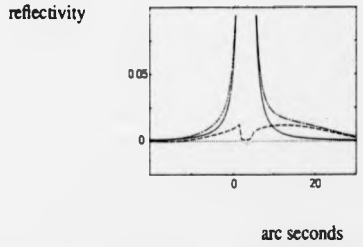

Figure 3.11 is a comparison of the first iteration of the incoherent intensity with diffuse scattering computed from kinematical theory (Dederichs, 1971), for the same size and concentration of defects as above (after Holý, 1984). This shows that multiple diffuse scattering may be neglected in the tails of the reflection curve and the kinematical approximation in the diffuse scattering theory may therefore be used.

Figure 3.11 Comparison of dynamical and kinematical theories ($CuK\alpha_1$, Si 422).
_ dynamical theory -- kinematical theory
.. coherent intensity

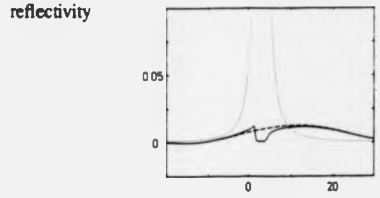

Defects can be characterised by their concentration, radius and the strength of the displacement field. The static Debye-Waller factor and correlation function of the displacement field depend on the volume taken up by the defects in the crystal. The diffuse scattering intensity increases linearly with the concentration of defects. Figure 3.12 shows the effect of varying the defect radius, for a constant total volume of 1% (after Holý, 1983).

The diffuse scattering intensity increases and moves closer to the Bragg peak as the defect size increases. These results agree with those predicted by kinematical theory (section 3.2.1). It is therefore possible to characterise small, randomly distributed defects in nearly perfect crystals by comparison of experimental and theoretical reflection curves.

Holý and Kuběna (1987, 1989) used double- and triple- axis diffractometry with a three-reflection monochromator to measure Laue case reflection and transmission curves of annealed silicon with growth striations due to oxygen precipitates. The defects were modelled by amorphous spheres. The experimental rocking curves agreed quite well with theory, though the theory for randomly distributed defects does not account for inhomogeneously distributed defects or anisotropic defects with equivalent orientations. The theory would also have to be modified for crystals having only surface defects.

Figure 3.12 Effect of varying the defect radius ($CuK\alpha_1$, Si symmetric 333 reflection).
a) 0.2μm, b) 0.4μm, c) 0.6μm, d) 0.8μm, e) 1.0μm
-- coherent intensity

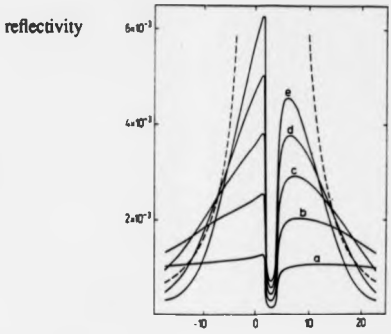

Conclusion.

Diffuse scattering gives useful information on the concentration, size, type and orientation of defects in crystals, which is particularly useful when the defects are too small to be resolvable by topography. The kinematical or dynamical theories of diffuse scattering could eventually be incorporated into simulation programs for diffraction from crystals with strained surface layers.

Chapter 4

4. X-ray reflectivity theory.

4.1 Introduction.

The refractive index of x-rays in matter is less than one and there is total external reflection at angles of incidence less than the critical angle. The penetration depth is then greatly reduced and only the surface is probed, down to depths of a few nanometres to several hunded nanometres. The difference of the refractive index from unity depends on the electron density of the material. Analysis of the curve of reflected x-ray intensity versus either angle or energy gives information on the variation of electron density with depth near the surface. This enables determination of surface layer thickness, density and surface and interface roughness. Reflectivity measurements give information on both amorphous and crystalline layers.

In this chapter, reflectivity theory is summarised, with emphasis on energy dispersive reflectivity. This is a new technique which enables measurement of a range of energies simultaneously reflected from a sample at a fixed angle of incidence. The data collection time is therefore much shorter than in most angle dispersive techniques, where the sample is rotated step by step through a range of angles.

The refractive index, n is less than unity by

$$n = 1 - \delta - i\beta \qquad 4.1$$

where

$$\delta + i\beta = \frac{\lambda^2}{2\pi} r_e \, (Z + f' + if'') N \qquad 4.2$$

where N is the number of atoms per unit volume, $N = N_A \, \rho / A$

N_A is Avogadro's number

ρ is the density

A is the atomic weight

Z is the atomic number

f' is the dispersion correction to the atomic scattering factor

f'' is the absorption correction to the atomic scattering factor

and

$$\beta = \frac{\lambda\mu}{4\pi} \qquad 4.3$$

where μ is the linear absorption coefficient.

The critical angle for total external reflection, ψ_c is given by

$$\psi_c = \cos^{-1} n \approx \sqrt{2\delta} \qquad 4.4$$

The critical angle depends only on the density of the medium and the wavelength or energy of radiation, according to the formula $\psi_c = 1.64\times10^{-3}\sqrt{\rho}\,\lambda$, where ρ is in g/cm^3 and λ is in Å

For energy dispersive reflectivity, where the angle of incidence, ψ is fixed, the critical energy, E_c is given by $E_c \approx 2.05\times10^{-2}\sqrt{\rho}/\psi$, where ρ is in g/cm^3 and E_c is in keV. In this case, the deviation of the refractive index from unity ($\delta + i\beta$) changes with wavelength (equation 4.2). The dispersion corrections, f' and f'' and linear absorption coefficient also change.

4.2 Reflectivity theory for layered structures.

The theory of x-ray reflectivity from a multi-layered structure was developed by Parratt (1954). A summary is given here.

For two homogeneous media, where medium 1 is air and medium 2 is the crystal, the ratio of the electric vector of the reflected beam, E_1^R and the electric vector of the incident beam, E_1 is given by the Fresnel coefficient

$$F_{1,2} = \frac{E_1^R}{E_1} = \frac{f_1 - f_2}{f_1 + f_2} \qquad 4.5$$

where

$$f_1 = \psi$$
$$f_2 = (\psi^2 - \psi_{c2}^2)^{1/2} \qquad 4.6$$

ψ is the angle of incidence and ψ_c is the critical angle.

If absorption is taken into account, f_n becomes complex.

$$f_n = (\psi^2 - 2\delta_n - 2i\beta_n)^{1/2} \qquad 4.7$$

or

$$f_n = A_n - iB_n$$

where

$$A_n = 1/\sqrt{2}\,[\,((\psi^2 - \psi_{c(n)}^2)^2 + 4\beta_n^2)^{1/2} + (\psi^2 - \psi_{c(n)}^2)\,]^{1/2}$$

and

$$B_n = 1/\sqrt{2}\,[\,((\psi^2 - \psi_{c(n)}^2)^2 + 4\beta_n^2)^{1/2} - (\psi^2 - \psi_{c(n)}^2)\,]^{1/2}$$

For N homogeneous media, where medium 1 is air and medium N is the substrate, the reflectivity is given by the recursion formula for the reflectivity from the $n-1,n$ interface

$$R_{n-1,n} = a_{n-1}^4 \left(\frac{R_{n,n+1} + F_{n-1,n}}{R_{n,n+1} F_{n-1,n} + 1} \right) \qquad 4.8$$

where

$$R_{n,n+1} = a_n^2 \left(\frac{E_n^R}{E_n} \right)$$

$$F_{n-1,n} = \frac{f_{n-1} - f_n}{f_{n-1} + f_n}$$

and a_n is the amplitude factor for half the thickness d_n of layer n.

$$a_n = \exp(-i\,\pi/\lambda\, f_n d_n) \qquad 4.9$$

Interface roughness can be modelled by multiplying each Fresnel coefficient, $F_{n-1,n}$

by a Gaussian function (Cowley and Ryan, 1987), given by

$$\exp -\tfrac{1}{2}[(4\pi\sigma_n/\lambda)\sin\psi]^2 \qquad 4.10$$

where σ_n is the root-mean-square roughness for layer n.

The recursion formula (4.8) is solved by starting at medium N, where $R_{n,n+1}$ is zero (since the substrate thickness is taken to be infinite), and ending at medium 1, where a_1 is unity, giving the reflectivity $R_{1,2} = E_1^R/E_1$.

The ratio of the reflected to incident intensities is given by the product of $R_{1,2}$ with its complex conjugate

$$\frac{I_R}{I_0} = \frac{|E_1^R|^2}{|E_1|^2} = |R_{1,2}|^2 \qquad 4.11$$

For angle dispersive reflectivity, at a fixed wavelength, the dispersion corrections f' and f'' in equation 4.2 can be found in the International Tables for X-ray Crystallography, Volume IV (1974).

However, for energy dispersive reflectivity at a fixed angle, the dispersion corrections vary with the wavelength and can be calculated to a good approximation using Hönl's formulae (James, 1948).

A computer program to calculate reflectivities from a range of materials for both angle dispersive and energy dispersive modes was developed by S. Miles at Durham University (1989). This has been used to calculate the theoretical reflectivity curves in this chapter and in Chapter 8.

4.2 Effect of layer density, thickness and roughness.

Angle dispersive reflectivity curves for silicon are shown in figure 4.1, for CuKα_1(1.54 Å), MoKα_1(0.71 Å) and WKα_1(0.21 Å) radiation. The critical angle increases with wavelength. This is also shown in figure 4.8 of penetration depths at the critical angle. The reflectivity decreases more rapidly for shorter wavelengths. The

Figure. 4.1. Angle dispersive reflectivity of silicon for various wavelengths.

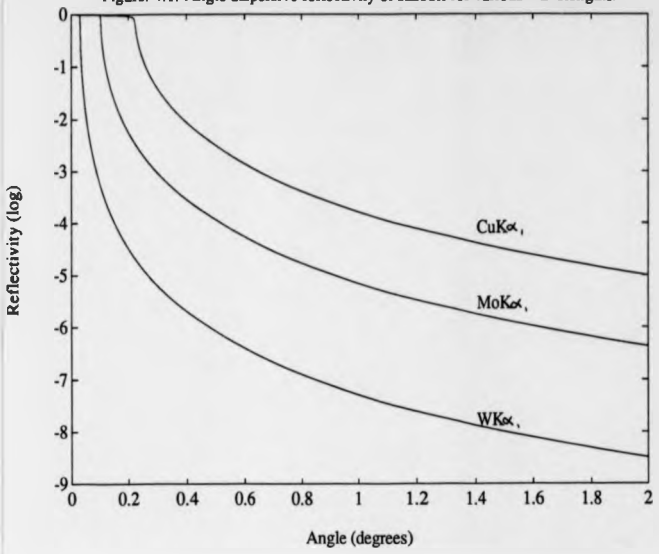

Figure. 4.2. Energy dispersive reflectivity of silicon for a range of angles.

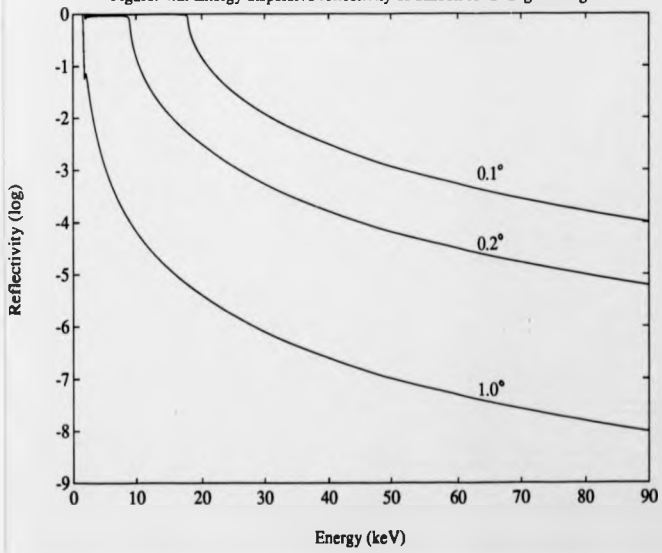

longer wavelengths are therefore more useful for measuring a large angular range. Figure 4.2 shows energy dispersive reflectivity curves for silicon at 0.1°, 0.2° and 1.0°. The critical angle and reflectivity increase with decreasing angle of incidence. Low angles of incidence therefore give higher intensities. The Si K absorption edge can be seen at 1.84 keV.

Surface layers give interference fringes, with amplitude depending on the layer density and period on the layer thickness. Surface or interface roughness decreases the reflectivity and smears out any interference fringes. Surface layers give similar effects for angular and energy dispersive modes. The reflectivity curves shown in figures 4.2 to 4.7 are energy dispersive (at 0.1° incidence) since this applies to the experiments described in Chapter 8. Figure 4.3 shows the effect of 10 Å root-mean-square surface roughness. The gradient of the reflectivity curve decreases more rapidly. Figures 4.4 and 4.5 show the effect of 20 Å interface roughness on 200 Å layers of silicon dioxide on silicon and aluminium oxide (Al_2O_3) on aluminium. The interference fringes become smeared out further away from the critical energy. The effect of layer density on fringe amplitude can also be seen. Silicon dioxide has a density 5% less than that of silicon and results in shallow fringes with intensity lower than for silicon. The density of aluminium oxide is almost 50% greater than that of aluminium and the fringes have a large amplitude and higher intensity than the aluminium reflectivity curve. The Al K absorption edge can be seen at 1.6 keV. The effect of varying the layer thickness is shown figures 4.6 and 4.7 for SiO_2 and Al_2O_3 layers ranging from 25 Å to 200 Å thick. Fringe period is inversely proportional to layer thickness.

For angle dispersive reflectivity, the fringe period is given by

$$\Delta\psi = \frac{\lambda}{2t\cos\psi} = \frac{\lambda}{2t} \qquad 4.12$$

where t is the layer thickness.

Figure. 4.3. Energy dispersive reflectivity of silicon with surface roughness. 0.1° incidence.

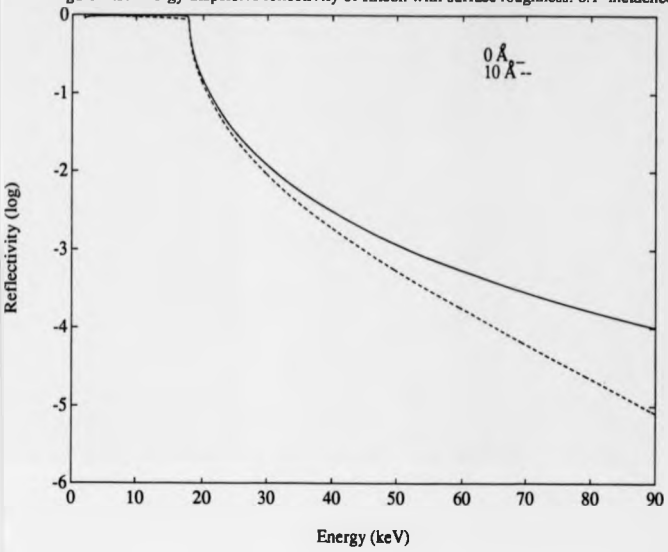

Figure. 4.4. Energy dispersive reflectivity of 200 Å SiO_2/Si. 0.1° incidence.

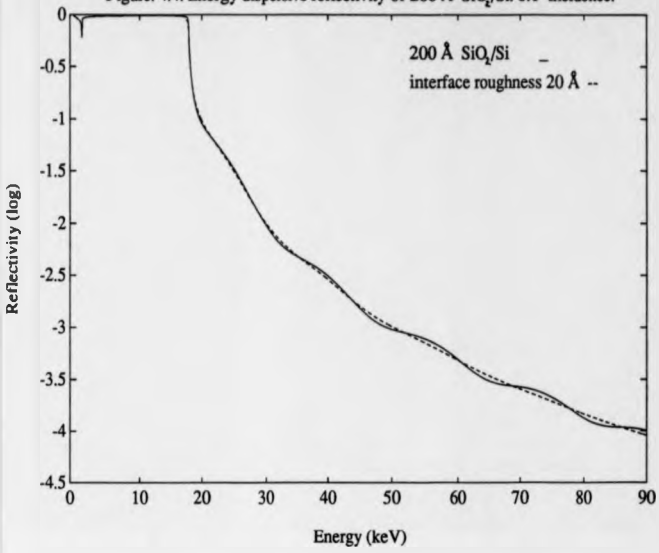

Figure. 4.5. Energy dispersive reflectivity of 200 Å Al_2O_3/Al. 0.1° incidence.

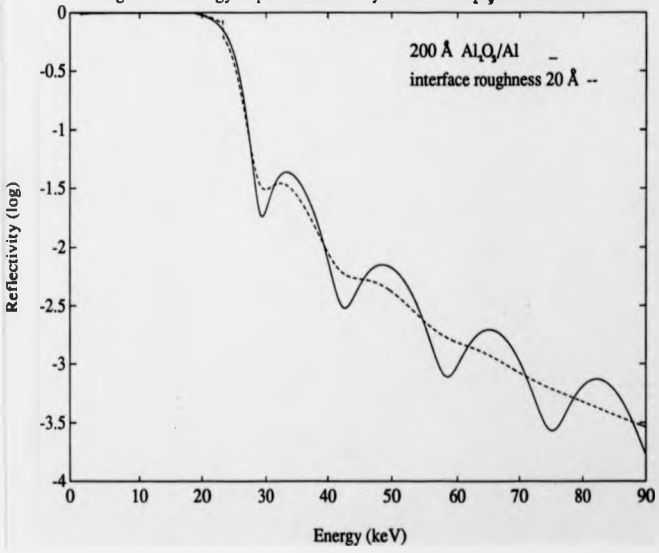

Figure 4.6. Effect of varying layer thickness for SiO_2 on Si.

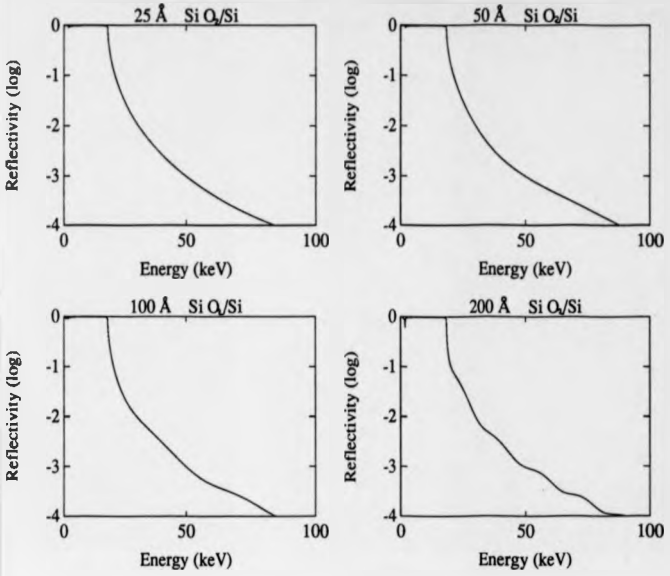

Figure 4.7. Effect of varying layer thickness for Al_2O_3 on Al.

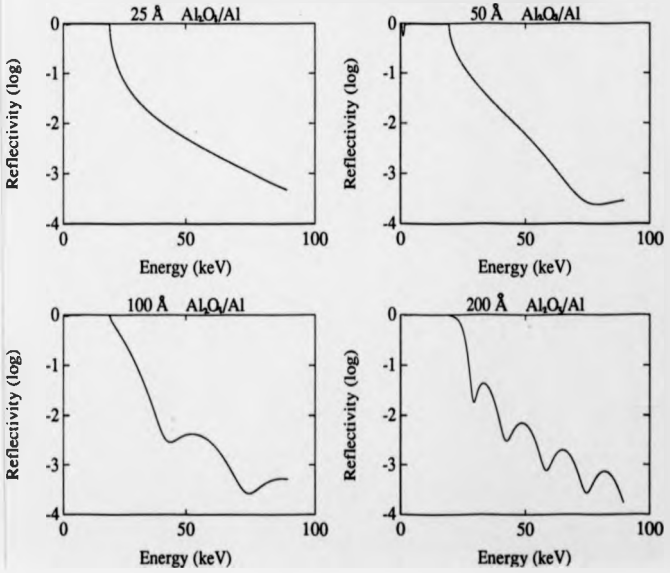

For energy dispersive reflectivity, the fringe period is

$$\Delta E = \frac{hc}{2t\sin\psi} \approx \frac{hc}{2t\psi} \qquad 4.13$$

Most of the information on thin surface layers is found away from the critical angle or energy. This is analogous to the surface scattering away from the Bragg diffraction peak discussed in Chapter 3.

For specular reflection, the penetration depth at which the intensity is reduced to $1/e$ is given by (Parratt, 1954)

$$d_{e^{-1}} = \lambda\sqrt{2}/4\pi[\,((\psi^2 - \psi_{c(a)}^2)^2 + 4\beta_a^2)^{1/2} - (\psi^2 - \psi_{c(a)}^2)\,]^{1/2} \qquad 4.14$$

Figure 4.8 shows plots of the variation of penetration depth with angle for several different wavelengths, $CuK\alpha_1$(1.54 Å), $MoK\alpha_1$(0.71 Å) and $WK\alpha_1$(0.21 Å).

Figure 4.8. Penetration depth near the critical angle for various wavelengths.

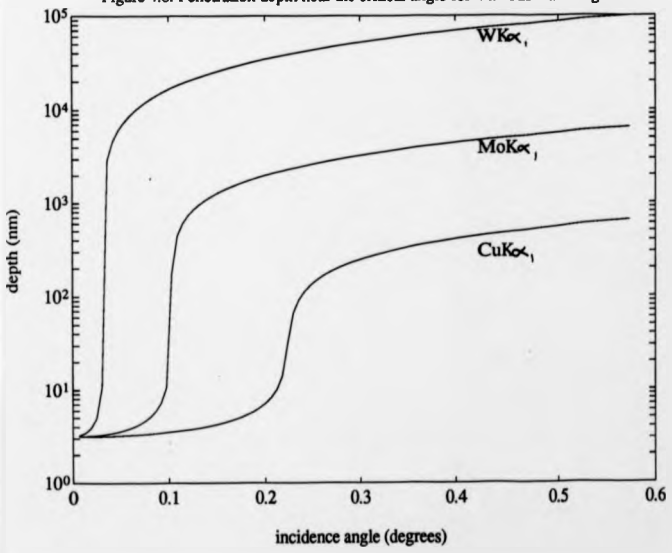

Chapter 5

5. Experimental Techniques.

This chapter covers the practicalities of taking a rocking curve or a topograph, the design of multiple-reflection beam conditioners and the experimental instrument function for the double-axis diffractometer used at Warwick University.

5.1 Practical aspects of double-axis diffractometry.

5.1.1 Instrumentation.

Double-axis diffractometry experiments were performed at Warwick University on a Bede Scientific Instruments model 450 diffractometer (with 450 mm between the axes) shown in photograph 5.1. The first crystal axis was coaxial with the diffractometer rotation axis. The detector was mounted on an axis coaxial with the second crystal axis. The diffractometer was mounted to give a vertical dispersion plane. In this position, the axes are horizontal and samples can be mounted kinematically, eliminating unnecessary strains. The smallest obtainable step size of the diffractometer fine axes was 0.05 arc seconds, with a total range of about 10°. The diffractometer was controlled by an Amstrad PC 1640 using Bede software with a Bede Minicam interface. A Nuclear Enterprises DM1.1 scintillation counter was used. The x-ray generator was a Hiltonbrooks model DG2 with AEG fine-focus sealed x-ray tubes rated up to 3 kW, with Cu or Mo targets. The x-ray tube and diffractometer were mounted inside a steel enclosure with a lead perspex window and a safety-interlocked door.

Grazing incidence white radiation and double-crystal topography, requiring high intensity x-rays, were carried out at Daresbury Synchrotron Radiation Source (SRS). Comprehensive reviews of x-ray and synchrotron radiation sources are given by Bonse (1980) and Bowen (1988). Experiments were performed using the high-precision double-crystal diffractometer shown in photograph 5.2, described by Bowen and Davies

Photo 5.1. The Bede model 450 diffractometer at Warwick University.

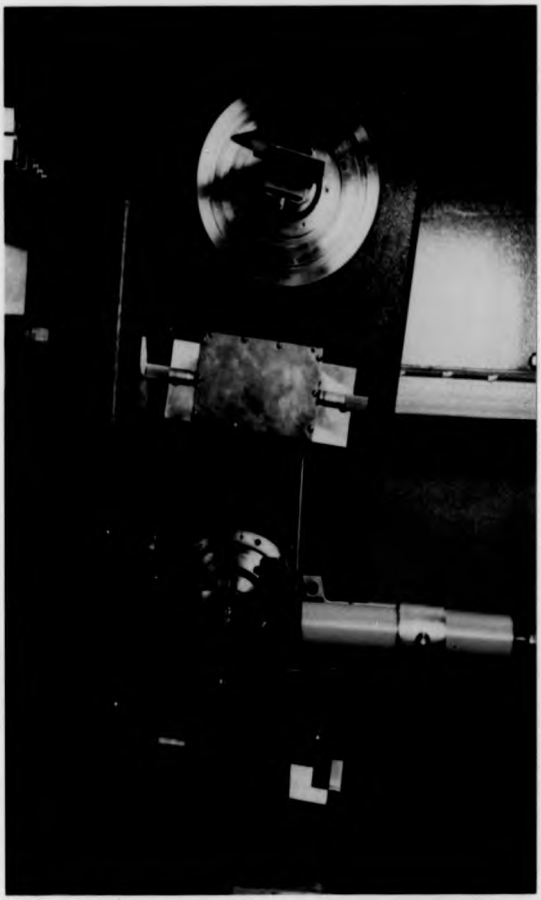

Photo 5.2. The double-crystal diffractometer at Daresbury Synchrotron Radiation Source.

(1983) in the topography station on beamline 7.6. The diffractometer was mounted to give a vertical dispersion plane. Alignmment to a high precision was possible with the use of a laser set up along the same axis as the the synchrotron beam.

5.1.2 Alignment.

For double-crystal diffractometry, the crystals must be aligned so that the incident and diffracted beams lie in a plane parallel to the difractometer surface and intercept the diffractometer axes (defined in Chapter 2). The diffractometer and x-ray source must first be aligned so that the x-ray beam is parallel to the diffractometer surface and intercepts the first and second axes.

First crystal.

The diffractometer is set at 2θ and the first (reference) crystal at θ (where θ is the Bragg angle). The detector is set at zero (or 2θ relative to the incident beam). The first crystal is scanned to find the Bragg peak. The tilt and rotation of the first crystal must be set so that the diffracted beam is parallel to the diffractometer surface and intercepts the second axis. The tilt may be adjusted using a slit parallel to the diffractometer surface, mounted on the second axis, at the same distance from the diffractometer as the incident beam. The tilt is scanned to find the position where the intensity is maximum. The diffractometer rotation (2θ) must then be adjusted so that the diffracted beam passes exactly over the second axis, using a slit perpendicular to the diffractometer surface. The diffractometer and first crystal are rotated in equal and opposite directions until the intensity is maximum. Alternatively, the alignment of the first crystal may be checked using a pointer of the correct length in the second axis and imaging the beam using x-ray film or an image intensifier.

If a multiple-reflection beam conditioner of the Bonse-Hart type (section 5.1.3) is used, the alignment is the same, except that there is a spatial offset between the incident and exit beams. This can be accommodated either by rotating the diffractometer so that

the exit beam again intercepts the second axis or, if the x-ray tube is moveable, by moving it so that the diffracted beam emerges along the diffractometer axis. If the number of reflections is odd, the diffractometer is set at 2θ and if it is even, the diffractometer is set at zero (or at a small angle to accommodate the step).

Second crystal.

To align the second (sample) crystal, the detector is moved through -2θ and the sample is set at $-\theta$ and scanned to find the Bragg peak. The tilt must then be adjusted to bring the diffraction vector (Bragg plane normal) into the diffractometer plane, so that it is parallel with the diffraction vector of the reference crystal. Any tilt deviation will broaden the Bragg peak, though the integrated intensity remains constant. Hence the correct tilt position is where the Bragg peak intensity is maximum, corresponding to a minimum in peak width. If the crystal is tilted and the Bragg peak scanned, the direction in which the Bragg peak moves and the direction in which to tilt to increase the peak intensity may be determined. Further tilting and Bragg peak scanning until the intensity is maximised will result in the optimum tilt setting.

Fewster (1985) describes an iterative method of tilt alignment, where the tilt angle is scanned, giving a single peak if the crystal is on the low-angle side of the Bragg angle and two peaks if it is on the high-angle side, for which the correct tilt position is midway between. The optimum tilt setting may therefore be reached by rotating the crystal and scanning the tilt angle.

Tanner, Chu and Bowen (1986) describe a high-speed, high-precision method of tilt optimisation which may be used if a sample rotation stage is available. The crystal is rotated about an axis almost normal to the Bragg planes. Provided the Bragg angle is within the misalignment angle of the Bragg planes, there will be two positions at which the Bragg condition is satisfied, and the optimum tilt is midway between these.

For rocking-curve measurements, the x-ray beam should be small (around 0.5 mm

diameter) to minimise the effect of sample curvature, which broadens the rocking curve since each part of the illuminated area on the sample diffracts at a different angle. Background noise must be reduced as much as possible by using shielding around the first crystal and narrow slits between the two axes, taking care not to intercept the beam. This ensures that the detector "sees" only the diffracted beam from the sample, and is especially important in diffuse scattering measurements in the rocking-curve tails, where the count rate is very low (Chapter 6).

Effective shielding is also important in x-ray topography experiments, where background noise will fog the film. Extreme care must be taken when using synchrotron radiation, especially if weak reflections are used, which give low intensities compared to the background (Chapter 7).

5.1.3 Multiple-reflection beam-conditioner design.

The range of angles of incidence accepted by a Bonse-Hart n-reflection beam conditioner decreases with increasing n.

$$\frac{\tan\theta_{max}}{\tan\theta_{min}} = \frac{n+1}{n-3} \qquad n>3 \qquad 5.1$$

for symmetric reflections, where θ_{max} and θ_{min} are the maximum and minimum angles of incidence. If $n \leq 3$, the range of angles is 0° to 90°, provided the crystals are large enough.

Beam conditioners should be mounted to give rotation about the point of intersection of the two limiting incident beams (figure 5.1), as first suggested by Rodrigues (1979). This enables them to be set to different Bragg angles simply by rotation.

Four-reflection channel-cut beam conditioners, designed for a range of wavelengths, from Mo 004 (15.14°) to Cu 004 (34.56°), were cut from a single block of silicon, with a strain-relief cut for mounting, and etched to remove sawing damage (photograph 5.3).

Photo 5.3. A four-reflection beam conditioner with a strain-relief cut for mounting.

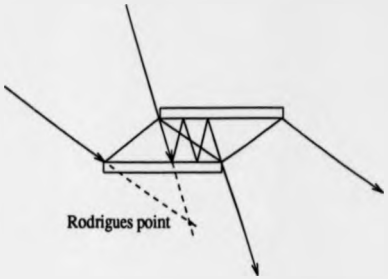

Figure 5.1 Four-reflection beam conditioner. Range of reflection.

5.1.4 Experimental instrument functions.

A double-axis rocking curve of a polished and etched silicon wafer, taken using a silicon four-reflection beam conditioner with the 004 reflection and CuKα radiation is shown in figure 5.3. The auto-correlation instrument function was measured by placing an identical four-reflection beam conditioner in the sample position (figure 5.2). This gave a tailless rocking curve of width (FWHM) 4 arc seconds, which is close to the theoretical. The suppression of the tail intensity can clearly be see in figure 5.4.

5.1.5 Double-crystal topography.

To image a large area of a crystal, it may be necessary to use either a broad source or an asymmetrically-cut first crystal. A line source may be used, either from a sealed tube or a rotating anode. Synchrotron radiation has the advantages of high intensity, giving very short exposures (of the order of minutes, unless a very weak reflection is used), low divergence, giving high strain sensitivity, and tuneable wavelength, allowing experiments at grazing incidence or near absorption edges.

An asymmetrically-cut first crystal can be used to expand the beam. This causes a reduction in intensity but decreases the divergence, giving higher strain sensitivity. In grazing-incidence topography it is more important to have a narrow, high-intensity

Fig. 5.3. Instrument function. 4-reflection beam conditioner.

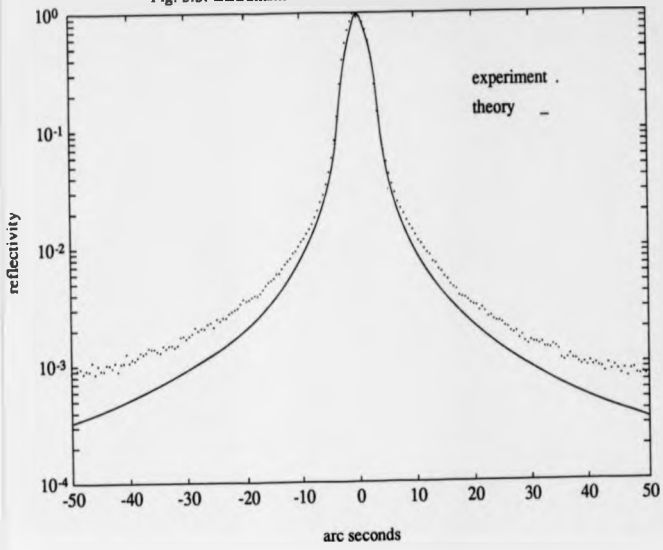

Fig. 5.4. Instrument function. Pair of 4-reflection beam conditioners.

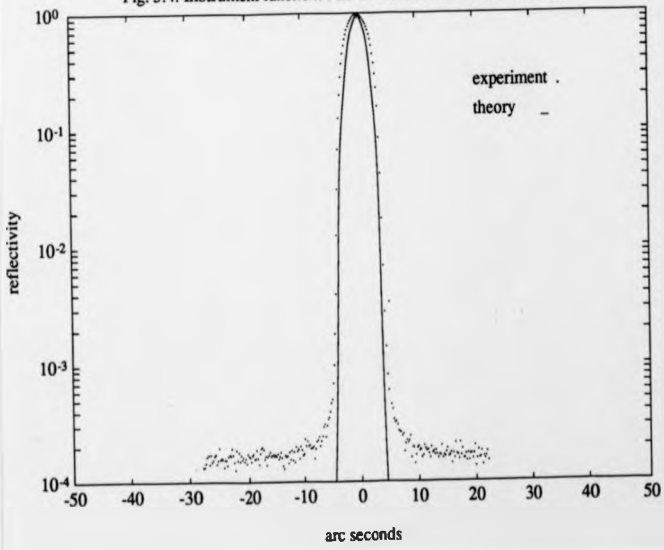

Figure 5.2 Double-axis diffractometry.
Measurement of instrument functions.

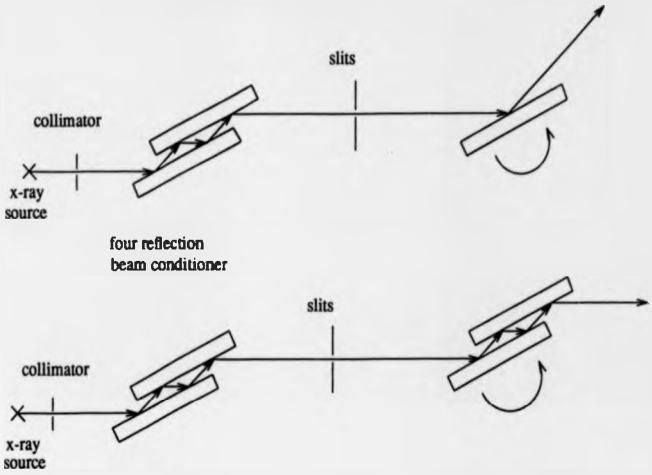

incident beam since this will illuminate a large area of the sample. This can be achieved by using the first crystal in grazing exit to contract the beam.

Alignment for double-crystal topography is the same as described in section 5.1.2. The crystal is set on the rocking curve peak and a photographic plate is placed in the diffracted beam, in front of the detector. Maximum strain sensitivity may be obtained by setting the crystal at the steepest part of the rocking curve flank, where the change in intensity with orientation is greatest. The tilt setting is important, otherwise the crystal will not diffract over the whole illuminated area. If the crystal curvature gives rise to a range of Bragg angles greater than the rocking-curve width, only a narrow strip will be imaged. The crystal can then be rotated in steps so that each part diffracts in turn to build up a Bragg angle contour map (Renninger, 1962, 1965). A topograph is taken by placing a film close to the sample and perpendicular to the diffracted beam. Exposures are up to

several days with a sealed-tube source. Such long exposures require monitoring of the signal through the photographic plate to ensure that the crystal does not drift off the peak.

If the strain sensitivity is high, images of defects are broad and high spatial resolution is not necessary. Faster, lower resolution films can therefore be used. Ilford nuclear emulsion type G5 is considerably faster than L4, but gives about 1μm resolution, compared to 0.25μm for L4. Thick emulsions of 50-100 μm are necessary to absorb short wavelengths and decrease the exposure time. Agfa D2, D4 and D7 can also be used, where the number signifies the grain size in microns and the film speed increases with grain size.

To obtain high strain sensitivity, great care must be taken with stability. The x-ray tube and diffractometer should be isolated from any vibration and the temperature should be kept stable. The samples should be mounted kinematically, or with a small amount of wax at one point only, to avoid unnecessary strains.

5.2 Determination of damage depth by etching.

5.2.1 Introduction.

Damage depth profiles may be determined by measuring etch rate as a function of depth (Tuck, 1975; Ives and Leung, 1988). Strained or damaged material etches at a higher rate than damage-free material, due to the larger surface area and the favourable release of strain energy. If the surface is damaged and the bulk is relatively damage-free, the etch rate decreases until all damaged material is removed and a constant etch rate is achieved. The depth at which the etch rate becomes constant gives an indication of damage depth.

Etching has been called an "art" since it is so sensitive to small changes in the conditions and results may vary even between two different people using the same etching technique. Various methods for etching and measurement of depth etched have been used. Schwartz and Robbins (1959) used a micrometer screw gauge to measure the decrease in thickness of silicon etched in HF–HNO_3. Ives and Leung (1988) initially used the measurement of weight loss to determine depth etched, and later developed a method using laser interferometry for measuring the depth of gallium arsenide removed while etching with bromine-methanol in an optical flow cell.

In order to determine etch rates for removal of damaged material and for sub-surface characterisation of machined and polished silicon, several experiments were necessary, involving the measurement of etched depths down to less than a micron. A widely used etchant for silicon is HF–HNO_3 (Schwartz and Robbins, 1976; Kern, 1978), which etches at room temperature. Etching rates for various etchants at different concentrations are given in the EMIS review of properties of silicon (1988). The above techniques for measurement of depth etched were unsuitable for application to silicon etched in HF–HNO_3 with etched steps of less than a micron. Interferometry methods would require an etching cell made of a transparent material, such as glass or perspex, both of which react with HF–HNO_3. A micrometer would not have a high enough

precision for the measurement of such small etched steps, so a Rank Taylor Hobson Form Talysurf was used. The possibility of using a capacitative flow etching technique for measurement of thickness change was considered, but it was found to have too low a sensitivity for this application.

5.2.2 Etching experiments.

Machined and polished (001) silicon was etched in steps using hydrofluoric acid (40% HF) and nitric acid (70% HNO_3), in the proportions 1:99, 5:95 and 10:90. The machined silicon was cut using a diamond saw and the polished silicon was commercially polished using a mechanical-chemical process. Etching was performed in a Teflon beaker and the reaction was stopped by immersing the sample in a beaker of cold water. After etching each step, the silicon was rinsed in distilled water and dried and a strip was masked using stopping off lacquer. Etch rate is extremely sensitive to rapidity of agitation and quite sensitive to temperature, so every attempt was made to keep these constant. The silicon was held with tweezers and vigourously agitated and the beaker of etchant was placed in a constant temperature water bath. Etching generates heat and because of the low thermal conductivity of the Teflon beaker, it was difficult to maintain a steady etchant temperature. Each experiment was repeated to check the reliability of the results. The step sizes were measured using a Rank Taylor Hobson Form Talysurf and the etch rate for each step was plotted against the total depth etched.

5.2.3 Results.

All samples gave an initial etch rate which was much higher than the final, steady etch rate. The depth at which the etch rate became steady was greater for the as-sawn sample than for the polished sample, implying a greater depth of damage, as expected. Etch steps of less than a micron and etching times of less than a few seconds were difficult to measure accurately and gave spurious results. The graphs of etch rate against depth are shown in figure 5.5, for HF concentrations of 10%, 5% and 1% at temperatures

of 18° , 15° and 20° .

Fig.5.5. Etch rate against depth etched. HF(40%):HNO3(70%).

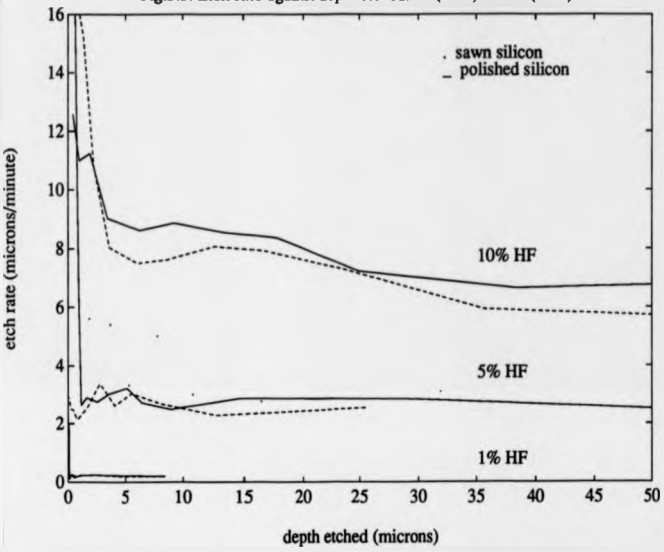

The final, steady etch rates are 6.4, 2.5 and 0.2 μm/minute respectively.

5% *HF* is the optimum concentration to use for removal of damaged material from as-sawn silicon. It gives a smooth, specular surface with few etch pits, after several hours etching. Higher concentrations (10% *HF*) give a pitted, "orange-peel" surface texture. 1% *HF* may be used to remove very small amounts of material in a controlled manner, useful for characterisation of sub-surface damage. Generally, the lower the concentration of *HF*, the slower the reaction and the smoother the surface generated.

5.2.4 Discussion.

In the HF–HNO_3 system, the HNO_3 oxidises the silicon and the *HF* attacks the oxide. When the concentration of *HF* is low (less than 50%), a decrease in *HF* causes a

decrease in the rate of reaction, implying that the etch rate is controlled by the diffusion of HF to the silicon surface (Schwartz and Robbins, 1959; Tuck, 1975; Kern, 1978). Diffusion limited reactions etch all crystallographic planes at the same rate and therefore give flat, planar surfaces. If there is greater access to the surface for the diffusion of *HF*, the etch rate will increase. This effect may be seen at edges and corners, which etch preferentially, giving surfaces which are far from flat. If the reaction becomes violent, such as when there is a concentration of *HF* greater than 10%, bubbles of gas form and some points on the surface will have a higher dissolution rate, creating pits or holes. If there are dislocations at the surface, these will form etch pits.

Damage produced by abrasion on silicon, such as that caused by diamond sawing, comprises a combination of plastic deformation, dislocations and cracks. (Puttick and Shahid, 1977). These defects are surrounded by strain fields, which cause an increase in etch rate, due to the favourable release of strain energy. Damaged surfaces also present a larger surface area to the etchant, where the reaction can proceed at a higher rate. Mechanical-chemical polishing is a combination of abrasion and etching used to produce surfaces which are both flat and specularly smooth. This process may result in a low level of strain or damage in the surface.

Referring to the results obtained for the as-sawn silicon, the damage depth is estimated, from the point at which the etch rate becomes steady, to be about 10 μm. For the polished silicon, the high initial etch rate shows that there must be strain or damage in the top micron below the surface.

Chapter 6

6. Double-axis x-ray rocking-curve analysis.

6.1 Introduction.

Double-axis x-ray diffractometry may be used to detect strains of the order 10^{-6}, with depth resolution down to around 50 nm, near the surface of single-crystal semiconductor materials.

It is well known (Afanas'ev, 1984) that information on very thin sub-surface layers (down to 10 nm) may be found in the tails of the Bragg reflection curve (Chapter 3). By using a four-reflection, non-dispersive beam conditioner to give a tailless reflection curve (Bonse and Hart, 1965), information on surface scattering from the sample may be obtained from the tails of the double-axis rocking curve. A strong reflection must be used to give enough intensity in the tails (with a conventional x-ray source), and a long wavelength for low extinction depth and surface sensitivity.

Surface symmetric reflections give information on strains perpendicular to the surface, while asymmetric reflections also give information on strains parallel to the surface. However, the surface of the crystal is constrained by the underlying bulk crystal so that strain is only in a direction perpendicular to the crystal surface. This introduces a Poisson effect. If the strain exceeds the elastic limit, misfit dislocations are introduced in the layer-bulk interface, producing strain parallel to the surface. In the following experiments, it was expected that the strains would be very small, in the elastic range. A surface symmetric reflection was therefore chosen, which measured strain perpendicular to the surface only.

X-ray double-axis rocking-curve analysis was used to characterise the residual surface strain or damage left by the mechanical-chemical polishing process by which high-quality silicon wafers are produced. To demonstrate the range of applications of this technique, silicon epiwafers (heavily doped wafers with more lightly doped epitaxial

layers) and ion implanted silicon wafers were also investigated.

6.2 Experiments.

The samples were (001) silicon wafers which had been polished using the mechanical-chemical process described in Chapter 1. To determine whether there was significant strain or damage induced in the polishing process, rough-polished and fully-polished wafers were compared before and after etching in steps of 1 μm (a 5 minute etch in 1% HF (40%): 99% HNO_3 (70%)). To find whether any improvement could be made, silicon wafers which had been polished using different processes, or under different conditions were investigated. Silicon wafers with homoepitaxial layers were also investigated to compare as-grown surfaces with polished surfaces. To demonstrate the sensitivity of the technique, commercially polished wafers from a number of different vendors were compared.

The experiments were performed using the diffractometer and instrumentation described in Chapter 5. The experimental set-up is shown in fig 6.1.

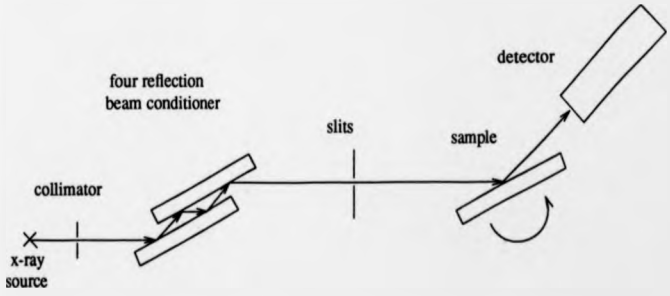

Figure 6.1 Double-axis diffractometry. Experimental set-up.

The 004 reflection was used with $CuK\alpha_1$ radiation, giving a surface symmetric

reflection with Bragg angle $\theta = 34.56°$. The extinction depth was 16.8 μm, though the scattering intensity in the tails 20 rocking-curve widths away from the Bragg peak was mainly from the the top 0.8 μm. The four-reflection beam conditioner was channel cut from a single block of silicon, with a strain-relief cut for mounting, and etched to remove sawing damage. The experiment was set up in the (+,−,+,−,+) parallel geometry which is non-dispersive in wavelength. A 0.5 mm diameter collimator was used, which gave a beam size of 0.5×4 mm^2 at the sample, due to horizontal beam divergence. The x-ray generator was run at 45 kV, 35 mA. The background was reduced as much as possible without intercepting the beam, by placing narrow (5 mm) tungsten carbide slits and lead perspex shielding between the two axes. The background noise was measured with no sample or sample mount and found to be 0.1 counts per second, compared with peak intensities of 45,000 counts per second. The temperature in the laboratory was kept stable at 23°C.

The samples were mounted kinematically to prevent them from being strained. Rocking curves were taken along the [110] and [100] directions, and at 90° and 180° rotations. The Bragg peak was scanned up to 150 arc seconds on either side, in steps of 0.5 arc seconds, with total data collection times up to 8 hours to give good counting statistics in the tails.

6.3 Results.

The results presented in this section have not been normalised. Theoretically, by conservation of energy, the total scattering remains constant (a decrease in peak intensity plus an increase in diffuse scattering intensity) and the rocking curve can be normalised by dividing by the integrated intensity (the area under the peak). However, some of the diffuse scattering intensity appears far from the Bragg peak (Chapter 3). It was therefore decided that the rocking curves should not be normalised, since the range in most cases was only 100 arc seconds on either side of the peak. It was found in any case that normalising had little effect on the results.

Figure 6.2. Rough polished and etched silicon wafer.

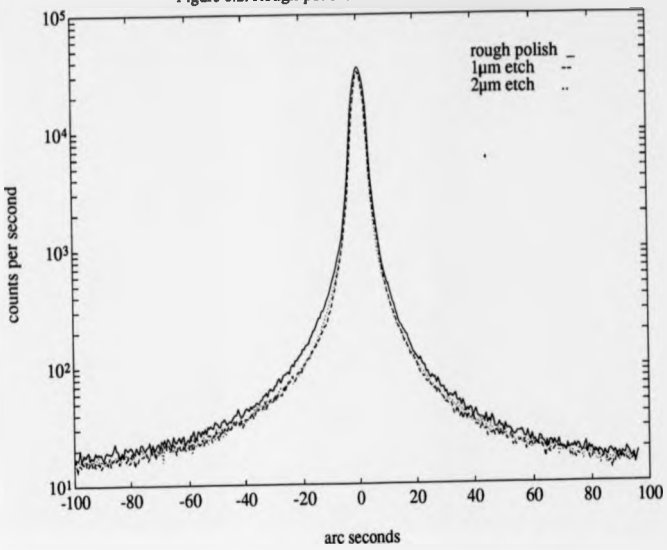

Figure 6.3. Fully polished and etched silicon wafer.

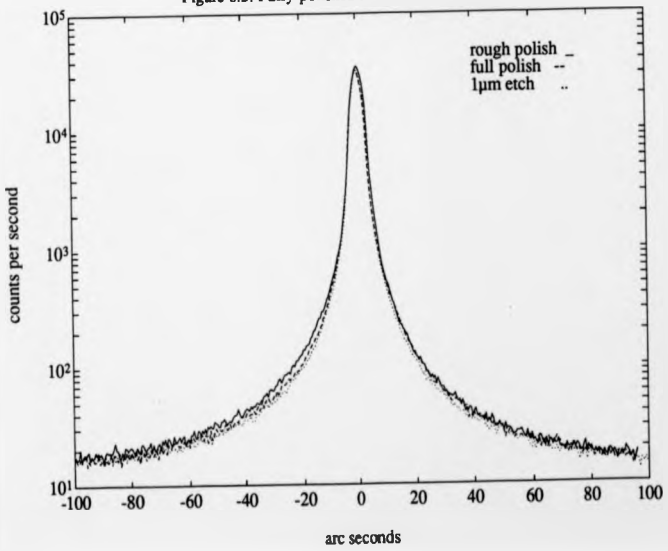

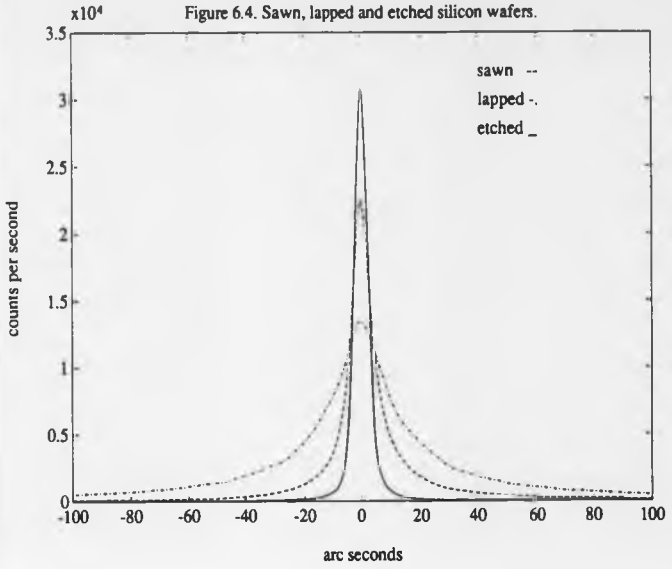

Figure 6.4. Sawn, lapped and etched silicon wafers.

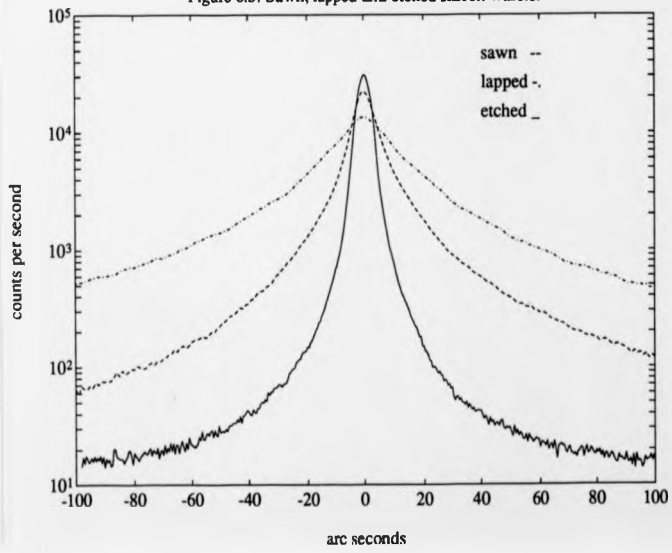

Figure 6.5. Sawn, lapped and etched silicon wafers.

6.3.1 Mechano-chemically polished silicon.

The silicon wafers characterised were p-type (boron doped) with resistivity in the range 11 to 16 Ωcm (7.8×10^{14} to 1.4×10^{15} atoms/cm^2) and a typical oxygen concentration of 14 ppm (7×10^{17} atoms/cm^2). The wafers were (001) orientation, to within about 0.2° (unless stated otherwise). Figure 6.2 shows rocking curves from a rough-polished wafer which was then etched to depths of 1 μm and 2 μm to remove strain and damage. There was no significant difference in the rocking-curve tail intensities produced by the 1 μm and 2 μm etching treatments, which implies that most of the residual strain is in the top micron below the surface. Topographs of this wafer are shown in Chapter 7. The scattering in the rocking-curve tails is greatly reduced in fully polished wafers. A rocking curve from such a wafer is shown in figure 6.3, which compares rough-polished, fully polished and etched wafer rocking curves.

The plots are shown on a log-linear scale. Most of the scattering in the tails appears between 5 and 75 arc seconds, or approximately 1 to 15 rocking-curve widths from the Bragg peak maximum, with more intensity on the low angle side of the peak, implying a lattice expansion at the surface.

For comparison, rocking curves from severely damaged (as-sawn and lapped) wafers are shown in figures 6.4 and 6.5 (linear and log-linear plots), compared with an etched wafer. The full widths at half maximum (FWHM) of these rocking curves are 9" for the as-sawn, 24" for the lapped and 5" for the etched wafer.

Comparison of commercially polished wafers.

Figures 6.6, 6.7 and 6.8 are comparisons of rocking curves from wafers from different vendors. The wafers were 6 inch (150 mm), except for those from vendors C and D, which were 4 inch (100 mm). Wafers B1 and B2 come from two different batches from the same manufacturer. These and wafers D and E have all been polished by nominally the same process but at different sites. The wafer from vendor E was found to

Figure 6.6. Commercially polished silicon wafers.

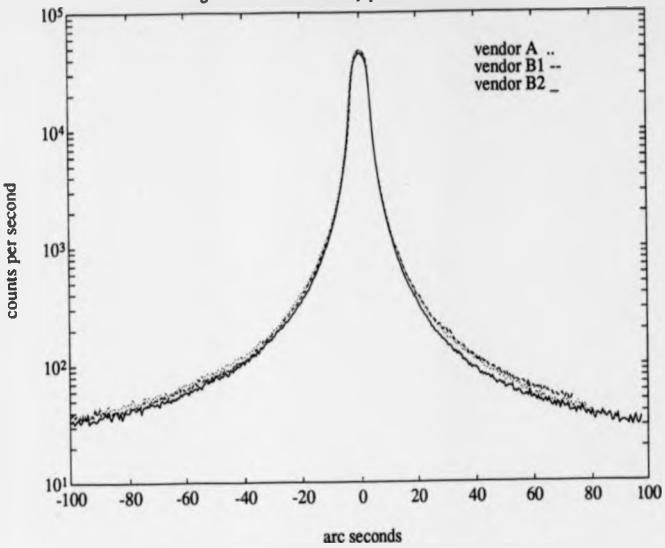

Figure 6.7. Commercially polished silicon wafers.

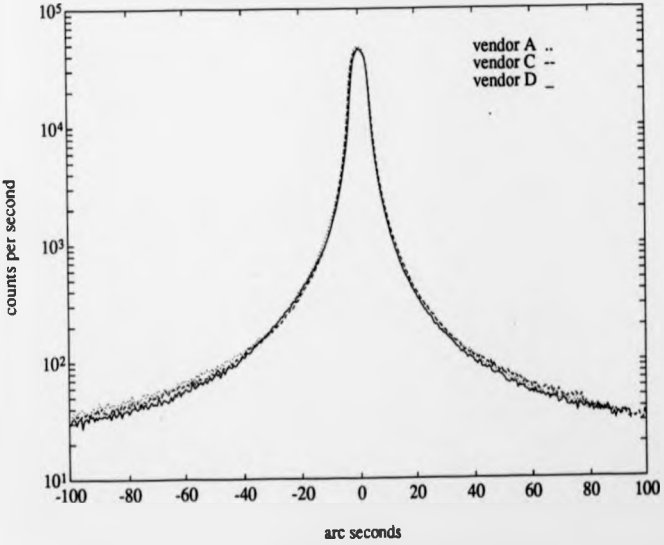

Figure 6.8. Commercially polished silicon wafers.

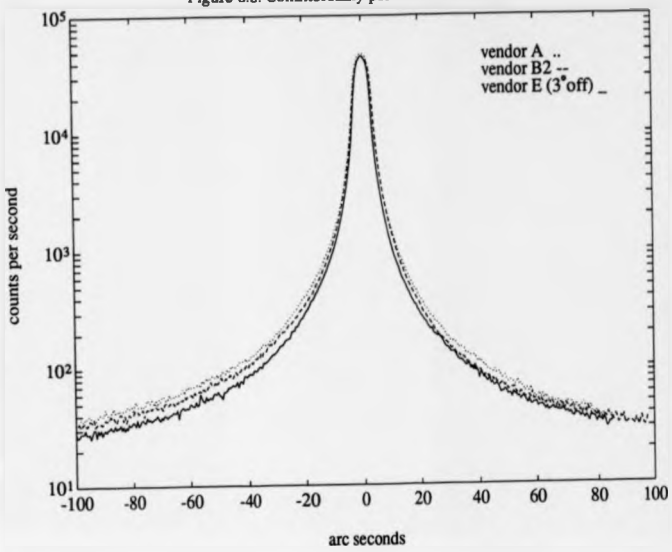

Figure 6.9. Comparison of polished wafers with etched wafer.

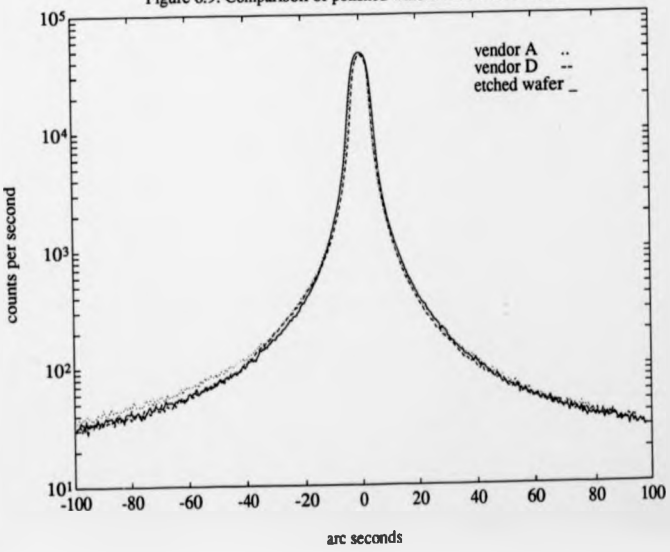

be orientated approximately 3° from the other wafers. This caused an increase in the angle of incidence of x-rays and hence a decrease in the rocking curve width and tail intensity. Wafers B2 and D gave the lowest overall scattering intensities in the tails (apart from wafer E). The wafer from vendor A gave the highest tail intensity and is shown for comparison in each figure. In figure 6.9, wafer A is compared with the etched wafer from figure 6.2 (etched 2 μm). It should be noted that, although the etched wafer rocking curve in figure 6.9 has a greater FWHM than wafers A and D (possibly due to an incorrect tilt adjustment, sample curvature or surface roughness), the scattering intensity in the tails decreases to less than or equal that of the polished wafers.

The rocking curves in figures 6.6 to 6.9, recorded in January 1990 have greater intensities and widths than those in figures 6.2 and 6.3, recorded in June 1989. This might have been caused by an increase in the x-ray power (due to repair of the previously faulty x-ray generator) and possible detector saturation. Therefore, the later rocking curves cannot be directly compared with the earlier ones. The rocking curve of the 2 μm etched sample in figure 6.2 was repeated for comparison in figures 6.9 and 6.11.

Effects of changing the polishing conditions.

Figure 6.10 shows rocking curves from silicon wafers which had been polished using deliberately varied polishing processes. A very small difference in scattering intensity in both tails of the rocking curves is observed between 20 and 60 arc seconds from the rocking-curve peak. Polish 2 gives a slightly lower tail intensity than polish 1. In figure 6.11, the rocking curves in figure 6.10 are compared with the rocking curves from the 2 μm etched wafer. A difference in scattering intensity can be seen in the low-angle tail, of magnitude similar to that observed in other fully polished wafers (above).

Evaluation of similar polishing processes was performed by Dr. G.R. Fisher (1988) by measurement of etch pit density from oxidation induced stacking faults at the surface of wafers polished by the different techniques. It was found that polish 2 produced fewer etch pits after oxidation than polish 1. Etching for 1 minute or 10 minutes in 1:100

Figure 6.10. Comparison of different polishing processes.

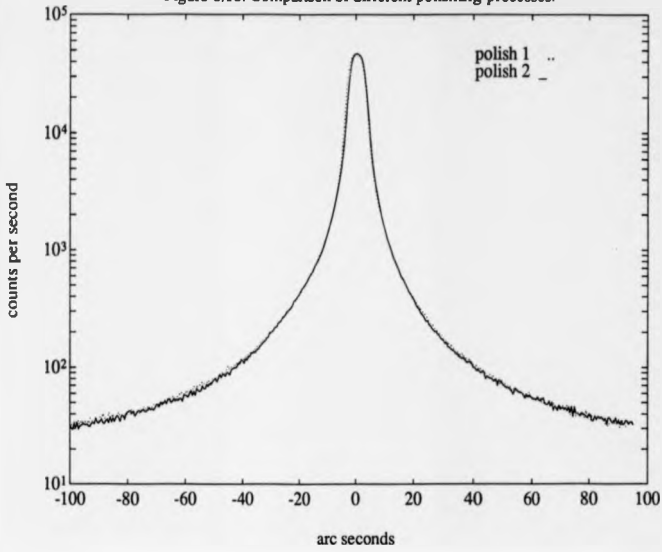

Figure 6.11. Comparison of polished wafers with etched wafer.

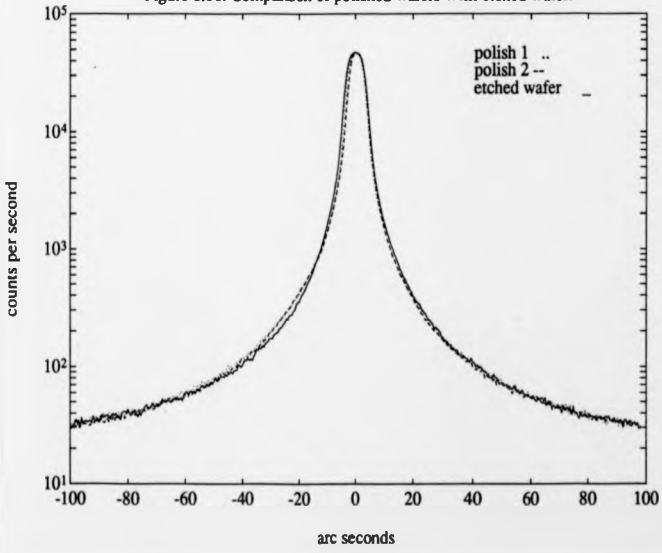

Figure 6.12. Comparison of wafers polished under different conditions.

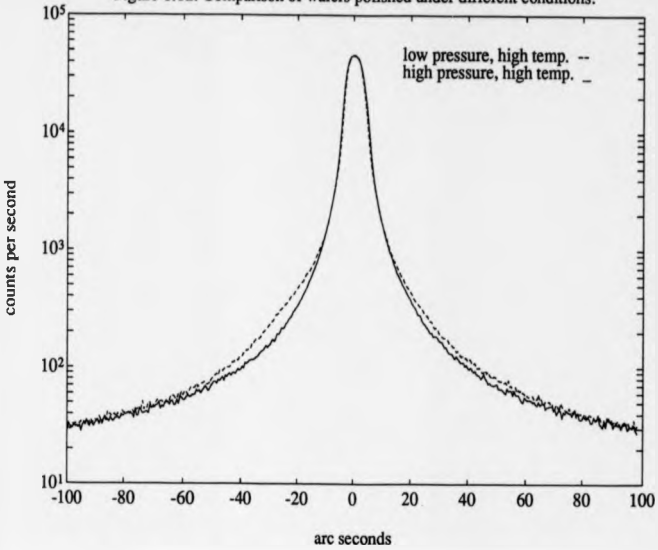

Figure 6.13. Comparison of wafers polished under different conditions.

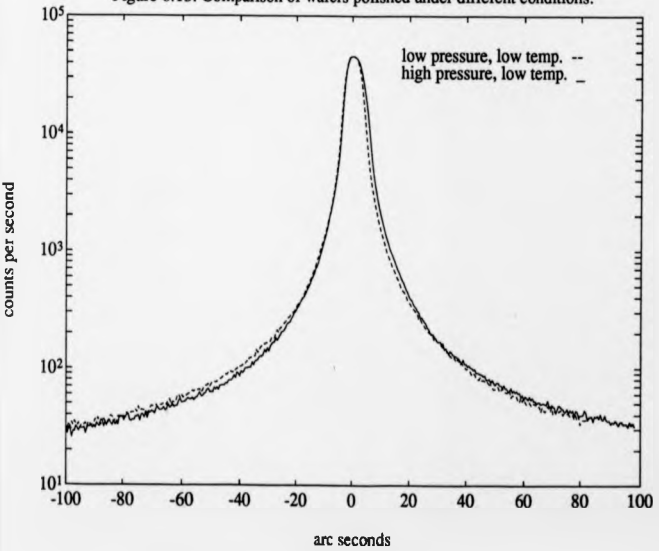

$HF:HNO_3$ before oxidation resulted in an even greater reduction in stacking fault density. This is in agreement with the rocking curve results presented above, since stacking faults are more likely to form on strained or damaged surfaces.

Figures 6.12 and 6.13 show rocking curves from wafers polished under different conditions, including different polishing pressures, temperatures and polishing pads. A new pad was used to polish the wafers in figure 6.12 and a used pad for those in figure 6.13. The rocking curves have large differences in the tail intensities (particularly in figure 6.12), showing that the polishing conditions do affect the wafer surface. The results obtained indicate that the polishing pressure is the most important factor, with higher pressures giving better results. However, there were not enough wafers available to carry out an extensive survey.

Float-zone silicon.

Float-zone silicon has a lower oxygen concentration than Czochralski silicon, from which most wafers are made. To reduce the scattering from oxygen-related defects so that most of the scattering intensity in the rocking curve tails would result from polishing strain or damage, rocking curves were measured from slices cut from float-zone silicon. These slices were etched and polished using the same method as ordinary commercial wafers. However, the slices were 3 mm thick, compared to around 0.6 mm for commercial wafers, and the polishing conditions were therefore different. Grazing incidence topographs of these silicon slices are shown in Chapter 7.

Figure 6.14 shows a comparison of an etched silicon wafer with float-zone silicon. The scattering intensity in the tails is reduced, particularly on the high-angle side. This is due to a decrease in diffuse scattering from oxygen-related defects which cause local lattice expansions in the bulk silicon (Chapter 3). Rocking curves of rough-polished and fully polished float-zone wafers are shown in figure 6.15. Slices of the same orientation were not available. An increase in miscut angle (and incidence angle) produces a decrease in rocking curve width and tail intensity. It is therefore difficult to distinguish

Figure 6.14. Comparison of etched wafer with float-zone silicon.

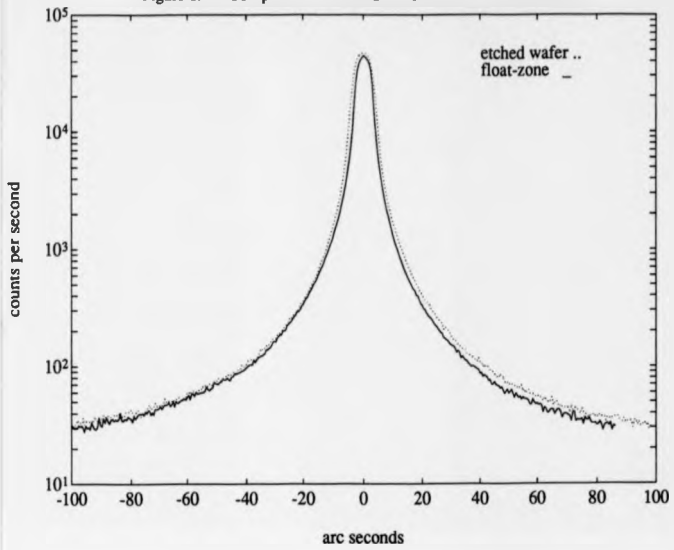

Figure 6.15 . Polished float-zone silicon with different miscut angles.

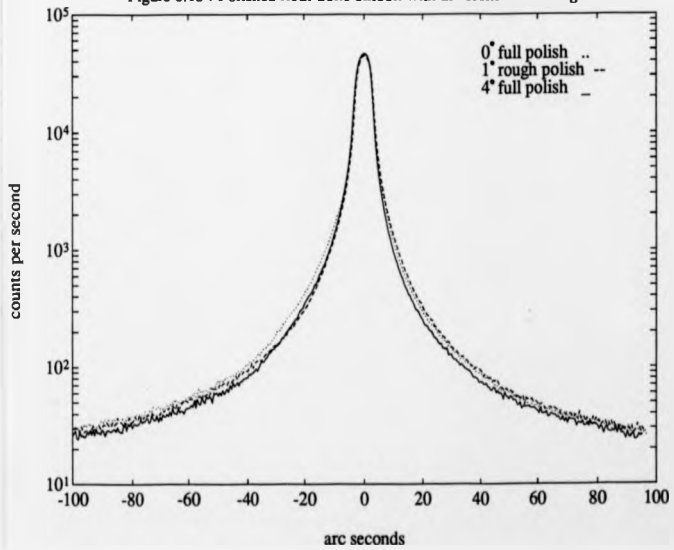

the effects of polishing from miscut, though it appears that the rough-polished wafer has higher intensity in the tails than the fully polished wafers.

6.3.2 Silicon epiwafers.

Rocking curves of p-type (boron doped) and n-type (phosphorus doped) silicon epitaxial layers grown on more heavily doped substrates are shown in figures 6.16 and 6.17. The resistivities were 10.3 / .017 Ωcm and 9.3 / .015 Ωcm for the P/P$^+$ and N/N$^+$ wafers respectively. The corresponding boron and phosphorus concentrations are approximately 10^{15} / 10^{21} atoms/cm^2 and 5×10^{14} / 5×10^{20} atoms/cm^2. Lattice strain is proportional to impurity concentration.

To check whether the layers were tilted relative to the substrate, four rocking curves were measured from each sample, at 90° rotations, shown in figures 6.18 and 6.19. The p-type epiwafer rocking curves (figure 6.18) are the same for all rotations, showing that there is no relative tilt. The upper left and lower right rocking curves in figure 6.19 have slightly different layer peak shifts (in the low-angle tail), showing that the n-type epilayer is slightly tilted in one direction. The n-type epilayer is thin and the peak is not resolved from the substrate peak, but can be seen in the low-angle tail. The p-type epilayer is relatively thick, and gives a peak of higher intensity than the substrate peak. Both layers are positively mismatched from the substrate. The sign of the mismatch depends on the size of the dopant atoms, and whether they are substitutional or interstitial. The layer thicknesses were determined, using fourier transform infra red measurements, to be 10.72 μm for the p-type and 9.9 μm for the n-type silicon.

6.3.3 Ion implanted silicon.

The ion implanted silicon was supplied by Prof. B.K. Tanner and implanted by T.A. Woods of Whickham Ion Beam Systems. There were two samples, implanted with nitrogen at 110 keV, one with a dose of 2×10^{13} N$^+$/cm^2 and the other with a dose of 2×10^{14} N$^+$/cm^2. The rocking curves are shown in figure 6.20. The higher intensity rocking curve

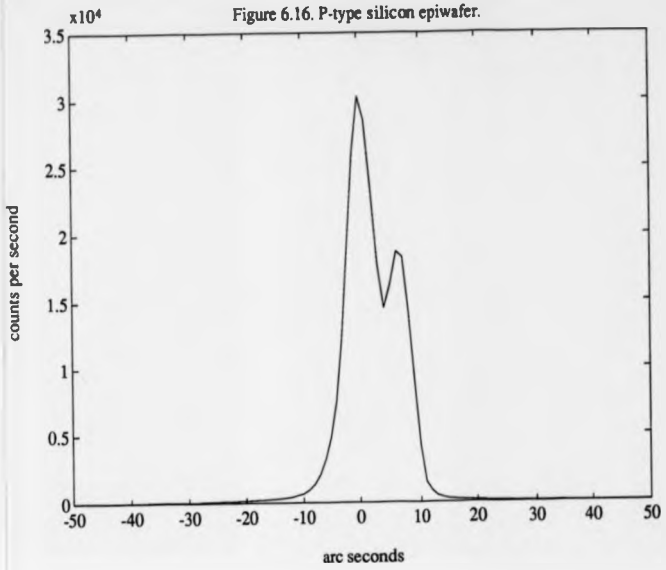

Figure 6.16. P-type silicon epiwafer.

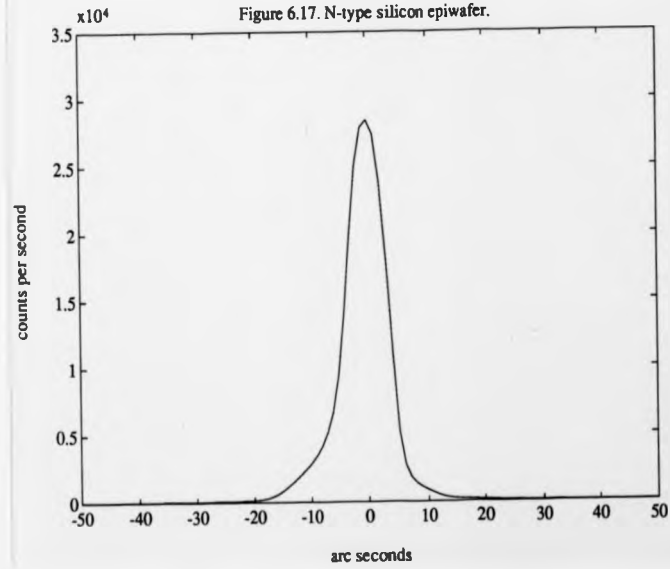

Figure 6.17. N-type silicon epiwafer.

Figure 6.18. P-type epiwafer rocking curves at 90° rotations.

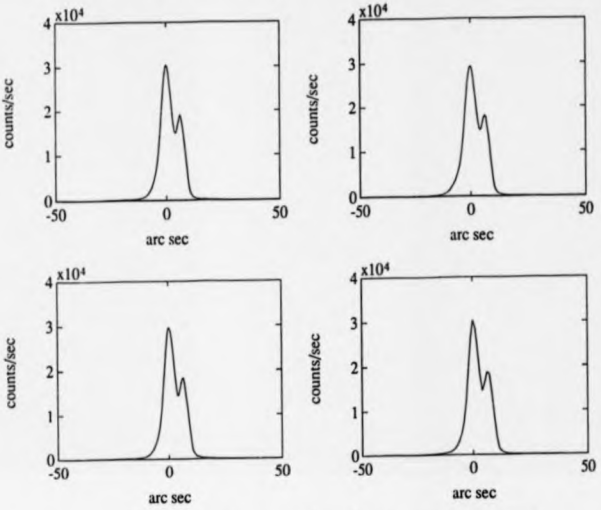

Figure 6.19. N-type epiwafer rocking curves at 90° rotations.

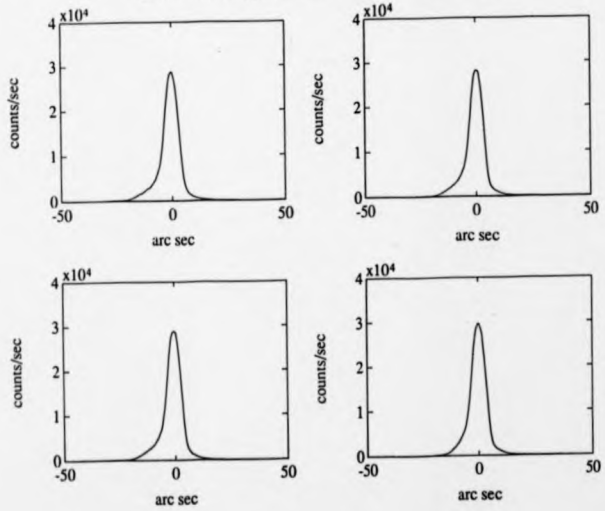

Figure 6.20 . Ion implanted silicon wafers.

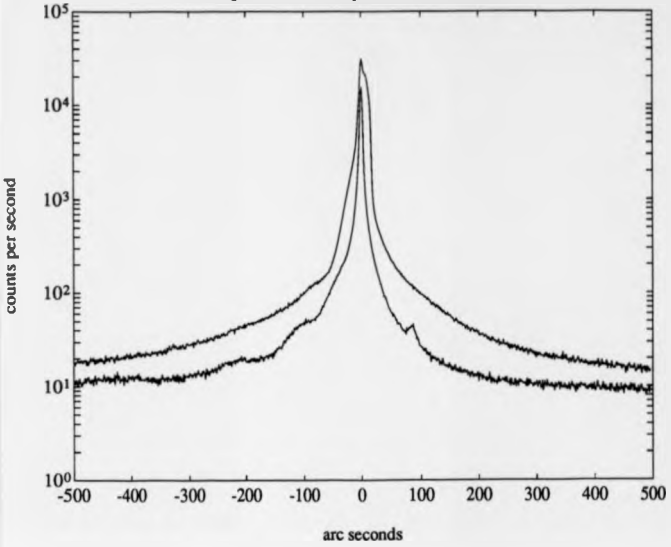

Figure 6.21. Comparison of experiment with theory (+ .00035 background).

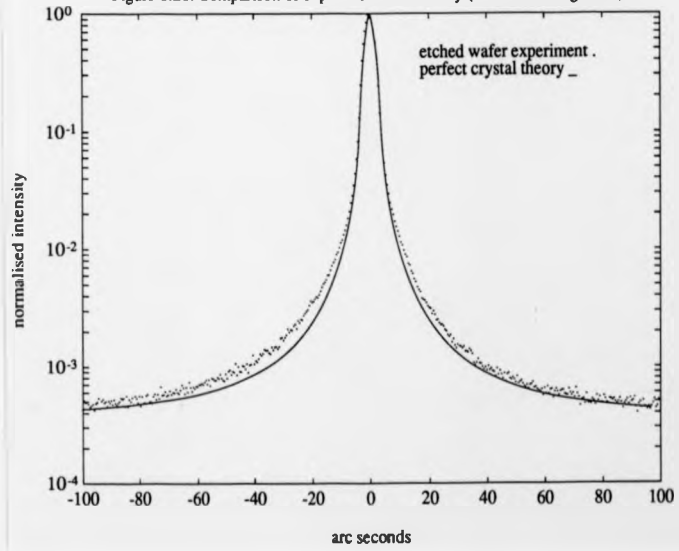

is from the lower dose sample (2×10^{13} N^+/cm^2) and the lower curve is from the higher dose sample (2×10^{14} N^+/cm^2). The decrease in intensity is due to the increase in damage caused by the higher dose implantation. Lattice strain and damage is proportional to dose. There could also be a buried amorphous layer which would not diffract x-rays. Pendellösung fringes can be seen away from the Bragg peak, showing that there is a thin strained surface layer introduced by the implantation. This was estimated from the fringe spacing to be about 0.2 μm.

6.4 Simulations.

Initial rocking-curve simulations were made using the program at Durham University, based on the solution of the Takagi-Taupin equations (Chapter 2). All subsequent simulations were made using the Bede Scientific Instruments RADS program. To simulate the reflection curve from the four-reflection beam conditioner, a perfect-crystal curve was raised to the fourth power. This was then cross-correlated with the reflection curve from the model sample to give a simulation of the rocking curve.

Experimental data from an etched silicon wafer were compared with a theoretical simulation of a perfect silicon crystal rocking curve, shown in figure 6.21. The difference in intensity in the tails could be due to sample curvature, thermal diffuse scattering and diffuse scattering from dopants or oxygen in the bulk silicon. A background of 12 counts per second, chosen by matching the background at 100 arc seconds away from the peak, has been added to the theoretical simulation. This is ascribed to background noise, including noise from the detector and electronics, scattering of stray x-rays and inelastic Compton scattering.

A number of different strain profiles was simulated in order to find any possible agreements with the experimental data. In the simulations, lattice mismatch was varied between 1 and 20 parts per million, with total layer thicknesses from 0.1 to 10 microns, assuming maximum strain at or near the surface. The strains reported here are relaxed strains, that is, if the layer were removed from the substrate and allowed to relax. The

Figure 6.22. Simulations. Single uniform layer. 0.2 μm thick.

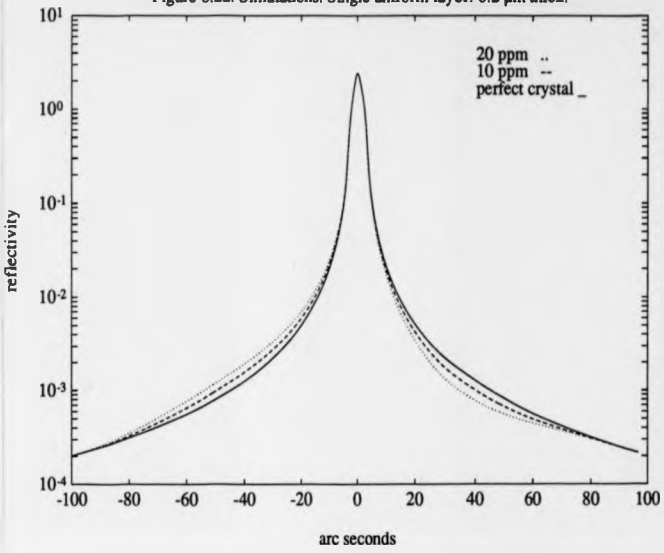

Figure 6.23. Simulations. Single uniform layer. 10 ppm.

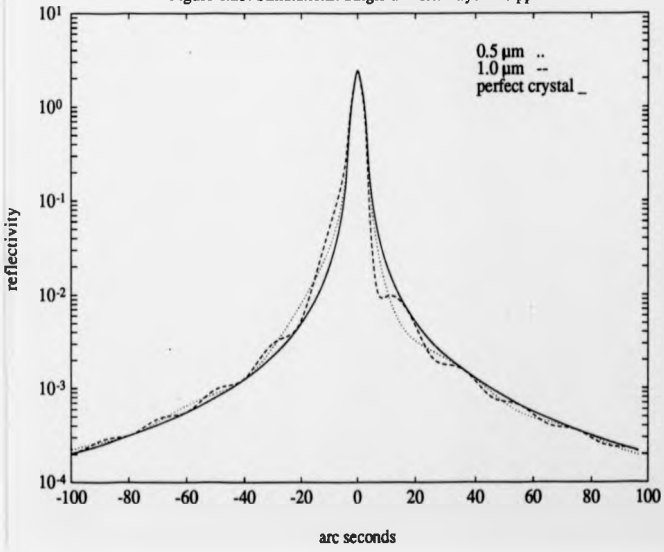

Figure 6.24. Simulations. Linearly graded layer. 1 μm thick.

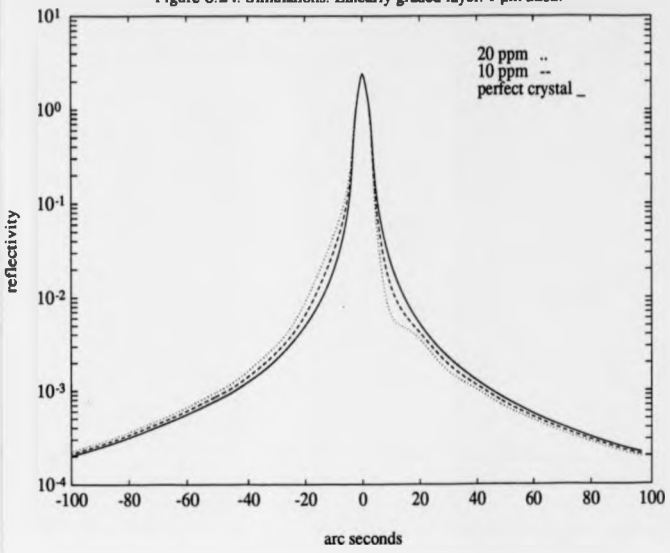

Figure 6.25. Comparison of linear and quadratic grading. 1 μm, 20 ppm max.

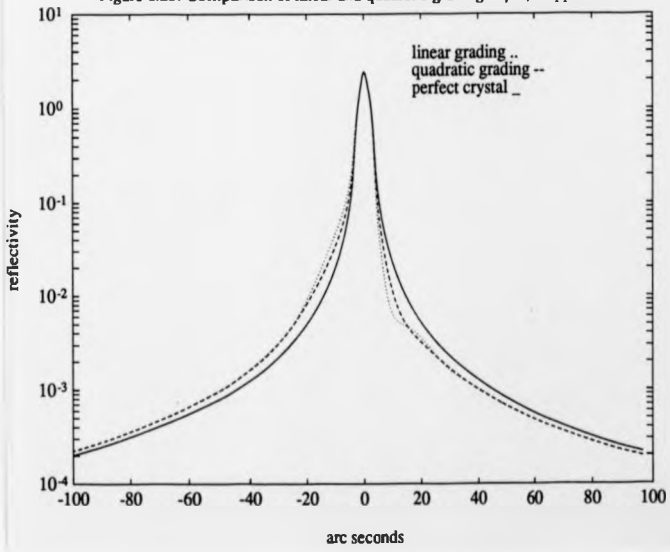

actual measured strains, of the layer on the substrate, are 1.77 times the values given.

Initial simulations are shown in figues 6.22 to 6.25. The strain-profile models used in figures 6.22 and 6.23 are single, uniformly strained layers. Figure 6.22 shows the effect of varying the lattice parameter of a 0.2 μm layer with 20 ppm and 10 ppm lattice strains. The strained layer produces an asymmetrical rocking curve, with an increase in intensity on the low-angle side and a decrease in intensity on the high-angle side, for a positive mismatch. A negative mismatch would give the opposite effect. The difference between the strained and perfect crystal simulations increases with mismatch. Figure 6.3 shows the effect of varying the layer thickness, for a lattice mismatch of 10 ppm. 0.5 μm and 1.0 μm give Pendellösung fringe spacings of 38.6 and 19.3 arc seconds. The fringes are smoothed out if a strain gradient is introduced. Figure 6.24 shows simulations from graded layers of 20 ppm and 10 ppm at the surface, decreasing linearly to zero at 1 μm depth. The strain-depth profiles are shown in figures 6.24a and b. The layer is divided into 20 laminae, each with a constant lattice parameter.

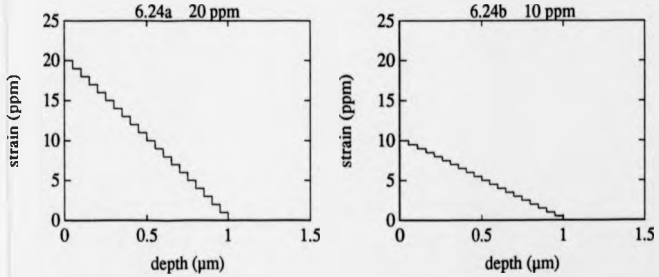

The difference between a linear grading and a quadratic grading is shown in the simulations in figure 6.25, of the strain profiles in figures 6.25a and b. A quadratic grading, with lattice parameter increasing as the square of the distance from the layer-substrate interface, gives a greater smoothing of interference fringes.

Figures 6.26 to 6.29 show simulations approaching the experimental rocking curve

Figure 6.26. Simulations. Graded layer. 10 ppm at surface.

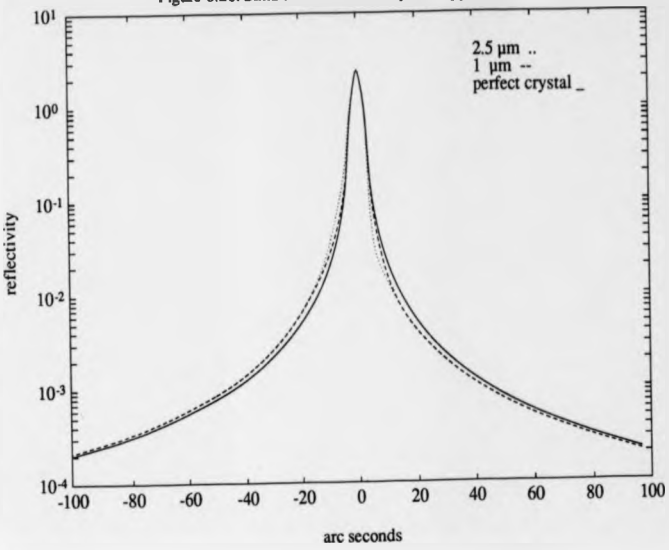

Figure 6.27. Simulations. Graded layer. 10 ppm at surface.

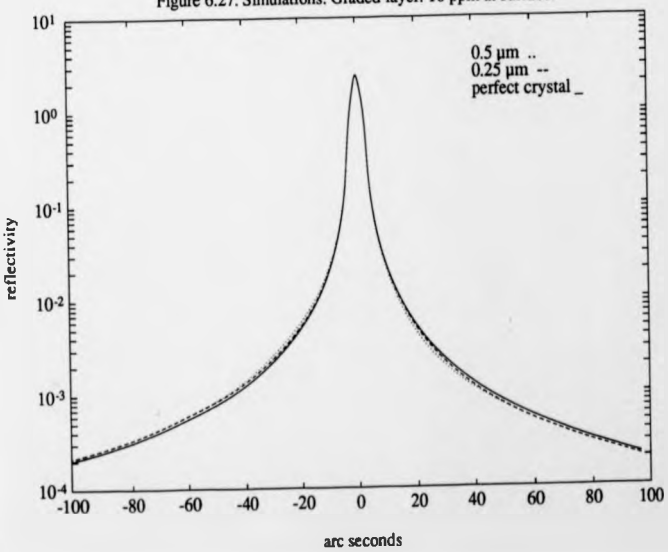

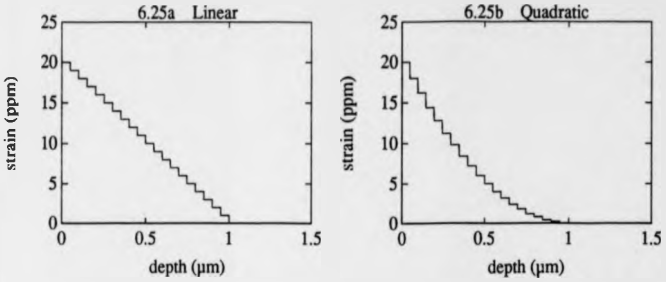

profiles. The strained layer is modelled by a positively mismatched graded layer, with lattice parameter increasing as the square of the distance from the layer-substrate interface and maximum strain at or near the surface. Figure 6.26 shows simulations from 2.5 μm and 1 μm layers with lattice strains of 10 ppm at the surface, compared with a perfect crystal. The strain profiles are shown in figures 6.26a and b.

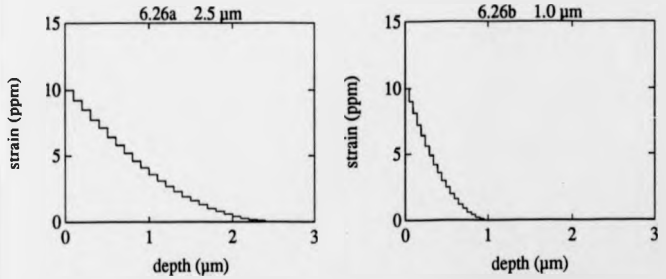

The difference in the tails of the strained and perfect crystal simulations decreases away from the rocking curve peak. The decrease in strained layer thickness from 2.5 μm to 1 μm causes the difference in intensity to move further down the tails, away from the rocking curve peak. This effect can also be seen in figure 6.27, which shows 0.5 μm and 0.25 μm strained layer simulations. The differences in intensity between the strained and perfect crystal simulations can now only be seen much further down in the tails. The

Figure 6.28. Simulations. Graded layer. 1 μm thick.

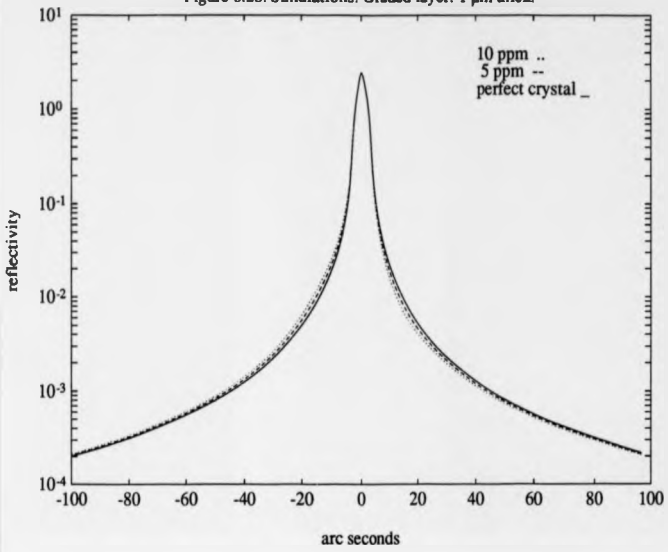

Figure 6.29. Effect of strain-free surface layer. Graded layer 1 μm, 10 ppm max.

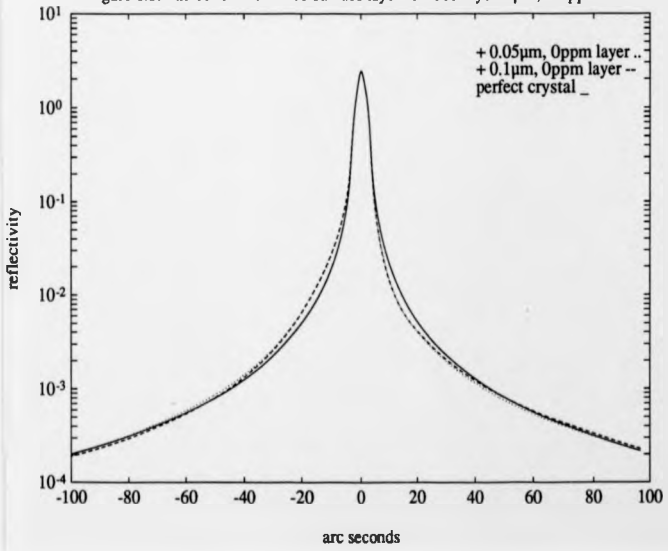

thickness of a strained surface layer can therefore be determined from the distance from the rocking curve peak of the extra tail intensity (see Chapter 3, equation 3.1). The sign of the mismatch depends on which tail has higher intensity.

Figure 6.28 shows simulations for a 1 μm layer with maximum strains of 5 and 10 ppm at the surface. These are similar to the experimental rocking curves from rough and fully polished wafers. The strain profiles are shown in figures 6.28a and b.

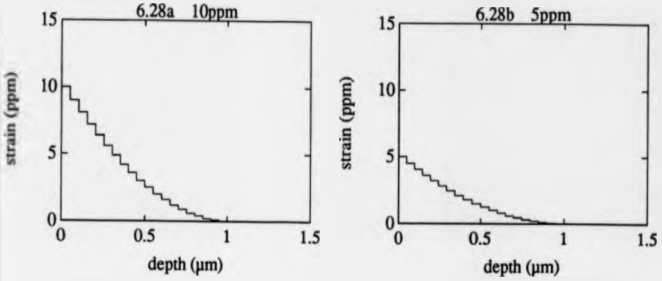

The effect of adding a surface layer of zero strain to the model was also investigated. Figure 6.29 shows simulations from a 1 μm strained layer with maximum strain of 10 ppm at 50 nm or 100 nm below the surface, as in figures 6.29a and b. As the thickness of the strain-free surface layer increases, the difference in tail intensity between the strained and perfect crystal simulations decreases to zero more rapidly. The thicker the surface layer, the closer to the rocking curve peak is its effect. Models with maximum strain below the surface consistently showed better agreement with experiment than models with maximum strain at the surface itself. An explanation for this is given in Chapter 9.

Several other strain-depth profiles were also tried in the simulations. Figure 6.30a and b shows strain profiles with positive strain up to 0.25 μm from the surface and negative strain between 0.25 μm and 0.5 μm depth. These are termed "Z" distributions. The resulting simulations are shown in figure 6.30. The simulation of 6.30a has Pendellösung fringes with a spacing of about 40 arc seconds. In the simulation of 6.30b,

Figure 6.30. Simulations. Z-distribution strain profiles. 0.5 μm thick.

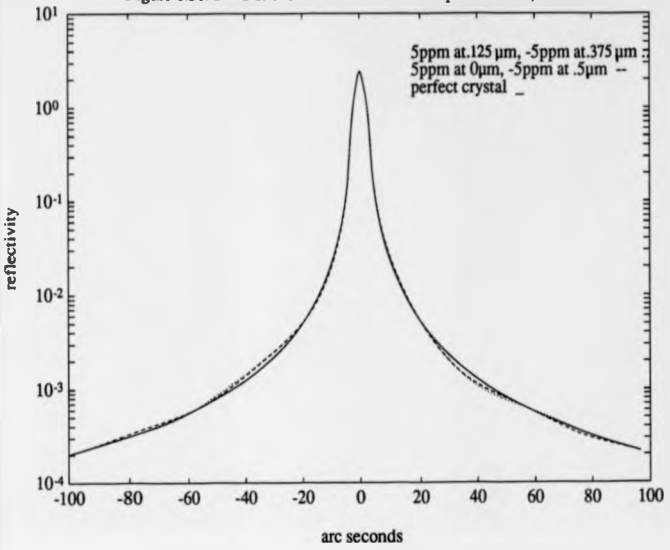

Figure 6.31. Simulations. Different miscut angles.

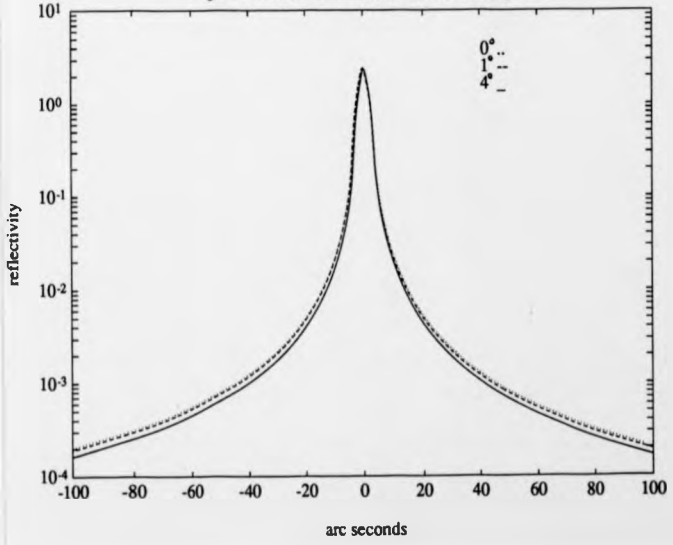

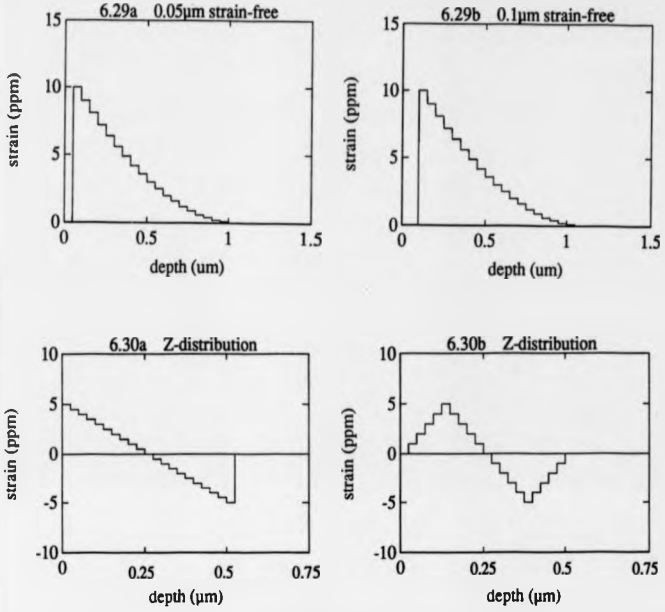

only the fringe nearest the rocking curve peak is observed.

Figure 6.31 shows the effect of cutting the wafer off (001) orientation. Commercial wafers intended for the growth of epitaxial layers are often cut about 4° off. The effect on the rocking curve depends on whether the angle of incidence is increased or decreased. Figure 6.31 shows simulations with increased angles of incidence. This causes a narrowing of the peak and a decrease in intensity in the tails. In the experiments, the angle of miscut could be measured from the shift in the angular position of rocking curve from one sample to the next. The kinematic mounting made this measurement quite accurate.

Other effects which change the peak shape include sample curvature and surface roughness (Chapter 2). These effects were eliminated by comparing rocking curves from

Figure 6.32. Simulations for rough and fully polished wafers.

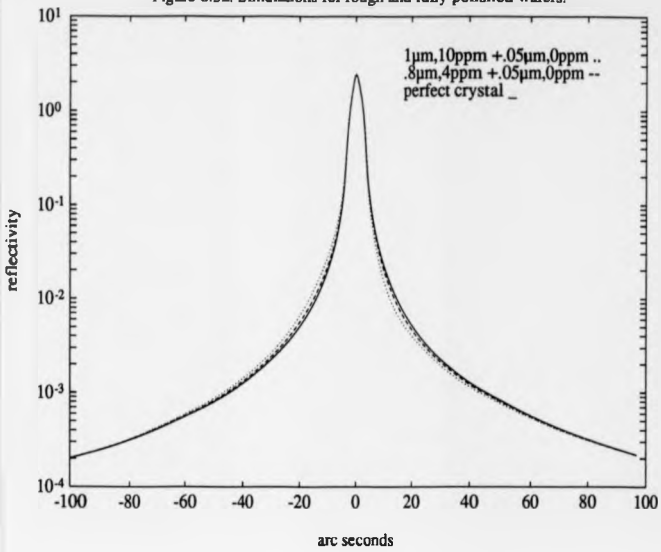

the same point on the sample before and after etching. However, the rocking curves of wafers from different manufacturers may be affected by differences in surface orientation and roughness, as well as differences in the strain-depth profiles.

By comparison of experimental with simulated rocking curves, as described above, strain-depth profiles for the rough and fully polished wafers were determined. A positive mismatch was assumed, due to the asymmetrically increased intensity on the low angle side of the rocking curve. For the rough-polished wafer, the best fit was given by a very low strain at the surface, a maximum strain of 10 ppm at 50 nm below the surface, decreasing gradually to zero at 1 μm below the surface. For the fully polished wafer, the depth profile was similar, but with a maximum strain of only 4 ppm, decreasing to zero at 0.8 μm below the surface. The strain-depth profiles are shown in figure 6.32a and b.

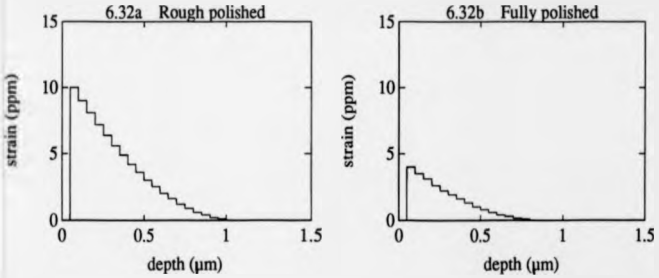

Table 6.1 gives the values of maximum strain, depth below the surface and total strained layer thickness for the rough and fully polished wafers. The resulting simulations are shown in figure 6.32, compared with a perfect crystal simulation.

Table 6.1 Values of strain and layer thickness for polished silicon wafers.

Wafer	max. strain (ppm)	depth of max. (μm)	layer thickness (μm)
rough polish	10	0.05	1.0
full polish 1	4	0.05	0.8
full polish 2	4	0.15	0.6

Values of strain and layer thickness for the commercially polished wafers were estimated by comparison of experimental with simulated rocking curves. The results are given in table 6.2. These values are accurate to within 0.5 ppm and 0.05 μm.

Table 6.2 Comparison of silicon wafers from different manufacturers.

Wafer	max. strain (ppm)	depth of max. (μm)	layer thickness (μm)
A	8	0.0	0.9
B1	6	0.05	0.8
B2	4	0.05	0.7
C	5	0.05	0.8
D	6	0.1	0.8
E*	4	0.1	0.6

*(3° off)

A better fit to the experimental data may be obtained by adding intensity to both tails of the theoretical strained-layer curve. This could be explained by diffuse scattering from atomic disorder or defects near the surface, which would increase the intensity at the rocking curve tails on both sides of the peak (Huang scattering). The diffuse scattering intensity distribution would be shifted towards the low-angle side for surface defects which expand the lattice (Chapter 3). Such defects include impurity and self-interstitials, and substitutional atoms with a larger radius than that of silicon atoms. Clusters of defects and dislocation loops could also be present.

It was therefore concluded that a combination of lattice dilation and atomic disorder or defects must be present near the surface in order to give an asymmetric peak shape with both tails higher in intensity than for a perfect crystal.

Similar conclusions have been made by several other workers. Kashiwagura et al (1983) measured diffuse scattering from polished (111) silicon wafers. They found rod-shaped scattering in reciprocal space which was shifted to the low-angle side of the Bragg peak. This disappeared after etching. Harada et al (1987) showed that the rod-shaped scattering was perpendicular to the crystal surface and not to the crystallographic planes. Kashihara et al (1987) explained the asymmetry by comparing the tails of the scattering intensity distribution with calculations using a model of the lattice plane at the surface, with a lattice expansion of 3% and only 30% of the Si atoms at the surface. However, the rocking curve simulations in this chapter have shown that the strained layer extends far below the surface, to depths up to a micron. Possible explanations of the cause of the strain are given in the discussion in Chapter 9.

Simulations for the epiwafers are shown in figures 6.33 and 6.34. The p-type epilayer is modelled by an 8 μm layer with a 25 ppm mismatch, and the n-type by a 1.5 μm layer with a 20 ppm mismatch. Both layers are positively mismatched (on the low angle side of the Bragg peak). Substitutional boron atoms give a larger lattice contraction than phosphorus atoms, hence the difference in mismatch between the p- and n-type epilayers. The layer thicknesses, particularly of the n-type epilayer are surprisingly less than those determined by fourier transform infra red measurements.

Figure 6.35 shows a simulation for the higher dose ion implanted silicon sample ($2\times10^{14}N^{+}/cm^{2}$, 110 keV). The strain-depth profile used in the simulation was similar to the Z-distribution in figure 6.30b, but with a mismatch of ±30 ppm and a total depth of 0.4 μm. The experimental rocking curve has a high diffuse scattering intensity, probably due to damage and amorphisation. The lattice expansion at the surface is produced by vacancies and the contraction by interstitials. The lattice strain is proportional to the

Figure 6.33. P-type epiwafer. 8 μm, 25 ppm. 2" curvature.

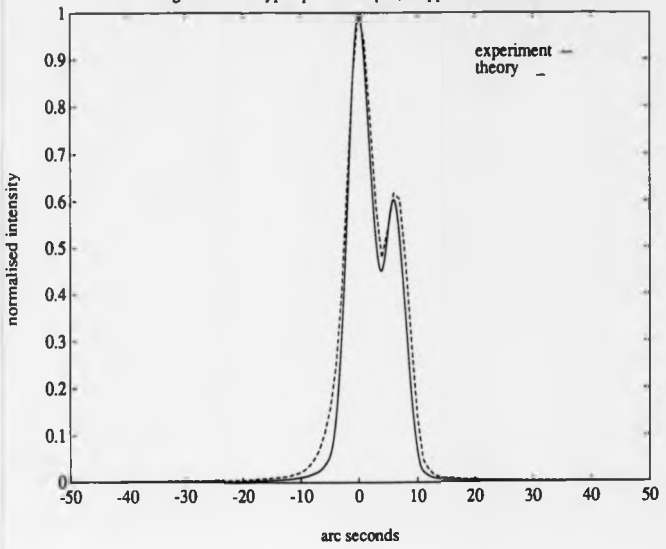

Figure 6.34 . N-type epiwafer. 1.5 μm, 20 ppm. 6" curvature.

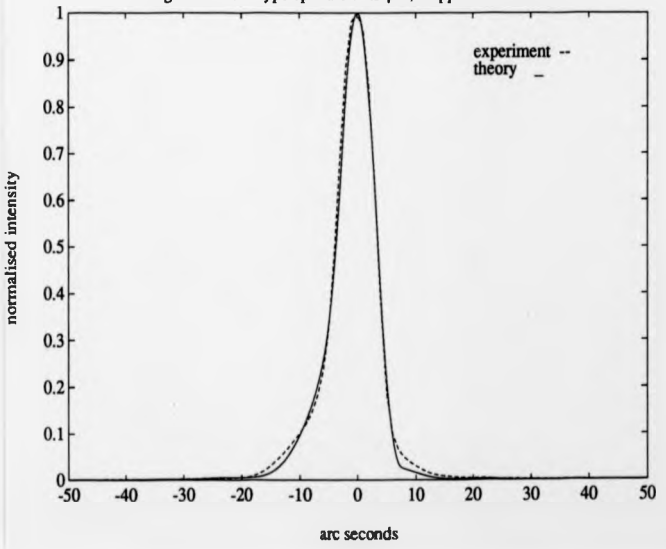

number of displaced atoms.

These simulations show that this technique can be used to characterise a range of material processes resulting in widely varying degrees of strain and damage.

Figure 6.35. Simulation of ion implanted silicon.

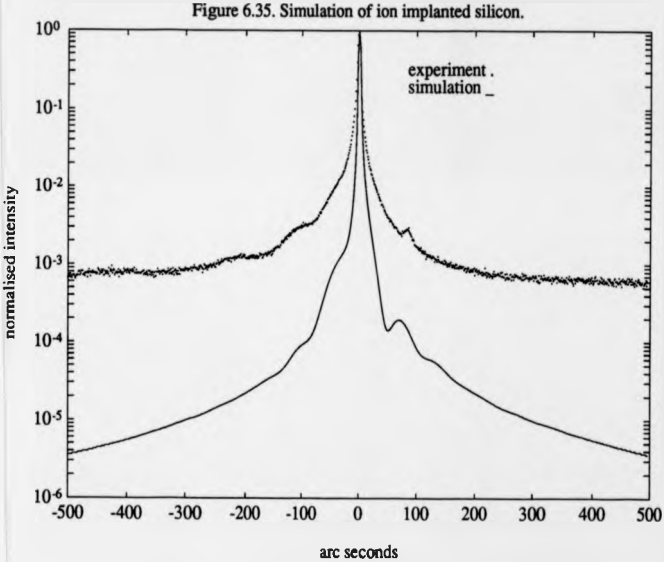

Chapter 7

7. Double-crystal x-ray topography.

7.1 Introduction.

Double-crystal topography was carried out using both a sealed-tube x-ray source and synchrotron radiation. The experimental conditions were carefully chosen to give both high strain senstivity and surface sensitivity.

Non-dispersive settings were used, with high order reflections (088 and 488) at short wavelengths of around 0.7 Å . These conditions give very narrow, steep-sided rocking curves with intrinsic widths less than 0.5 seconds of arc. Topographs taken on the steepest part of the rocking curve flank give high strain sensitivities, enabling detection of strains as low as 10^{-8} (Hart, 1968; Bonse and Hartmann, 1981).

Surface sensitivity was enhanced by using grazing incidence, which increases the path length of the x-rays inside the crystal. At low angles of incidence or exit, the extinction distance is reduced and absorption has a greater effect, causing a reduction in the penetration depth. As the angle of incidence approaches the critical angle for total external reflection, the diffracted beam becomes weaker, the specularly reflected beam becomes stronger and the penetration depth decreases rapidly. Below the critical angle, the diffracted beam is very weak and topography would be difficult unless synchrotron radiation and a strong reflection at the monochromator were used (Kitano et al, 1987).

It was deduced from the rocking curves in Chapter 6 that most of the polishing damage was in the top micron below the surface of polished silicon wafers. To enable comparison of polished and etched areas on the same topograph, rough polished and fully polished silicon wafers were partially masked using stopping-off lacquer, and etched in 1% HF(40%): 99% HNO_3(70%) for 5 or 10 minutes. The depth etched was measured using a Rank Taylor Hobson Form Talysurf and found to be 1.0μm for a 5 minute etch and 2.0μm for a 10 minute etch. Boundaries between etched and unetched areas were

approximately parallel to the (110) flats on each wafer.

7.2 Experiments using a conventional x-ray source.

The samples were 5 inch (001) silicon wafers which had been polished using the mechanical-chemical method described in Chapter 1.

The experiments were performed using the diffractometer and instrumentation described in Chapter 5. The 088 reflection was used with $MoK\alpha_1$ radiation (0.71 Å), giving an asymmetric reflection at the sample, with a 2.6° angle of incidence and a narrow intrinsic rocking-curve width of 0.3 arc seconds. This gave high strain sensitivity and also surface sensitivity. Because of the low angle of incidence, absorption had more effect than extinction, giving an absorption length of 31 μm and an extinction depth of 94 μm. The experimental set-up in the non-dispersive, (+,–) geometry, is shown in figure 7.1. An asymmetrically cut beam conditioner with a (113) surface and (088) Bragg planes was used to expand the beam by a factor of 3.5 in order to illuminate the whole of the sample. The beam was expanded again at the sample by a factor of 22. The azimuthal angles of incidence were 18.4° from [110], in the [210] direction at the beam conditioner and 45° from [110], in the [100] direction at the sample. A 3 kW long fine focus (12×0.4 mm^2) sealed-tube x-ray source was used at 58 kV, 36 mA, with a wide collimator, giving a beam size of about 100×65 mm^2 at the sample. The geometric resolution was calculated, from the source size and the specimen-film distance (20 mm), to be about 10 μm. The film used was Ilford G5 nuclear emulsion, 50μm and 100μm thick on glass plates. This gives a resolution of about a micron. Exposure times were up to several days, requiring automatic servo control to stay on the rocking curve flank.

Results.

Plates 7.1 to 7.4 show topographs of a rough-polished silicon wafer, etched in steps of 1μm as shown in figure 7.1. Rocking curves from this wafer are shown in figure 6.2 of Chapter 6. The etched depth is 1μm between the double lines and 2μm on either side of

Fig. 7.1. Double-crystal topography using an asymmetric first crystal.
088 reflection

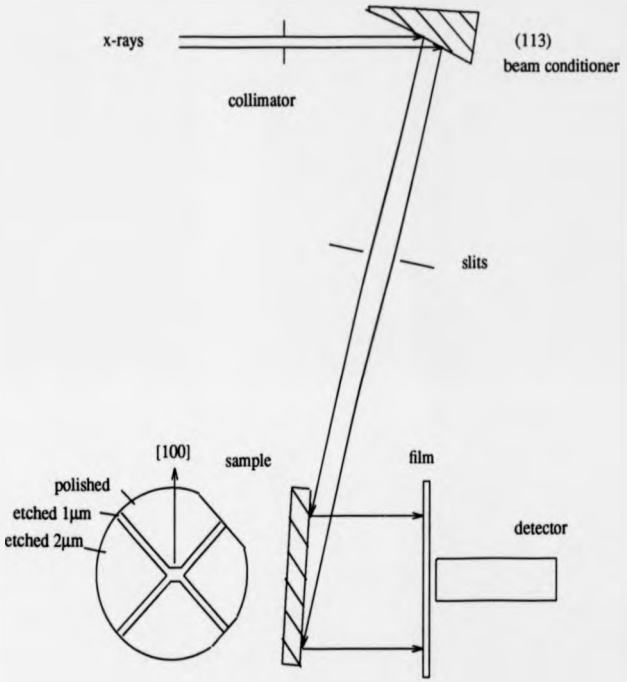

the wafer. The top and bottom areas of the wafer are as polished. Plates 7.1 and 7.2 are topographs taken on the low-angle and high-angle flanks of the rocking curve. Plates 7.3 and 7.4 are double exposures taken on opposite flanks of the rocking curve. The exact positions are shown in the figures. The rocking curves were taken with the photographic plate in position in front of the detector.

The topographs show light swirl towards the edges of the wafer, probably due to oxygen-related defects in the silicon (see Chapter 9). The blurred vertical streaks and "dents", visible on plates 7.3 and 7.4, are from the reference crystal. The diagonal lines are etched steps. Plates 7.5 to 7.9 are magnifications of plates 7.1 to 7.4. There appears to be little, if any, surface damage. A few defects, possibly due to handling damage, can be seen on the polished areas. These defects are not visible to the eye on the wafer surface. Areas with defects (shown by arrows) are further magnified in plates 7.9 and 7.10.

The rocking curves (without the plate in position) had full widths at half maximum (FWHM) of 4 arc seconds. This broadening was due to sample curvature. The strain sensitivity was calculated from equation 2.14 (Chapter 2), with lattice tilt, $\delta\theta = 0$. Contrasts of 5% and 1% give lattice strains of $\frac{\delta d}{d} = +4.0\times10^{-7}$ and $+8.0\times10^{-8}$ on the low-angle flank, with the opposite signs on the high-angle flank.

[100]

Double-crystal topographs. MoKα radiation. 880 reflection.
Rough polished silicon wafer. Etched 1 μm and 2μm.
Wafer positioned as in figure 7.1.

Plate 7.1. Low-angle flank.

62 hours exposure.

Plate 7.2. High-angle flank.

48 hours exposure.

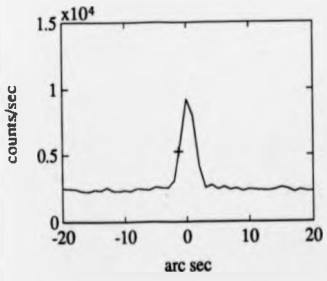

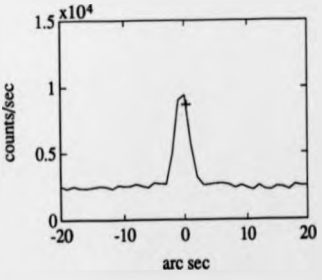

[100]

Double-crystal topographs. MoKα radiation. 880 reflection.
Rough polished silicon wafer. Etched 1 μm and 2μm.
Wafer rotated 180° from figure 7.1.

Plate 7.3. Double exposure.

48 hours on high-angle flank.

24 hours on low-angle flank.

Plate 7.4. Double exposure.

48 hours on high-angle flank.

16 hours on low-angle flank.

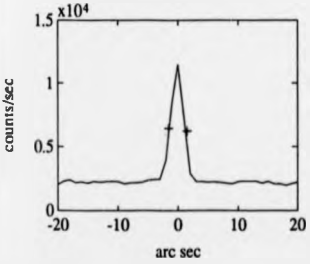

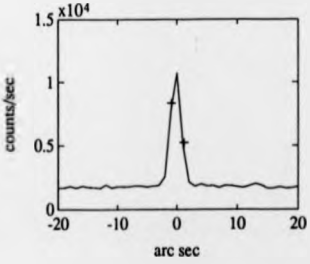

Double-crystal topographs. MoKα radiation. 880 reflection.
Rough polished silicon wafer. Etched 1 μm and 2μm.
Plates 7.1 and 7.2 magnified.

[100]

Plate 7.5. ⟷ 5 mm

Plate 7.6. ⟷ 5 mm

Double-crystal topographs. MoKα radiation. 880 reflection.
Rough polished silicon wafer. Etched 1 μm and 2μm.
Plates 7.3 and 7.4 magnified.

[100]

Plate 7.7. ⟵⟶ 5 mm

Plate 7.8. ⟵⟶ 5 mm

Double-crystal topographs. MoKα radiation. 880 reflection.
Rough polished silicon wafer. Etched 2μm top left and 1μm between lines.
Magnifications showing handling damage and defects.

Plate 7.9. ——— 5 mm

Plate 7.10. ——— 5 mm

7.3 Experiments using synchrotron radiation.

The samples and reference crystal were 3 inch diameter [001] grown float-zone silicon cut into 3 mm slices using a diamond saw and polished using the mechanical-chemical method described in Chapter 1. Because of the thickness of the slices, the polishing conditions were slightly different from those used for ordinary silicon wafers. The silicon was Bond oriented before cutting and a a notch cut in the [110] direction. Samples were cut either on (001) orientation or 1° or 4° off in the direction of the notch, so that the (001) planes tilted out of the surface at the notch. The orientation of each sample was checked by Laue photography, and the notch was found to be 12° off [110].

The reason for using thick samples, free from strain and curvature, was to facilitate experiments at extreme grazing incidence, down to the critical angle, where the penetration depth is very low. The samples were mounted kinematically to avoid unnecessary strains.

The experiments were performed at Daresbury Synchrotron Radiation Source (SRS) using the double-axis diffractometer described in Chapter 5. The experimental conditions were selected very carefully to give extreme surface sensitivity and high strain sensitivity. The wavelength was tuned to give grazing incidence of 0.5° to 1.5° at the sample, using the 488 reflection (0.68 to 0.69 Å) . This gives high surface sensitivities, with penetration depths of 6.0 μm at 0.5° and 0.1 μm at 0.1° incidence. The lower order 122 and 244 reflections are absent, so the 488 reflection has only weaker harmonics at shorter wavelengths. If there are harmonics, the images from the different orders of reflection are superimposed and more difficult to interpret. The 488 reflection has an intrinsic rocking-curve width of 0.5 arc seconds at 0.68 Å . This reflection was used at both the reference and sample crystals, giving high strain sensitivity, but rather low intensity. The setting was non-dispersive, with grazing exit at the reference crystal and grazing incidence at the sample, as shown in figure 7.2. The azimuthal angle of incidence was 18.4° from [110], in the [210] direction.

Fig. 7.2. Double crystal topography using grazing incidence.

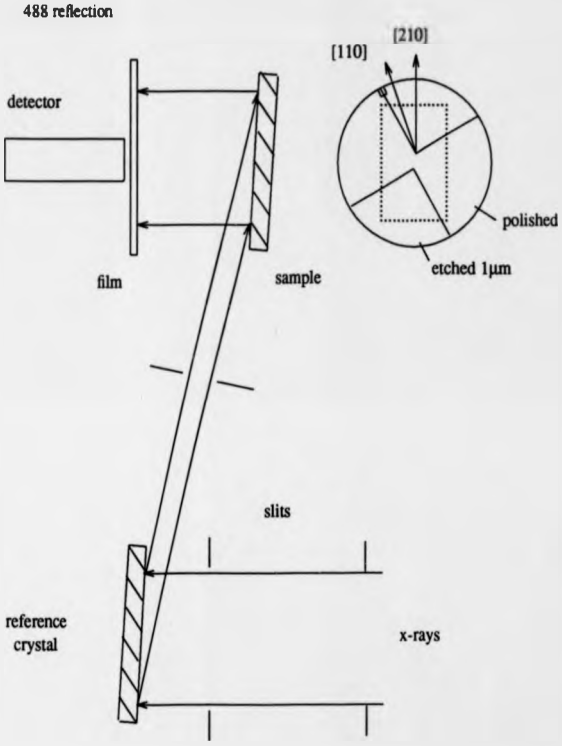

The critical angle for silicon at 0.7 Å wavelength is 0.1° . In order to determine the angle of incidence at the sample, the wavelength was tuned down until the rocking curve disappeared at 0° incidence. The wavelength of radiation could then be estimated. The angles of incidence and exit were accurately determined from the observed beam widths. Rocking curves taken at different wavelengths, with grazing incidence from 0.325° to

Figure 7.3. Rocking curves taken with incidence angles from 0.325° to 0° to determine the angle of incidence and wavelength.

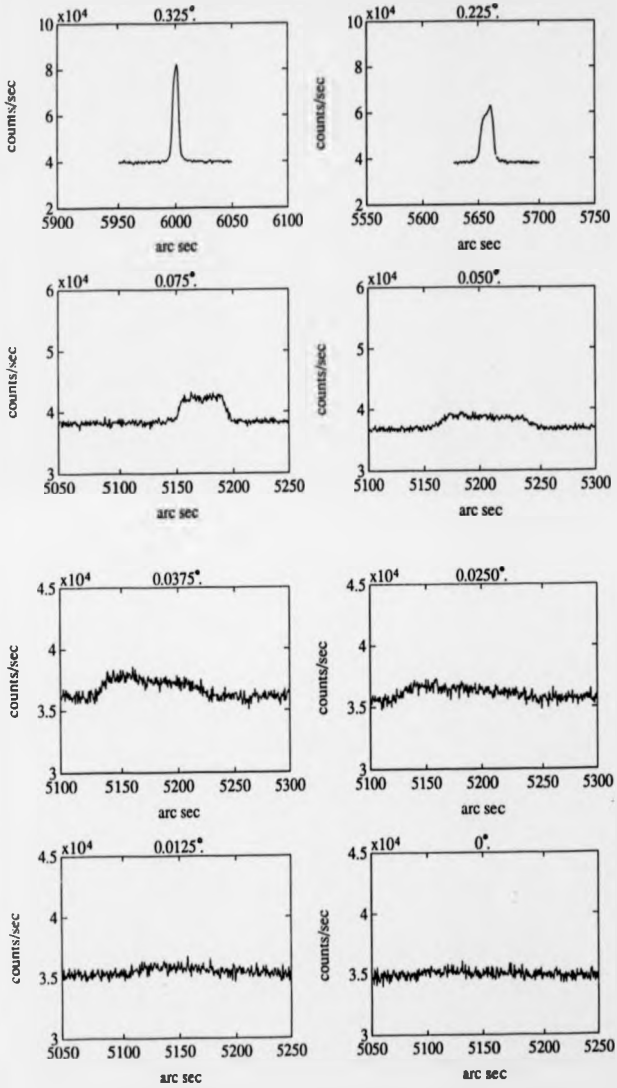

zero are shown in figure 7.3. The rocking curve becomes broader and weaker and finally disappears when the angle of incidence is zero. It was also noticed that the Bragg angle increased as the angle of incidence decreased towards the critical angle. A beam expansion at the sample was observed, due to the small surface misorientation of both the sample and reference crystals (estimated to be 0.5°, measured in the [210] direction). This misorientation caused an increase in exit angle at the reference crystal and a decrease in incidence angle at the sample, which had the desirable effects of increasing the surface sensitivity at the sample and broadening the image. This was the reason for cutting some of the samples 1° off (001), to allow a larger area of the sample to be imaged (the maximum vertical beam width was 22 mm, which could be increased by a factor of 3 with a 1° misorientation of the sample).

The film used was Agfa D4 and D7 and exposure times were as long as 8 hours !

Results.

Plate 7.11 is a white radiation topograph of a fully polished wafer, taken at grazing incidence (0.025°), for comparison with the double crystal topographs. The diagonal lines are 1μm etch steps. The upper area is etched 1μm.

Plates 7.12 and 7.13 are topographs of a fully polished silicon sample, taken at 0.8° and 0.5° incidence. The enhanced surface sensitivity in the 0.5° incidence topograph can clearly be seen. This is further magnified in plate 7.16. The rocking curve, taken with the film in position, is also shown. The topograph was taken on the low-angle flank. The upper and lower areas are etched 1μm and show small etch pits. The white vertical streaks are shadows of dust on the sample. The main region of interest (shown by arrows) is the dark contrast on the lower edge of the polished area. This appears to be residual strain relaxation at the edge of the polished area, where it has been etched 1μm and is no longer constrained by the surrounding crystal. The strain may have components of lattice dilation and tilt. The contrast is positive, indicating that the strain is positive (on the low-angle flank). The rest of the polished area, away from the edge,

appears slightly mottled.

The rocking-curve width (FWHM) was 4.4 arc seconds. Contrasts of 5% and 1% give lattice dilations of $\frac{\delta d}{d} = 7.1\times10^{-7}$ and 1.4×10^{-7}, or lattice tilts of 0.17 and 0.03 arc seconds. Figures 7.4 to 7.7 show densitometer traces along the etched edge. Figure 7.4 is furthest away from the edge and figure 7.7 is closest. Three distinct minima can be seen, corresponding to the three dark areas along the etched edge in plate 7.16. The sharp spikes are due to scratches on the film or dust on the sample. The contrasts of the three minima range from 20% to 40%. The strains measured are therefore between $\frac{\delta d}{d} = 2.8\times10^{-6}$ and 5.6×10^{-6}, or between $\delta\theta = 0.7$ and 1.4 arc seconds.

Plates 7.14 and 7.15 are topographs of a rough-polished silicon sample, taken at 1.5° and 0.5° incidence. The increase in surface sensitivity can again be seen. The polished area is on the right. On plate 7.15, the edge of the sample can be seen at the top right. The sample is leaning forward on to an aluminium mount at the top left, which may account for the narrow imaged area and broad rocking curve, due to sample curvature. Plate 7.15 is further magnified in plate 7.17. The rocking curve is also shown. The topograph was taken on the high-angle flank. The surface appears mottled and there is a small linear defect at the top of the polished area, which disappears at the etch boundary.

The rocking curve width (FWHM) for this sample is 9 arc seconds. The large broadening is due to the sample curvature. 5% and 1% contrasts give strains of $\frac{\delta d}{d} = 1.3\times10^{-6}$ and 2.6×10^{-7} or $\delta\theta = 0.3$ and 0.1 arc seconds.

Figure 7.4 Densitometer trace along etched edge in plate 7.16

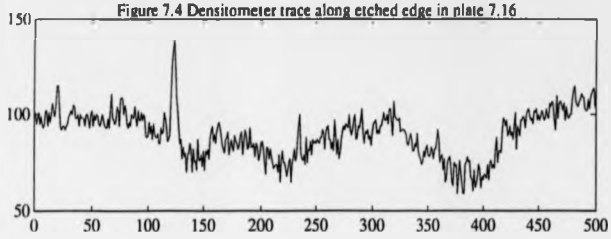

Figure 7.5 Densitometer trace along etched edge in plate 7.16

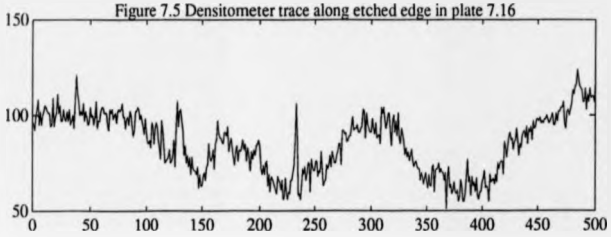

Figure 7.6 Densitometer trace along etched edge in plate 7.16

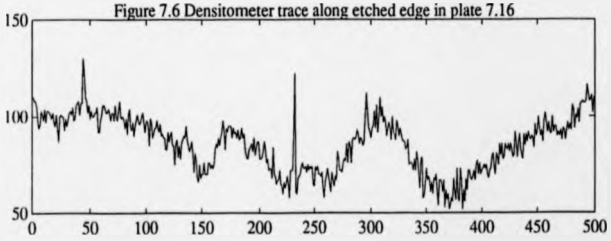

Figure 7.7 Densitometer trace along etched edge in plate 7.16

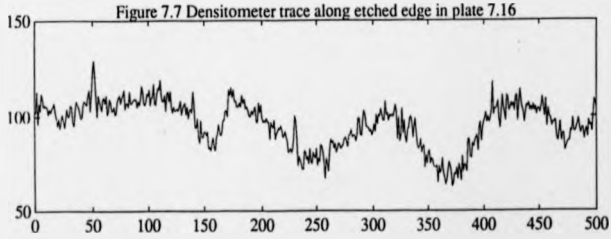

Plate 7.11. White radiation topograph. 220 reflection.
Polished silicon wafer. Top etched 1 μm.
0.025° grazing incidence. 75 minute exposure.

[100]

Double-crystal topographs. Synchrotron radiation. 0.69 Å. 488 reflection.
Float-zone silicon. Fully polished. Etched 1 μm top and bottom.

[210]

Plate 7.12. 0.8° incidence.

2 hour exposure.

Plate 7.13. 0.5° incidence.

8 hour exposure.

Double-crystal topographs. Synchrotron radiation. 0.69 Å. 488 reflection.
Float-zone silicon. 1° misorientation.
Rough polished. Etched 1 μm top and bottom.

[210]

Plate 7.14. 1.5° incidence.

4 hour exposure.

Plate 7.15. 0.5° incidence.

8 hour exposure.

Plate 7.16. Magnification of 7.13. 5 mm

[210]

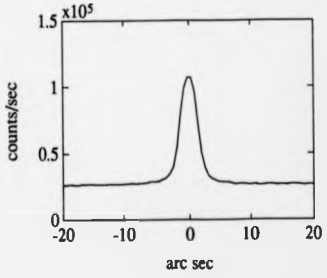

Plate 7.17. Magnification of 7.15.

5 mm

[210]

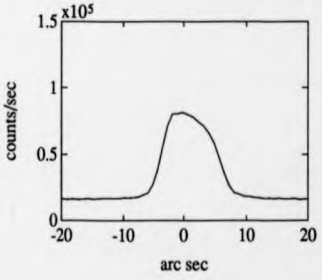

Chapter 8

8. Energy dispersive reflectometry.

Reflectometry is a powerful technique which can be used to measure surface roughness, layer thickness and density, for both amorphous and crystalline layers (Chapter 4). It therefore complements diffraction techniques, which can only be used to characterise crystalline materials.

Angle dispersive reflectometry, where the sample is rotated through a range of angles, requires extremely long counting times because of the rapid decrease in the reflected intensity above the critical angle. If a method could be found to reduce the data collection time, reflectometry could be used more routinely, for example, for quality control and assessment. Energy dispersive reflectometry is a solution to this problem. The complete reflectivity curve can be obtained in several minutes, by simultaneously measuring a range of energies reflected from the sample at a fixed angle of incidence. A solid state detector is used to give a large dynamic range.

8.1 Experiments.

The high-energy x-ray source at Manchester University (Holý, Cummings and Hart, 1988) was used for a series of reflectivity experiments on polished silicon wafers. The samples were silicon wafers which had been polished using different polishing processes, wafers which had been etched and wafers from several different manufacturers. Ion implanted silicon and aluminium were also investigated.

The experimental set-up is shown in figure 8.1. The x-ray source was a standard sealed-off microfocus tube with a tungsten target and 4×0.4 mm^2 source size. The x-ray tube was shielded and had a 2 mm diameter tungsten collimator. The beam was defined by molybdenum slits 250 mm long, with a spacing of 4 μm. These were used to obtain a low horizontal beam divergence of 3.3 arc sec (16 μrad) and, hence, high resolution. The sample was mounted vertically on one axis of a diffractometer, using vacuum grease on a

manual translation stage which enabled horizontal translation of the sample in or out of the beam. A second pair of molybdenum slits, spaced 0.1 mm apart, was mounted on the diffractometer between the sample and the Ge(Li) solid state detector. Two silicon wafers were positioned in the beam to act as a filter in the low-energy region below the critical angle, thus enhancing the high-energy region of interest far from the critical angle. A Canberra spectroscopy amplifier and multi-channel analyser were used to record the energy spectra.

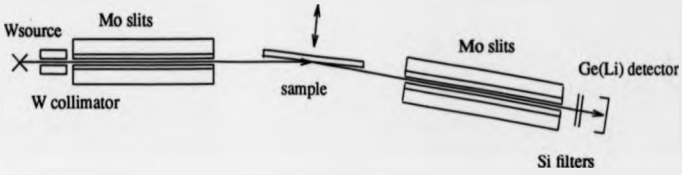

Fig. 8.1 Energy dispersive reflectometry.

The diffractometer and slits were carefully aligned with the beam to give maximum intensity at the zero position with no sample. The sample was then translated into the beam until the intensity was reduced by half. To set the sample parallel to the beam, it was rotated and set half-way between the two positions at which the beam was cut off. The sample was then moved to an angle of between 0.1° and 0.15° and again rotated and translated to obtain the maximum intensity possible. The sample position was checked using a laser reflected from the sample to the far wall 6.5 m away. After the initial setting up, samples could be changed relatively easily. The x-ray generator was set at 150 kV, 3.5 mA and the reflected beam recorded over a period of thirty minutes to several hours. Reflectivity data was also collected at 55 kV, 4.2 mA. The direct beam was recorded at lower currents of 0.3 mA at 150 kV and 1.5 mA at 55 kV, to prevent detector saturation.

An angle of incidence of $\theta = 0.1°$ was chosen to give a spectrum with the critical angle at the low-energy end of the range, with the region of interest, far from the critical angle, at the high-energy end. The width of the beam on the sample at 0.1° was estimated to be 2.3 mm. Several different angles were tried, ranging from $\theta = 0.1°$ to 0.15°. Angles of incidence greater than 0.2° required very long counting times because of the low reflected intensity. Angles less than 0.1° would result in a possible reduction in intensity from small samples, due to the increase in the projected beam width. It would also be more difficult to separate the direct and reflected beams.

8.2 Results.

All the results shown were measured at 150 kV. The 55 kV data showed similar results but covered a smaller range (50 keV). Figure 8.2 shows the direct beam spectra with and without the silicon filter. The tungsten K and L lines can be seen, and also the Mo K absorption edge. These lines were used to calibrate the energy spectra. The range was 80 keV, with a spectral resolution of 0.02 keV. All the reflected beam spectra were divided by the direct spectrum. However, this did not completely remove the characteristic lines. The reason for this is not understood, but it is likely to be an effect of the different set-ups used for measuring the direct and reflected beams. One explanaton is multiple scattering in the Mo slits, which would enhance the absorption of x-rays.

Figure 8.3 shows reflectivity curves from a polished silicon wafer at several different angles of incidence. The data has been divided by the direct spectrum, normalised and smoothed. The critical energy for total external reflection decreases as the angle of incidence increases (Chapter 4). The critical energies in figure 8.3 are close to the Mo K absorption edge (20 keV). The actual angles of incidence were estimated from the critical energies to be 0.08°, 0.105° and 0.13°.

Reflectivity curves from silicon wafers which had been polished using several different processes are shown in figures 8.4 and 8.5. These curves were obtained after 30

Figure 8.2. Direct beam spectra. 150 kV, 0.3 mA.

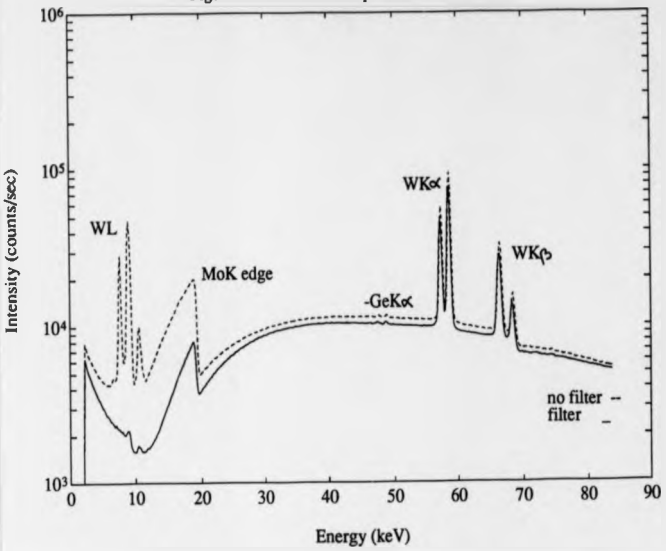

Figure 8.3. Energy dispersive reflectivity for silicon at various angles of incidence.

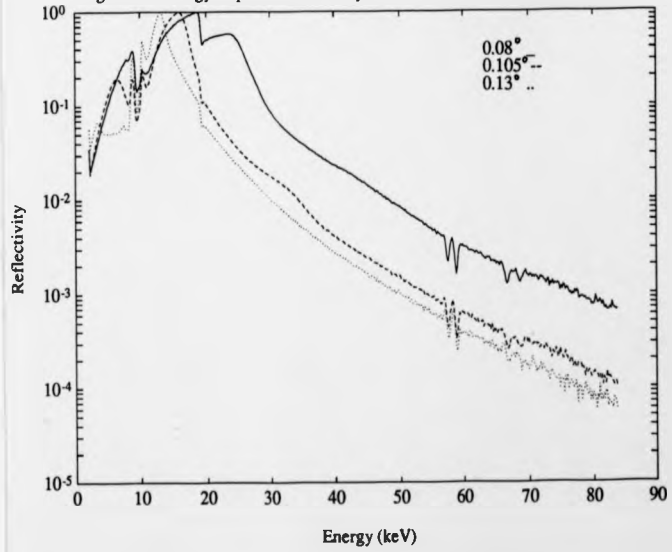

Figure 8.4. Reflectivity. Silicon wafers polished by different processes.

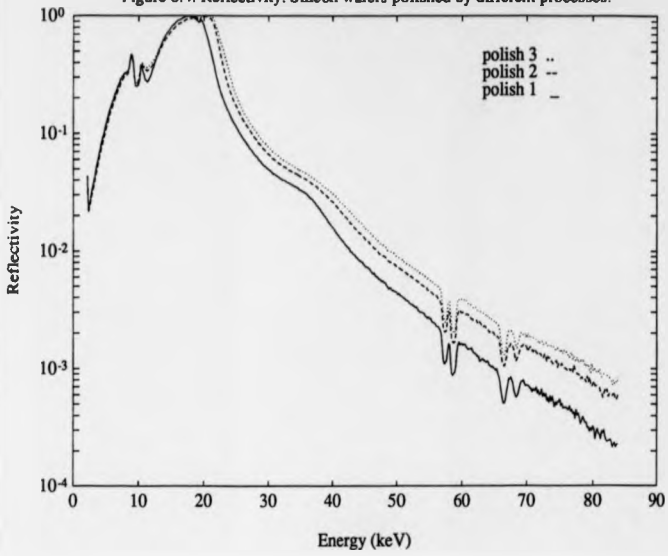

Figure 8.5. Reflectivity. Silicon wafers polished by different processes.

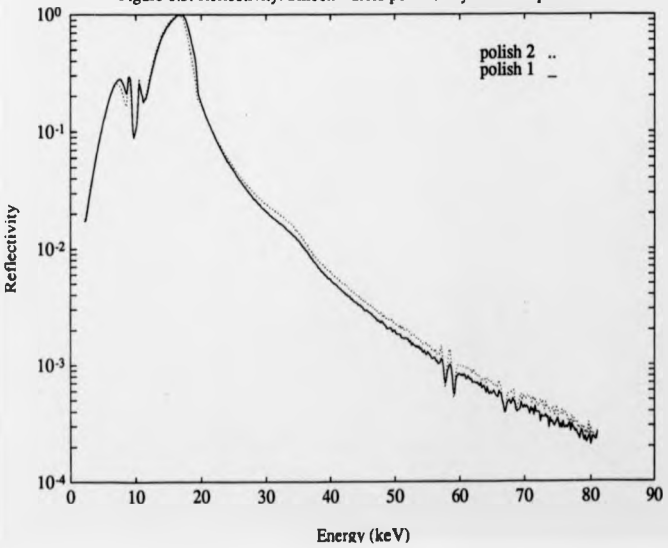

minutes of data collection time. However, most of the information could be determined from the reflectivity curves after the first five minutes of counting time.

The different gradients of the curves are due to surface roughness. As the surface roughness increases, the reflectivity decreases and the curve becomes steeper. The progressive improvement in surface smoothness of wafers produced by polish 2 and polish 3, compared to polish 1, can clearly be seen in figures 8.4 and 8.5. Measurement of oxidation induced stacking faults by Dr. G.R. Fisher (1988) showed that, compared to polish 1, polish 2 greatly reduced the stacking fault density, but polish 3 resulted in only a small reduction.

The angles of incidence vary slightly, probably due to differences in wafer curvature and mounting. A shallow fringe can be seen between 30 and 40 keV. This could be an interference fringe from a thin layer on the surface.

Figure 8.6 shows reflectivity curves from polished and etched wafers. The etching appears to produce a greater surface roughness, but there is a smaller difference than that between wafers polished by different techniques. The interference fringe can again be seen between 30 and 40 keV.

Reflectivity curves from silicon wafers from different manufacturers are shown in figure 8.7. The variations in the gradient can be determined, even though the angles of incidence are slightly different. The wafer from vendor D (also see Chapter 6) has the least rough surface, followed by vendor G and vendor F in order of increasing surface roughness.

Figures 8.8 to 8.11 show reflectivity data from silicon and aluminium samples supplied by Prof. B.K. Tanner and ion implanted with nitrogen by T.A. Woods of Whickham Ion Beam Systems. The silicon samples were implanted at 110 keV with doses of 2×10^{13} and 2×10^{14} N^+/cm^2. Data was collected for 4½ hours for the lower dose, 6¼ hours for the higher dose. The aluminium sample was implanted at 90 keV with a dose of 3×10^{17} N^+/cm^2 on one side and unimplanted on the other side. The data

Figure 8.6. Reflectivity. Polished and etched silicon wafers.

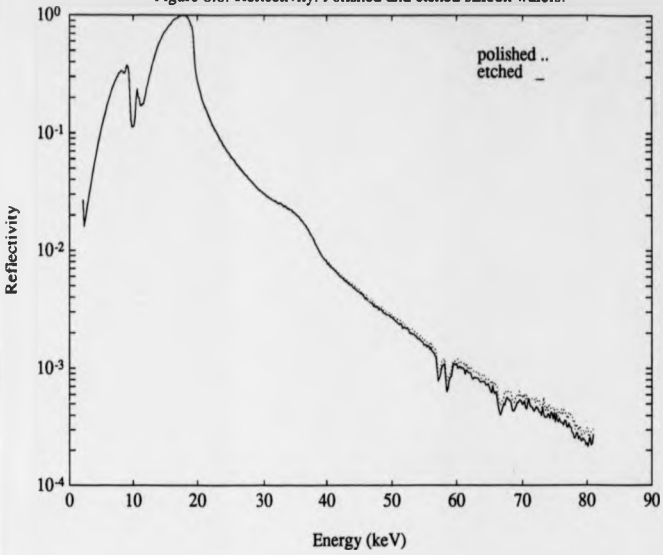

Figure 8.7. Reflectivity. Silicon wafers from different manufacturers.

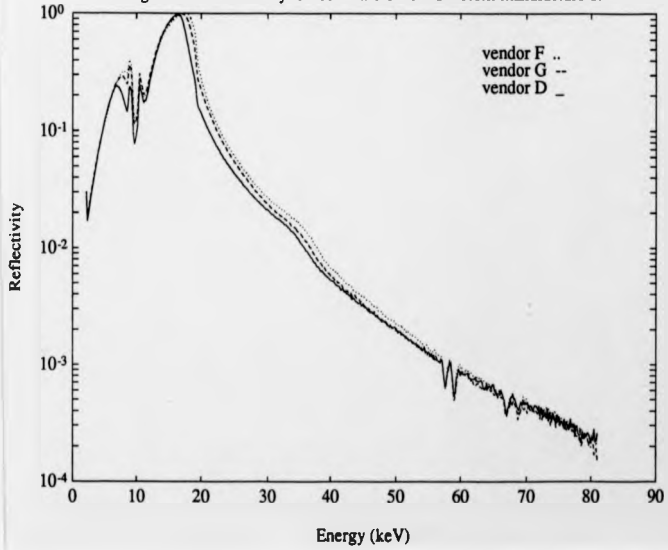

Figure 8.8. Reflectivity. Ion implanted silicon. Raw data.

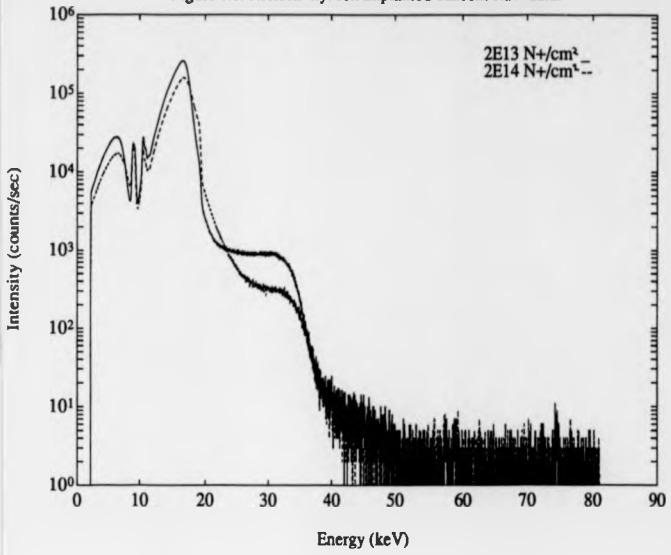

Figure 8.9. Reflectivity. Ion implanted silicon.

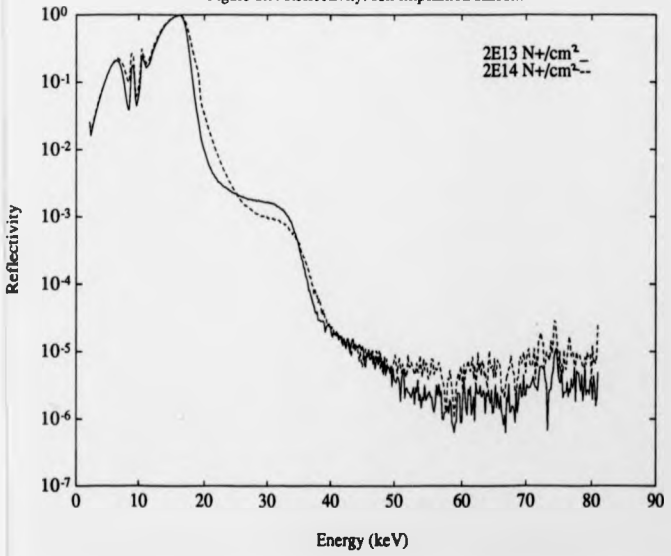

Figure 8.10. Reflectivity. Ion implanted aluminium. Raw data.

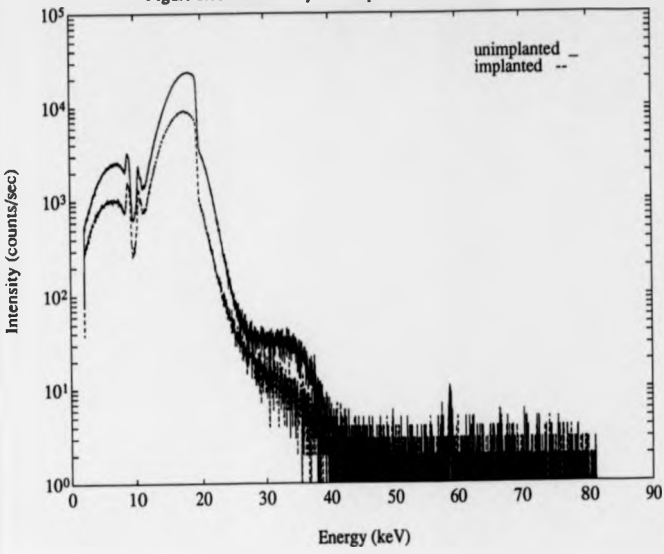

Figure 8.11. Reflectivity. Ion implanted aluminium.

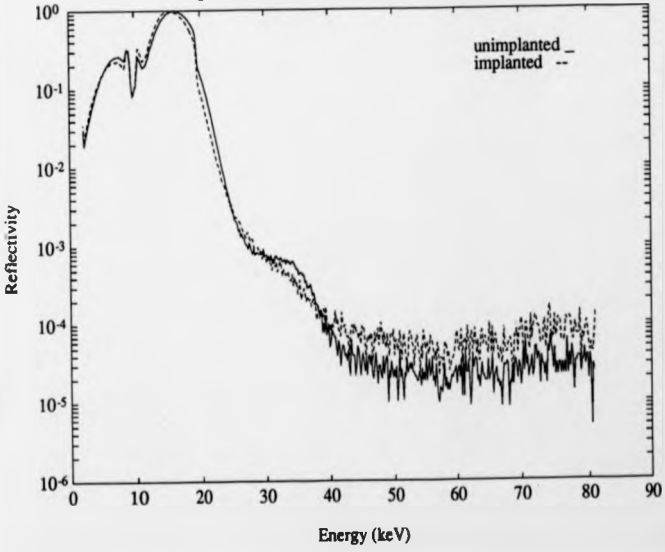

collection time was 2 hours for either side.

8.3 Simulations.

Simulations could not be compared directly with experimental data because of the characteristic lines which could not be completely removed from the data, as described above. The Mo K absorption edge, in particular, caused problems since it was near the critical energy for silicon at 0.09° incidence (20 keV) and therefore affected all the curves taken at 0.1° incidence.

Figure 8.12 shows energy dispersive reflectivity simulations for silicon at a range of angles of incidence. The critical energies correspond roughly to those in figure 8.3. Reflectivity curves for silicon with varying surface roughness are shown in figure 8.13. It can therefore be deduced that the different polishing processes used in figures 8.4 and 8.5 produce surface roughnesses varying by 3 to 8 Å rms . Silicon wafers from different manufactureres (figure 8.7) also vary in surface roughness by around 5 Å rms. The etched wafer in figure 8.6 has about 3 Å rms roughness more than the polished wafer. This shows that very small surface roughnesses can be measured using this technique.

Native oxides on silicon normally grow to thicknesses in the range 5 to 25 Å. Figure 8.14 is a comparison of silicon wafers with 0 Å, 25 Å and 50 Å surface oxide layers. The oxide density is 5% less than that of silicon and the interference fringes are therefore of low amplitude. The differences between the reflectivity curves from wafers from different manufacturers in figure 8.7 could be due to variations in both the surface oxide thickness and roughness. The interference fringe seen between 30 and 40 keV in all the silicon wafer curves cannot be explained by the presence of an oxide layer, and is probably due to a thin, dense layer of contamination, such as a water or oil film (from vacuum pumps in the vicinity of the x-ray lab).

The ion implanted silicon in figures 8.8 and 8.9 appears to have a surface layer, several hundred Ångstroms thick, of up to 50% lower density than silicon. The two

Figure. 8.12. Simulations for silicon for a range of incidence angles.

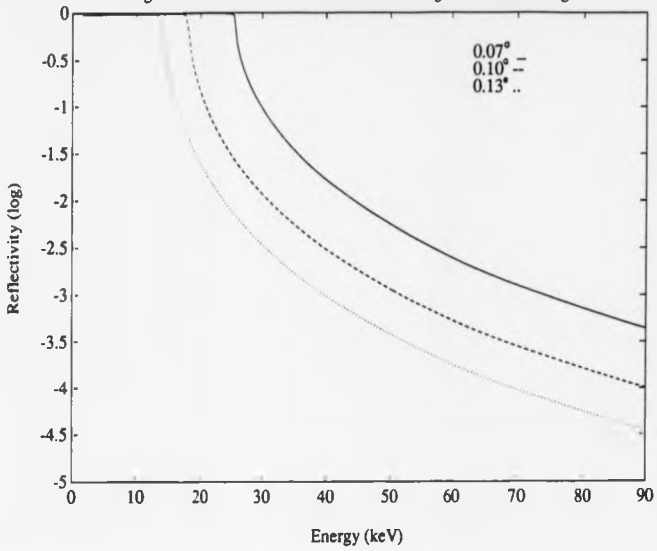

Figure 8.13. Simulations for silicon with varying surface roughness. 0.1° incidence.

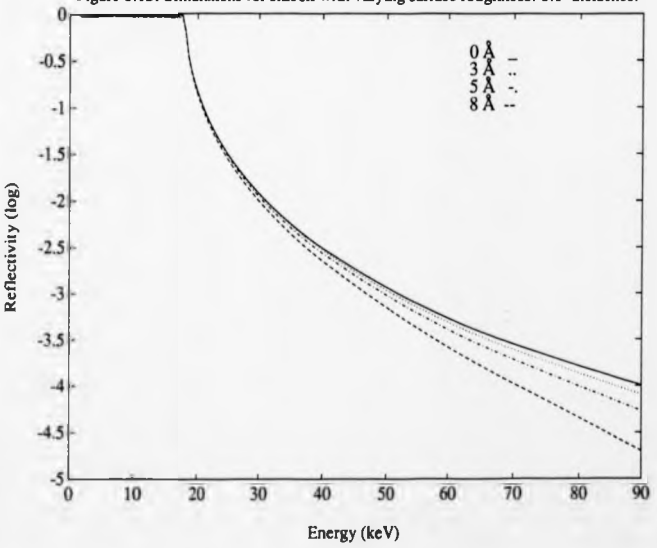

Figure. 8.14. Simulations for silicon with varying thicknesses of SiO_2. 0.1° incidence.

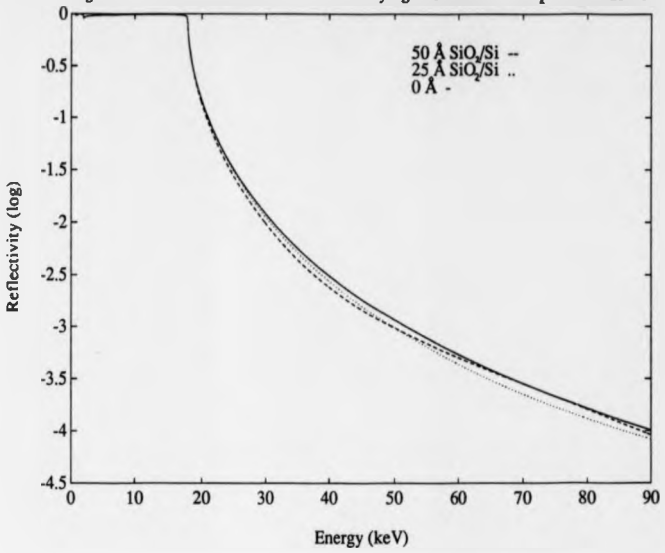

Figure. 8.15. Simulations for aluminium with varying thicknesses of Al_2O_3. 0.1° incidence.

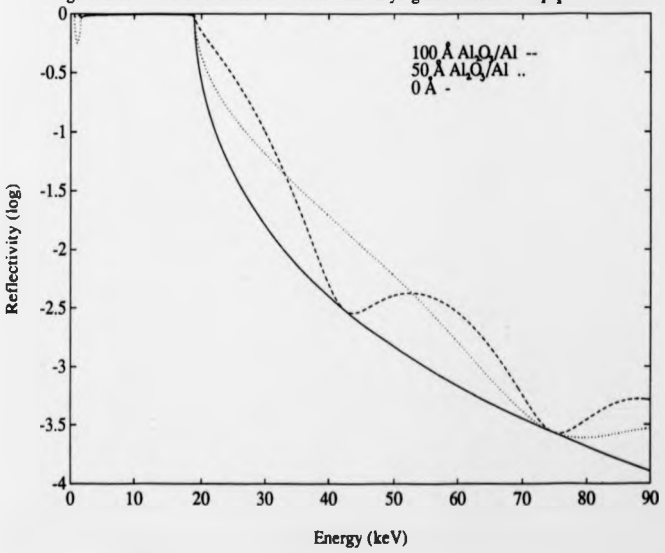

different doses give displaced interference fringes of slightly different amplitudes. The lower dose fringes have the larger amplitude and are nearer the critical energy, indicating a slightly thicker surface layer than that produced by the higher dose. The decrease in fringe amplitude at the higher dose could be explained by an increase in interface roughness. The surface and interface roughnesses are high (estimated to be up to 20 Å rms), producing reflectivities lower than 10^{-6} above 50 keV.

Aluminium oxide has a density of almost 50% greater than aluminium. A comparison of 0 Å, 50 Å and 100 Å layers of oxide on aluminium is shown in figure 8.15. The fringes have a much greater amplitude than those from oxide layers on silicon. A difference can be seen between the unimplanted and implanted aluminium in figures 8.10 and 8.11. The fringes, possibly due to a surface oxide layer, have a much smaller amplitude after implantation. This could be due to an increase in interface roughness. The surface roughness is high (more than 40 Å rms).

Despite a few experimental difficulties, energy dispersive reflectometry has been shown to be a powerful technique, enabling measurement of surface layer thickness and roughness down to Ångstrom resoluton in a relatively short time.

Chapter 9

9. Discussion and Conclusions.

9.1 Discussion.

Mechano-chemically polished silicon.

Possible explanations for the lattice expansion and diffuse scattering measured from the surface of polished silicon wafers include the presence of point defects or extended defects, or disorder of atoms at the surface caused by amorphous smearing in the polishing process. If line dislocations were present, the crystal would be slightly mosaic and micro tilts between mosaic blocks would result in broadening (that is, an increase in the full width at half maximum) of the rocking curve. This is observed in as-sawn and lapped wafers but not in polished wafers. It can therefore be deduced that any defects present are likely to be point defects or clusters of point defects. Amorphous smearing of atoms at the surface would produce diffuse scattering, but does not explain the lattice expansion at the surface. The difference between the rocking curves from the as-sawn and lapped wafers can be explained as follows. If material is removed by cracking and chipping under high loads, such as in diamond sawing, the damage depth is high (tens of microns) but the residual strain is low (Puttick and Shahid, 1977). However, if material is removed by smaller abrasive particles under lower loads, such as in lapping, ductile fracture occurs by the generation of dislocations and movement in slip planes and directions (Stickler and Booker, 1963). The damage depth is low (several microns) but the residual strain, due to the high concentration of dislocations, is high. The dislocations cause broadening of the rocking curve but are too closely spaced (~0.1μm) to be resolved in an x-ray topograph.

In the mechano-chemical polishing process, the silicon wafer surface is repeatedly etched and re-oxidised. Oxidation occurs by diffusion of oxygen to the oxide-silicon interface, where it reacts with the silicon to form SiO_2. The extra oxygen at the interface

can either occupy a silicon vacancy, or displace a silicon atom, which forms a silicon self-interstitial (Ravi, 1981). For p-type silicon, the self-interstitials occupy tetrahedral positions in the lattice.

Continued oxidation results in diffusion of silicon interstitials away from the interface. The rate of diffusion depends on whether vacancies or self-interstitials dominate the diffusion process. At high temperatures (1100-1300°C), there exists a dynamical equilibrium between vacancies and self-interstitials. At lower temperatures, under non-equilibrium conditions, self-interstitials move independently of vacancies. The diffusivity is then greatly enhanced. Tan and Gösele (1985) give a diffusion coefficient, $D \approx 10^{-5} \exp(-0.4(eV)/kT)$ cm^2/s for diffusion of silicon self-interstitials. This is accurate only to one or more orders of magnitude and is probably rather high. Calculations of the depth of silicon interstitials from the diffusion length, $x = \sqrt{Dt}$ after a time, t of 60 seconds gives 300 nm at 80°C and 100 nm at 25°C. Injection of self-interstitials by repeated oxidation of silicon is therefore a plausible explanation for the lattice expansion and diffuse scattering measured by rocking curve analysis in Chapter 6. The measured strain-depth profile shows a maximum lattice expansion at about 50 nm, decreasing to zero at up to 1 μm from the surface. The theoretical diffuson profile of concentration against depth is similar to the measured strain-depth profile.

The oxidation and diffusion process during polishing is further complicated by the continuous removal of the surface layer. Rough polishing produces greater strains because of the higher material removal rates and, hence greater number of etching-oxidation cycles, producing higher concentrations of self-interstitials. After polishing, the rate of surface oxidation rapidly decreases when the oxide layer reaches a thickness of about 1.5 nm. The interstitials at the surface may then be annihilated by diffusion into the surface oxide at room temperature. This would result in a lower lattice strain at the surface, as determined from the rocking curves in Chapter 6. Substitutional oxygen may also be present at the oxide-silicon interface, causing a slight lattice contraction. This

would cancel the expansion caused by the silicon interstitials to produce a lower overall strain at the surface. Etching removes the strained surface layer, though subsequent oxidation at room temperature could result in the formation of a low concentration of silicon interstitials at the interface.

If the concentration of point defects exceeds the equilibrium value at a particular temperature, the defects condense into clusters, dislocation loops or stacking faults. Calculation of the extra volume due to a 5ppm lattice expansion, and hence the total extra volume of silicon atoms gives a silicon interstitial concentration of be 2.2×10^{18} atoms/cm^3. Microdefects are most likely to form where there is residual strain or damage at the crystal surface, or at impurities in the silicon. Microdefects with strain fields smaller than 1 μm cannot be resolved by topography, though inhomogeneous distributions of defects, such as swirl, can be imaged. Surface strains can be imaged if part of the surface is etched away, allowing the strain to relax at the edge (Chapter 7). Lattice tilts and dilations both give contrast.

Impurities in silicon include carbon and oxygen, which are dissolved in the melt during Czochralski growth from the silica crucible. The oxygen content of Czochralski silicon is 10^{17}–10^{18} atoms/cm^3, while float-zone silicon contains 10^{15}–10^{16} atoms/cm^3. The oxygen atoms are interstitial, causing a local lattice expansion of about 3ppm for Czochralski silicon. The carbon atoms (~10^{17}/cm^3) are substitutional, producing lattice contractions of −0.3 to −1.0 ppm. Swirl is caused during crystal growth, by thermal convection currents in the liquid silicon. The type of microdefect formed depends on the growth rate and the temperature gradient near the crystal-liquid interface. There are two main types of swirl defects observed in silicon. A-defects are small (~1μm) dislocation loops formed from excess silicon interstitials and oxygen. B-defects are thought to be even smaller clusters of silicon atoms, nucleated by an impurity such as carbon. In the topographs in Chapter 7, swirl could be seen near the edges of the commercial silicon wafers, but not in the float-zone silicon. The rocking curve comparison in Chapter 6

showed diffuse scattering from defects in silicon wafers causing local lattice expansions, thought to be oxygen-related.

Silicon self-interstitials have little effect on the density of the silicon, below concentrations of 10^{18} atoms/cm^3. This is due to the extra volume occupied by the interstitials, which counteracts the effect of the extra mass. Surface layers will give interference fringes in reflectivity curves only if the density differs from that of the substrate by more than a few percent. However, surface and interface roughnesses of only a few Ångstroms can be measured from the difference in the gradient of the curves. Polished silicon surfaces were found to vary by about 5 Å root-mean-square roughness.

Silicon dioxide is about 5% less dense than silicon and gives fringes which, though detectable, are not of very large amplitude. Even so, the oxide layer density and thickness can be determined by comparison with theoretical reflectivity curves.

9.2 Applications.

The techniques developed can be applied either in the semiconductor and electronics industry, or used in research. Applications in industry include incoming wafer inspection, quality control and process development. Rocking-curve analysis may be used in the monitoring and evaluation of wafer manufacturing processes. It enables qualitative and quantitative assessment of wafer surfaces and is therefore an extremely useful tool. This also applies to energy dispersive reflectometry, although the methodology of this technique is not as well established. Reflectometry is extremely sensitive to very small differences in surface properties, and can therefore give detailed information on the quality of polished wafer surfaces.

In x-ray topography, the achievement of both high strain sensitivity and surface sensitivity is difficult and is therefore useful only in research, if it is necessary to map very low surface strains.

All the techniques developed are sensitive enough to be used in research, for the

determination of surface strains produced by new processes and surface properties of new materials. The methods can be applied to a wide range of materials, including GaAs, InP, epitaxial layers and ion implanted samples.

9.3 Suggestions for further work.

Triple-crystal diffractometry can be used to separate diffuse scattering from dynamical diffraction and also to separate the effects of lattice dilation, tilt and surface unevenness. This is therefore the next step in the detailed characterisation of surface strains. Diffuse scattering measurements can be made by setting the sample at various angles away from the Bragg position and scanning the analyser. In order to measure the symmetry of the diffuse scattering, it is necessary to map the intensity distribution in reciprocal space. The type and orientation of defects can then be determined. If the defects are randomly orientated, three different reflections are required. However, triple-crystal diffractometry is difficult to set up and takes a long time. Double-crystal diffractometry is fast and versatile and, with the use of multiple reflection beam conditioners, can be used to measure low strains and thin layers. Diffuse scattering theory could be incorporated into rocking-curve simulation programs to enable determination of defect size and concentration, as well as strain and layer thickness.

Triple-crystal topography can be used to separate lattice tilts and dilations. This is especially useful if the sample is curved. Anomalous transmission and section topography can be used to characterise defects larger than about a micron. Smaller defects require transmission electron microscopy for imaging.

Energy dispersive reflectometry is a powerful technique, and therefore worth developing further. It gives information on very thin surface layers and the data collection times are not long. Both standard and high energy x-ray sources can be used. Angle dispersive reflectometry is also very powerful, although it takes a long time if the information required is far from the critical angle, or if the surface layers are thin. Extremely high angular resolution may be obtained if multiple-reflection beam

conditioners are used.

A range of non-x-ray techniques could be used to supplement the results obtained here. Useful techniques include TEM and SEM, light scattering and ellipsometry, infra-red spectroscopy or imaging of impurity clusters and ion channelling to determine strain and damage depth and lattice location of defects.

9.4 Conclusions.

Double-axis x-ray diffractometry may be used to detect very small strains (mismatches of a few parts per million) down to a resolution of 50 nm below the surface.

The mechanical-chemical polishing process used to produce high-quality silicon wafers leaves residual strain at the surface, which may be removed by etching. Comparison with theoretical simulations enables strain-depth profiles to be determined. A probable strain profile is a very low lattice mismatch just at the surface, rising to between 4 and 8 ppm at about 50 nm depth and falling gradually to zero at 1 μm below the surface. There is also disorder or defects, near the surface, which give extra diffuse scattering in the rocking-curve tails. The defects are thought to be silicon self-interstitials injected into the silicon during oxidation in the polishing process.

This technique may be used to monitor the silicon wafer polishing process, or to determine paths for improvement of the wafer surface quality. It is sensitive enough to detect differences between silicon wafers from different vendors, even with nominally the same polishing process, and enables a qualitative and quantitative assessment of surface strains.

Double-crystal topography can be used to map strains of the order 10^{-7}. Light swirl and handling damage can be detected in high quality mechano-chemically polished silicon wafers using high order reflections and short wavelengths with a conventional x-ray source. If synchrotron radiation is used, the grazing incidence can be tuned to very low angles. The surface sensitivity increases with decreasing angle of incidence.

surface strains due to polishing of between 2.8 and 5.6 ppm have been measured at the edges of areas etched to a 1 μm depth.

Energy dispersive reflectometry with a high energy x-ray source can be used to characterise surface layers (crystalline or amorphous) of thickness down to the Ångstrom level. The surface roughness of polished silicon wafers can be measured to a resolution of several Å and thin surface oxide layers can be detected. Ion implanted samples with amorphous layers can also be characterised. The main advantage of energy dispersive over angle dispersive reflectometry is the much shorter data collection time.

The techniques which have been developed are powerful tools for use either in industry, or in research. X-ray diffractometry and reflectometry are complementary techniques which can be successfully applied to the surface characterisation of semiconductor materials.

Appendix

Elastic constants for silicon.

The components of elastic strain and stress in a cubic, anisotropic crystal are related by a set of six equations with three independent constants (Nye, 1957).

$$\begin{bmatrix} \sigma_1 \\ \sigma_2 \\ \sigma_3 \\ \sigma_4 \\ \sigma_5 \\ \sigma_6 \end{bmatrix} = \begin{bmatrix} C_{11} & C_{12} & C_{12} & 0 & 0 & 0 \\ C_{12} & C_{11} & C_{12} & 0 & 0 & 0 \\ C_{12} & C_{12} & C_{11} & 0 & 0 & 0 \\ 0 & 0 & 0 & C_{44} & 0 & 0 \\ 0 & 0 & 0 & 0 & C_{44} & 0 \\ 0 & 0 & 0 & 0 & 0 & C_{44} \end{bmatrix} \begin{bmatrix} \varepsilon_1 \\ \varepsilon_2 \\ \varepsilon_3 \\ \varepsilon_4 \\ \varepsilon_5 \\ \varepsilon_6 \end{bmatrix}$$

where σ is stress, ε is strain and C is the elastic constant of proportionality.

Elastic constants for silicon at 25°C and ambient pressure, from the EMIS review of properties of silicon (1988) are

$$C_{11} = 165.64 \quad \text{GN/m}^2$$
$$C_{12} = 63.94 \quad \text{GN/m}^2$$
$$C_{44} = 79.51 \quad \text{GN/m}^2$$

The error in these values is 0.02%.

References.

Afanas'ev, A.M., Aleksandrov, P.A., Imamov, R.M., Lomov, A.A., Zavyalova, A.A., "Diffraction scattering at angles far from the Bragg angle and the structure of thin subsurface layers.", Acta Cryst., A **40**, 352-355, (1984).

Afanas'ev, A.M., Aleksandrov, P.A., Fanchenko, S.S., Chaplanov, V.A., Yakimov, S.S., "Asymptotic Bragg diffraction. Single-crystal surface-adjoining-layer structure analysis.", Acta Cryst. A **42**, 116-122, (1986).

Aleksandrov, P.A., Afanas'ev, A.M., Golovin, A.L., Imamov, R.M., Novikov, D.V., Stepanov, S.A., "A new method for surface analysis of crystals using x-ray diffraction under the specular reflection conditions.", J. Appl. Cryst., **18**, 27-32 (1985).

Aldred, P.J.E., Hart, M., "The electron distribution in silicon.", Proc. R. Soc. Lond. A, **332**, 223-238, 239-254, (1973).

Andrews, S.R., Cowley, R.A., "Scattering of x-rays from crystal surfaces.", J. Phys. C, **18**, 6427-6439, (1985).

Angell, J.B., Terry, S.C., Berth, P.W., "Silicon micromechanical devices.", Scientific American, 36-47, April 1983.

Auleytner, J., Bak., J., Furmanik, Z., Maciaszek, M., Saulewicz, A., "The x-ray method for the determination of damaged layer thickness of the Si crystal surface.", Kristall Technik, **15**, 301-304, (1980).

Authier, A., "Ewald waves in theory and experiment (Dynamical theory of x-ray diffraction).", in *Advances in Structure Research by Diffraction Methods.* , edited by Brill and Mason, **3**, 1-51, (1970).

Authier, A., "Contrast of images in x-ray topography.", in *Modern Diffraction and Imaging Techniques in Material Science.*, edited by Amelinckx, Gevers, Remaut and van Landuyt, North-Holland, Amsterdam, 481-520, (1970).

Badrick, A.S.T., Eldeghaidy, F., Puttick, K.E., Shahid, M.A., "Scratches on near (111) silicon slices.", J. Phys. D, **10**, 195-200, (1977).

Bartels, W.J., "Characterization of thin layers on perfect crystals with a multipurpose high resolution x-ray diffractometer.", J. Vac. Sci. Technol. B **1**, 338-345, (1983).

Bartels, W.J., Nijman, W., "X-ray double-crystal diffractometry of $Ga_{1-x}Al_xAs$ epitaxial layers.", J. Cryst. Growth, **44**, 518-525, (1978).

Bates, S., Hatton, P.D., Lucas, C.A., Ryan, T.W., Miles, S.J., Tanner, B.K., "Grazing incidence x-ray scattering studies of single quantum wells", Adv. X-ray Anal., **31**, 155-160, (1988).

Batterman, B.W., Cole, H., "Dynamical Diffraction of X-rays by Perfect Crystals.", Rev. Mod. Phys., **36**, 681-717, (1964).

Batterman, B.W., Hildebrandt, G., "X-ray Pendellösung fringes in Darwin reflection.", Acta Cryst. A **24**, 150-157, (1968).

Beaumont, J.H., Hart, M., "Multiple Bragg reflection monochromators for synchrotron radiation.", J. Phys. E, **7**, 823-829, (1974).

Bede Scientific Instruments Limited, Lindsey Park, Bowburn North Industrial estate, Bowburn, Durham.

Bilderback, D.H., Hubbard, S., "X-ray mirror reflectivities from 3.8 to 50 keV (3.3 to 0.25 Å).", Nucl. Inst. Meth., **195**, 85-89, 91-95, (1982).

Bonse, U., "X-ray picture of the field of lattice distortions around single dislocations.", in *Direct Observations of Imperfections in Crystals*., edited by Newkirk and Wernik, 431-460, Interscience, (1962).

Bonse, U., "X-ray sources.", in *Characterization of Crystal Growth Defects by X-ray Methods*., edited by Tanner and Bowen, 298-319, Plenum Press, (1980).

Bonse, U., Hart, M., "Tailless x-ray single-crystal reflection curves obtained by multiple reflection.", Appl. Phys. Lett., **7**, 238-240, (1965).

Bonse, U., Hartmann, I., "X-ray measurement of minute lattice strain in perfect silicon crystals.", Z. Krist., **156**, 265-279, (1981).

Bowen, D.K., "Synchrotron radiation.", Adv. Mat. Sci., **1**, 522-533, (1988).

Bowen, D.K., "Principles of x-ray diffraction topography", in *Applications of Synchrotron Radiation*., edited by Winick, Xian, Ye and Huang, 77-90, Gordon and Breach, London, (1988).

Bowen, D.K., "White radiation topography and dynamic experiments", in *Applications of Synchrotron Radiation*., edited by Winick, Xian, Ye and Huang, 91-107, Gordon and Breach, London, (1988).

Bowen, D.K., "High precision x-ray topography and diffractometry", in *Applications of Synchrotron Radiation*., edited by Winick, Xian, Ye and Huang, 109-121, Gordon and Breach, London, (1988).

Bowen, D.K., Davies, S.T., "The double-crystal x-ray camera at Daresbury Laboratory.", Nucl. Inst. Meth., **208**, 725-729, (1983).

Bowen, D.K., Davies, S.T., Swaminathan, S., "Assessment of multiple epilayer III-V compound semiconductors by synchrotron radiation diffractometry.", Adv. X-ray Anal., **29**, 345-352, (1986).

Bowen, D.K. and Hall, C.R., *Microscopy of Materials*., Macmillan, London, (1975).

Brown, G.T., Keir, A.M., Gibbs, M.J., Giess, J., Irvine, S.J.C., Astles, M.G., "X-ray characterisation of $Cd_xHg_{1-x}Te$ epitaxial layers grown on to GaAs substrates by MOVPE." Electrochem. Soc. Symp. Proc., **89**, 171-182, (1989).

Brühl, H.G., Pietsch, U., Lengeler, B., "Investigation of (Ga,In)(As,P) / InP single heterostructures by means of extremely asymmetrical Bragg diffraction using synchrotron radiation.", J. Appl. Cryst., **21**, 240-244, (1988).

Bubáková, R., Drahokoupil, J., Fingerland, A., "The influence of an uneven surface on the diffraction pattern of a perfect crystal.", Czech. J. Phys. B, **17**, 657-665, (1967).

Burgeat, J., Taupin, D., "Application of dynamical theory to the study of boron and phosphorus diffusion in silicon crystals.", Acta Cryst. A **24**, 99-102, (1968).

Capano, M.A., Hart, L., Bowen D.K., Gordon-Smith, D., Thomas, C.R., Halliwell, M.A.G., "Distribution of misfit dislocations in SiGe on Si measured using synchrotron radiation topography.", to be submitted to J. Cryst. Growth., (1990).

Cembali, F., Servidori, M., Zani, A., "Double-crystal x-ray diffraction analysis of low-temperature ion implanted silicon.", Solid State Electron., **28**, 933-943, (1985).

Chu, X., Tanner, B.K., "Interference peaks in double-crystal rocking curves of laser structures.", Appl. Phys. Lett., **49**, 1773-1775, (1986).

Compton, A.H. and Allison, S.K., *X-rays in Theory and Experiment.*, Van Nostrand, New York, (1935).

Cowley, R.A., Ryan, T.W., "X-ray scattering studies of thin films and surfaces: Thermal oxides on silicon.", J. Phys. D, **20**, 61-68, (1987).

Cui, S.F., Green, G.S., Tanner, B.K., "X-ray section topography of hydrogen precipitates in silicon.", Mat. Res. Soc. Symp. Proc., (1989).

Darwin, C.G., Phil. Mag., **27**, 315, 675, (1914).

Dederichs, P.H., "Diffuse scattering from defect clusters near Bragg reflections.", Phys. Rev. B, **4**, 1041-1050, (1971).

Dederichs, P.H., "The theory of diffuse x-ray scattering and its application to the study of point defects and their clusters.", J. Phys. F, **3**, 471-496, (1973).

Dudley, M., Miltat, J., Bowen, D.K., "A study of slip nucleation in Fe-3.5% Si single crystals by synchrotron radiation topography.", Phil. Mag. A, **50**, 487-504, (1984).

DuMond, J.W.M., "Theory of the use of more than two successive x-ray crystal reflections to obtain increased resolving power.", Phys. Rev., **52**, 872-883, (1937).

Eisenberger, P., Alexandropoulos, N.G., Platzman, P.M., "X-ray Brillouin scattering.", Phys. Rev. Lett., **28**, 1519-1522, (1972).

EMIS (Electronic Materials Information Service), *Properties of Silicon.*, INSPEC, The Institution of Electrical Engineers, London, (1988).

Epelboin, Y., "X-ray topographs of silicon crystals with superposed oxide film. A theoretical study by means of simulations.", J. Appl. Phys., **64**, 109-113, (1988).

Feldman, L.C., Mayer, J.W., Picraux, S.T., *Materials analysis by ion channeling.*, Academic Press, (1982).

Fewster, P.F., "Alignment of double-crystal diffractometers.", J. Appl. Cryst., **18**, 334-338, (1985).

Fewster, P.F., "A high-resolution multiple-crystal multiple-reflection diffractometer.", J. Appl. Cryst., **22**, 64-69, (1989).

Fewster, P.F., Curling, C.J., "Composition and lattice-mismatch measurement of thin semiconductor layers by x-ray diffraction.", J. Appl. Phys., **62**, 4154-4158, (1987).

Fisher, G.R., private communication, unpublished work, (1988).

Fukuhara, A., Takano, Y., "Determination of strain distributions from x-ray Bragg reflection by silicon single crystals.", Acta Cryst. A **33**, 137-142 (1977).

Gani, S.M.A., Tanner, B.K., McKenney, T.G., Hingle, H.T., Bowen, D.K., "An assessment of diamond turning for the production of silicon x-ray optical elements.", J. Appl. Cryst., **17**, 111-117, (1984).

Halliwell, M.A.G., Lyons, M.H., Hill, M.J., "The interpretation of x-ray rocking curves from III-V semiconductor device structures.", J. Crystal Growth, **68**, 523-531, (1984).

Harada, J., Kashiwagura, N., Sakata, M., Miyatake, H., "Observation of the mechanochemically polished surface of Si wafer by electron microscopy and diffuse x-ray scattering.", J. Appl. Phys., **62**, 4159-4162, (1987).

Hart, L., Bowen, D.K., Fisher, G.R. "X-ray characterisation of residual surface strains after polishing of silicon wafers.", Advances in X-ray Analysis, **33**, 55-60, (1990).

Hart, M., "Perfect crystals. A study of their structural defects.", Sci. Prog., Oxf., **56**, 429-447, (1968).

Hart, M., "Bragg reflection x-ray optics.", Rep. Prog. Phys., **34**, 435-490, (1971).

Hart, M., "Synchrotron radiation- Its application to high-speed, high-resolution x-ray diffraction topography.", J. Appl. Cryst., **8**, 436-444, (1975).

Hart, M., "Elementary dynamical theory.", in *Characterization of Crystal Growth Defects by X-ray Methods.*, edited by Tanner and Bowen, 216-263, Plenum Press, (1980).

Hart, M., "Bragg angle measurement and mapping.", J. Crystal Growth, **55**, 409-427, (1981).

Härtwig, J., "X-ray diffraction in the extremely asymmetric Bragg case.", Exper. Technik. Physik, **26**, 447-456, (1978).

Hashizume, H., Iida, A., Kohra, K., "A multiple crystal system for high strain-sensitivity x-ray topography and its applications.", Japan. J. Appl. Phys., **14**, 1433-1441, (1975).

Haubold, H.G., "Measurement of diffuse x-ray scattering between reciprocal lattice points as a new experimental method in determining interstitial structures.", J. Appl. Cryst., **8**, 175 (1975).

Hill, M.J., "X-ray double-crystal characterisation of epitaxial layers.", PhD Thesis, Durham University, (1985).

Hill, M.J., Tanner, B.K., Halliwell, M.A.G., Lyons, M.H., "Simulation of x-ray double-crystal rocking curves of multiple and inhomogeneous heteroepitaxial layers. ", J. Appl. Cryst., **18**, 446-451, (1985).

Hirsch, P.B., "Mosaic Structure.", Progress in Metal Physics, **6**, 236-339, (1956).

Holý, V., "X-ray reflection curves of crystals with randomly distributed microdefects in the Bragg case.", Acta Cryst. A **39**, 642-646, (1983).

Holý, V., "Dynamical x-ray diffraction from crystals with precipitates. I. Theory of the Bragg case.", Acta Cryst. A **40**, 675-679, (1984).

Holý, V., Gabrielyan, K.T., "Dyson and Bethe-Salpeter equations for dynamical x-ray diffraction in crystals with randomly placed defects.", Phys. Stat. Sol. (b), **140**, 39-50, (1987).

Holý, V., Kuběna, J., "X-ray reflection curves of Si crystals with microdefects in the Laue case.", Phys. Stat. Sol. (b), **141**, 35-45, (1987).

Holý, V., Kuběna, J., "Characterization of microdefects in silicon by means of x-ray reflection curves.", Phys. Stat. Sol. (b), **155**, 339-347, (1989).

Holý, V., Cummings, S., Hart, M., "High-energy double-crystal x-ray diffraction.", J. Appl. Cryst., **21**, 516-520, (1988).

Huang, K., "X-ray reflections from dilute solid solutions.", Proc. Roy. Soc., A, **190**, 102-117 (1947).

Hummel, R.E., "Differential reflectometry and its application to the study of alloys, ordering, corrosion, and surface properties.", Phys. stat. sol. (a), **76**, 11-44, (1983).

Iida, A., "Applications of x-ray triple crystal diffractometry to studies on the diffusion-induced defects in silicon crystals.", Phys. Stat. Sol. (a), **54**, 701-706, (1979).

Iida, A., Kohra, K., "Separate measurements of dynamical and kinematical x-ray diffractions from silicon crystals with a triple crystal diffractometer.", Phys. stat. sol. (a) **51**, 533-542, (1979).

International Tables for X-ray Crystallography., Kynoch Press, Birmingham, (1974).

Ishikawa, T., Kitano, T., Matsui, J., "Synchrotron plane wave x-ray topography of GaAs with a separate (+,+) monochro-collimator.", Japan. J. Appl. Phys., **24**, L968-L971, (1985).

Ishikawa, T., Kitano, T., Matsui, J., "Equi-lattice-spacing mapping x-ray topography.", J. Appl. Cryst., **20**, 344-348, (1987).

Ives, N.A., Leung, M.S., "Subsurface damage profiling system for semiconductor materials.", Rev. Sci. Instrum., **59**, 2198-2201, (1988).

James, R.W., *The Optical Principles of the Diffraction of X-rays.*, Bell, London, (1948).

James, R.W., "The dynamical theory of x-ray diffraction.", Solid State Physics, **15**, 53-220, (1963).

Jenichen, B., Köhler, R., Möhling, W., "Double crystal topography compensating for the strain in processed samples.", Phys. stat. sol. (a), **89**, 79-87, (1985).

Jenichen, B., Köhler, R., Möhling, W., "A double-crystal x-ray topographic camera applying new principles.", J. Phys. E., **21**, 1062-1066, (1988).

Johansson, S., Schweitz, J., Lagerlöf, K.P.D., "Surface defects in polished silicon studied by cross-sectional transmission electron microscopy.", J. Am. Ceram. Soc., **72**, 1136-1139, (1989).

Kashihara, Y., Kawamura, K., Kashiwagura, N., Harada, J., "Atomic displacements at surface of Si wafer (111).", Japan. J. Appl. Phys., **26**, L1029-L1031, (1987).

Kashiwagura, N., Harada, J., Ogino, M., "Characterization of mechanochemically polished (111) surface of silicon crystal by diffuse x-ray scattering.", J. Appl. Phys., **54**, 2706-2710, (1983).

Kato, N., Acta Cryst. A **36**, 763-769, 770-778, (1980).

Kavanagh, K.L., Capano, M.A., Hobbs, L.W., Barbour, J.C., Marée, P.M.J., Schaff, W., Mayer, J.W., Pettit, D., Woodall, J.M., Stroscio, J.A., Feenstra, R.M., "Asymmetries in dislocation densities, surface morphology, and strain of GaInAs/GaAs single heterolayers.", J. Appl. Phys., **64**, 4843-4852, (1988).

Kern, W., "Chemical Etching of Silicon, Germanium, Gallium Arsenide, and Gallium Phosphide.", RCA Review, **39**, 278-308, (1978).

Kiessig, H., Ann. Physik, **10**, 715-768, 769-788, (1931).

Kikuta, S., Kohra, K., Sugita, Y., "Measurements on local variations in spacing and orientation of the lattice plane of silicon single crystals by x-ray double-crystal

topography.", Japan. J. Appl. Phys. **5**, 1047-1055, (1966).

Kishino, S., Kohra, K., "Theoretical considerations on Bragg-case diffraction of x-rays at a small glancing angle.", Japan. J. Appl. Phys., **10**, 551-557, (1971).

Kitano, T., Ishikawa, T., Matsui, J., "The effect of reduction of dislocation density on the lattice distortions in undoped GaAs single crystal grown by LEC method.", Japan. J. Appl. Phys., **25**, L282-L284, (1986).

Kitano, T., Ishikawa, T., Matsui, J., Akimoto, K., Mizuki, J., Kawase, Y., "Synchrotron plane wave x-ray topography of 6 inch diameter Si crystal.", Japan. J. Appl. Phys., **26**, L108-L110, (1987).

Köhler, R., Möhling, W., "Sensitivity of plane wave topography to microdefects.", Phys. stat. sol. (a), **78**, 489-496, (1983).

Krivoglaz, M.A., *Theory of X-Ray and Thermal-Neutron Scattering by Real Crystals.*, Plenum Press, New York, (1969).

Krivoglaz, M.A., Ryaboshapka, K.P., "Theory of x-ray scattering by crystals containing screw and edge dislocations randomly distributed throughout the crystal.", Fiz. Metal. Metalloved., **15**, 18-31, (1963).

Kyutt, R.N., Petrashen, P.V., Sorokin, L.M., "Strain profiles in ion-doped silicon obtained from x-ray rocking curves.", Phys. stat. sol. (a), **60**, 381-389, (1980).

Lal, K., Bhagavannarayana, G., "A high-resolution diffuse x-ray scattering study of defects in dislocation-free silicon crystals grown by the float-zone method and comparison with Czochralski-grown crystals.", J. Appl. Cryst., **22**, 209-215, (1989).

Larson, B.C., "High-precision measurements of lattice parameter changes in neutron-irradiated copper.", J. Appl. Phys., **45**, 514-518, (1974).

Larson, B.C., Barhorst, J.F., "X-ray study of lattice strain in boron implanted laser annealed silicon.", J. Appl. Phys., **51**, 3181-3185, (1980).

Lee, J.W., Bowen, D.K., Salerno, J.P., "224 plane x-ray diffraction study of GaAs on Si wafers using a conventional double crystal diffractometer.", Mat. Res. Soc. Symp. Proc., **91**, 193-198, (1987).

Lim, G., Parrish, W., Ortiz, C., Bellotto, M., Hart, M., "Grazing incidence synchrotron x-ray diffraction method for analysing thin films.", J. Mater. Res., **2**, 471-477, (1987).

Lomov, A.A., Zaumseil, P., Winter, U., "Characterization of process-induced defects in silicon with triple-crystal diffractometry.", Acta. Cryst., A **41**, 223-227, (1985).

Lucas, C.A., Hatton, P.D., Bates, S., Ryan, T.W., Miles, S., Tanner, B.K., "Characterization of nanometre-scale epitaxial structures by grazing-incidence x-ray diffraction and specular reflectivity.", J. Appl. Phys., **63**, 1936-1941, (1988).

Lyons, M.H., Halliwell, M.A.G., "Double-crystal diffractometry of III-V semiconductor device structures.", Inst. Phys. Conf. Ser. No. **76**, 445-450, (1985).

Macrander, A.T., Dupuis, R.D., Bean, J.C., Brown, J.M., "X-ray characterization of heteroepitaxial structures with large mismatches.", in *Semiconductor-based Heterostructures: Interfacial Structure and Stability.*, 75-85, The Metallurgical Soc. (1986).

Macrander, A.T., Strege, K.E., X-ray double-crystal characterization of highly perfect InGaAs / InP grown by vapour phase epitaxy.", J. Appl. Phys., **59**, 442-446, (1986).

Marra, W.C., Eisenberger, P., Cho, A.Y., "X-ray total-external-reflection Bragg diffraction: A structural study of the GaAs-Al interface.", J. Appl. Phys., **50**, 6927-6933, (1979).

Mayer, J.W., Eriksson, L., Davies, J.A., *Ion Implantation in Semiconductors*., Academic Press, New York, (1970).

Mayo, W.E., Chaudhuri, J., Weissmann, S., "Residual strain measurements in microelectronic materials.", Non-destructive Evaluation: Application and Materials Processing, A.S.M., 129-136, (1984).

Miles, S.J., "Characterisation of very thin epitaxial layers by high resolution x-ray diffraction", PhD Thesis, Durham University, (1989).

Miles, S.J., Green, G.S., Tanner, B.K., Halliwell, M.A.G., Lyons, M.H., "Assessment of thin heteroepitaxial layers using skew angle asymmetrical x-ray double crystal diffraction.", Mat. Res. Soc. Symp. Proc., **138**, 539 (1989).

Miltat, J., "White beam synchrotron radiation topography.", in *Characterisation of Crystal Growth Defects by X-ray Methods*., 401-420, edited by Tanner and Bowen, Plenum Press, (1980).

Miltat, J., Sauvage-Simkin, M., "Synchrotron radiation imaging techniques- A review.", in *Application of X-ray Topographic Methods to Materials Science*., edited by Weissmann, Balibar and Petroff, 185-210, Plenum, (1984).

Naudon, A., Chihab, J., Goudeau, P., Mimault, J., "New apparatus for grazing x-ray reflectometry in the angle-resolved dispersive mode.", J. Appl. Cryst., **22**, 460-464, (1989).

Nye, J.F., *Physical Properties of Crystals*., Oxford, Clarendon Press, (1957)

Parratt, L.G., "Surface studies of solids by total reflection of x-rays.", Phys. Rev. **95**, 359-369, (1954).

Patel, J.R., "X-ray anomalous transmission and topography of oxygen precipitation in silicon.", J. Appl. Phys., **44**, 3903-3906, (1973).

Patel, J.R., "X-ray diffuse scattering from silicon containing oxygen clusters.", J. Appl. Cryst., **8**, 186-191, (1975).

Peisl, H., "Defect properties from x-ray scattering experiments.", J. Physique Colloque, **37**, C7 47-53, (1976).

Petersen, K.E., "Silicon as a mechanical material.", Proc. IEEE, **70**, 420-457, (1982).

Petroff, J.F., Sauvage, M., Riglet, P., Hashizume, H., "Synchrotron-radiation plane-wave topography. I. Application to misfit dislocation imaging in III-V heterojunctions.", Phil. Mag. A, **42**, 319-338, (1980).

Pinsker, Z.G., *Dynamical Scattering of X-rays in Crystals*., Springer-Verlag, Berlin (1978).

Pons, F., Megtert, S., Pivin, J.C., Pequignot, M., Mairey, D., Roques-Carmes, C., "Application of a grazing-incidence x-ray diffraction technique to the depth-resolved analysis of structural transformations due to surface treatments.", J. Appl. Cryst., **21**, 197-205, (1988).

Puttick, K.E., Shahid, M.A., "Abrasion of silicon by diamond.", Industrial Diamond Review, 228-233, July 1977.

Puttick, K.E., Shahid, M.A., Hosseini, M.M., "Size effects in abrasion of brittle materials.", J. Phys. D, **12**, 195-202, (1979).

Ravi, K.V., *Imperfections and Impurities in Semiconductor Silicon.*, Wiley-Interscience, New York, (1981).

Renninger, M., Phys. Lett. **1**, 104-106, 106-109, (1962).

Renninger, M., "Contribution to x-ray double-crystal diffraction topography.", Z. Angew. Physik, **19**, 20-33 (1965).

Robbins, H., Schwartz, B., "Chemical Etching of Silicon. I. The System HF, HNO_3, and H_2O.", J. Electrochem. Soc., **106**, 505-508, (1959).

Robinson, I.K., "Crystal truncation rods and surface roughness.", Phys. Rev. B, **33**, 3830-3836, (1986).

Rodrigues, PhD Thesis, King's College, London, (1979).

Ryan, T.W., Hatton, P.D., Bates, S., Watt, M., Sotomayor-Torres, C., Claxton, P.A., Roberts, J.S., "X-ray scattering from a single-quantum-well heterostructure.", Semicond. Sci. Technol., **2**, 241-243, (1987).

Sauvage, M., "Monochromatic synchrotron radiation topography.", in *Characterization of Crystal Growth Defects by X-Ray Methods.*, edited by Tanner and Bowen, 433-455, Plenum Press, (1980).

Schnopper, H.W., "Spectral measurements with aligned and misaligned two-crystal spectrometers.", J. Appl. Phys., **36**, 1415-1423, 1423-1430, (1965).

Schwartz, B., Robbins, H., "Chemical Etching of Silicon. IV. Etching Technology.", J. Electrochem. Soc., **123**, 1903-1909, (1976).

Schwarzchild, M.M., "Theory of the double x-ray spectrometer.",Phys. Rev., **32**, 162-171, (1928).

Segmüller, A., "Observation of x-ray interferences on thin films of amorphous silicon.", Thin Solid Films, **18**, 287-294, (1973).

Servidori, M., "Characterisation of lattice damage in ion implanted silicon by multiple crystal x-ray diffraction.", Nucl. Inst. Meth., B, **19/20**, 443-449, (1987).

Smith, S.T., "Machining of silicon with high speed miniature diamond cutters.", J. Phys. D, **23**, 607-616, (1990).

Speriosu, V.S., "Kinematical x-ray diffraction in non-uniform crystalline films: Strain and damage distributions in ion-implanted garnets.", J. Appl. Phys., **52**, 6094-6103, (1981).

Speriosu, V.S., Paine, B.M., Nicolet, M.A., Glass, H.L., "X-ray rocking curve study of Si-implanted GaAs, Si and Ge.", Appl. Phys. Lett., **40**, 604-606, (1982).

Speriosu, V.S., Nicolet, M.A., Tandon, J.L., Yeh, Y.C.M., "Interfacial strain in $Al_x Ga_{1-x} As$ layers on GaAs.", J. Appl. Phys., **57**, 1377-1379, (1985).

Stacy, W.T., Janssen, M.M., "X-ray Pendellösung in garnet epitaxial layers.", J. Cryst. Growth, **27**, 282-286, (1974).

Stevenson, A.W., Wilkins, S.W., Harada, J., Kashiwagura, N., Ohshima, K., Sakata, M., "Triple-crystal diffraction studies on ion-implanted and other silicon crystals using a synchrotron source.", Acta Cryst. A **44**, 828-833, (1988).

Stickler, R., Booker, G.R., "Surface damage on abraded silicon specimens.", Phil. Mag., **8**, 859-876, (1963).

Stokes, A.R., Wilson, A.J.C., "The diffraction of x-rays by distorted crystal aggregates.", Proc. Phys. Soc., **56**, 174-181, (1944).

Takagi, S., "Dynamical theory of diffraction applicable to crystals with any kind of small distortion.", Acta Cryst., **15**, 1311-1312, (1962).

Takagi, S., "A dynamical theory of diffraction for a distorted crystal.", J. Phys. Soc. Japan, **26**, 1239-1253, (1969).

Tan, T.Y., Gösele, U., "Point defects, diffusion processes and swirl defect formation in silicon.", Appl. Phys. A, **37**, 1-17 (1985).

Tanner, B.K., *X-ray Diffraction Topography*., Pergamon Press, Oxford, (1976).

Tanner, B.K., Barnett, S.J., Hill, M.J., "X-ray double crystal topographic studies of III-V compounds.", Microscopy of Semiconductor Materials, Oxford, Inst. Phys. Conf. Ser., (1985).

Tanner, B.K. and Bowen, D.K., (editors), *Characterization of Crystal Growth Defects by X-ray Methods*., Plenum Press, New York, (1980).

Tanner, B.K., Chu Xi, Bowen, D.K., "A new technique for high speed x-ray double-crystal rocking-curve analysis.", Mater. Res. Soc. Symp. Proc., **69**, 191-196, (1986).

Tanner, B.K., Halliwell, M.A.G., "Interference structures in double-crystal x-ray rocking curves from very thin multiple epitaxial layers.", Semicond. Sci. Technol., **3**, 967-972, (1988).

Tanner, B.K., Hill, M.J., "X-ray double-crystal diffractometry of multiple and very thin heteroepitaxial layers.", Adv. X-ray. Anal., **29**, 337-343, (1986).

Tanner, B.K., Hill, M.J., "Double axis x-ray diffractometry at glancing angles.", J. Phys. D, **19**, L229-L235, (1986).

Tapfer, L., Ospelt, M., von Känel, H., "Monolayer resolution by means of x-ray interference in semiconductor heterostructures.", J. Appl. Phys., **67**, 1298, (1990).

Tapfer, L., Ploog, K., "Improved assessment of structural properties of $Al_xGa_{1-x}As$ / GaAs heterostructures and superlattices by double-crystal x-ray diffraction.", Phys. Rev. B, **33**, 5565-5574, (1986).

Taupin, D., "Dynamical theory of x-ray diffraction for deformed crystals.", Bull. Soc. Fr. Min. Crist., **87**, 469-511, (1964).

Thomas, J.E., Baldwin, T.O., Dederichs, P.H., "Diffuse x-ray scattering in fast-neutron-irradiated copper crystals.", Phys. Rev. B, **3**, 1167-1173, (1971).

Toney, M.F., Huang, T.C., Brennan, S., Rek, Z., "X-ray depth profiling of iron oxide thin films.", J. Mater. Res., **3**, 351-356, (1988).

Trinkhaus, H., "On determination of the double-force tensor of point defects in cubic crystals by diffuse x-ray scattering.", Phys. stat. sol. (b), **51**, 307-319, (1972).

Tuck, B., "The Chemical Polishing of Semiconductors.", J. Mat. Sci., **10**, 321-339, (1975).

Vineyard, G.H., "Grazing-incidence diffraction and the distorted-wave approximation for the study of surfaces.", Phys. Rev. B, **26**, 4146-4159, (1982).

Warren, B.E., Averbach, B.L., "The effect of cold-work distortion on x-ray patterns.", J. Appl. Phys., **21**, 595-599, (1950).

Wilkens, M., "The determination of density and distribution of dislocations in deformed single crystals from broadened x-ray diffraction profiles.", Phys. stat. sol. (a), **2**, 359-370, (1970).

Yoshimura, J., "Influence of the vertical divergence of beams in the x-ray double-crystal arrangement.", J. Appl. Cryst., **17**, 426-434, (1984).

Zachariasen, W.H., *Theory of X-ray Diffraction in Crystals*., Wiley, New York, (1945).

Zaumseil, P., Winter, U., "Triple crystal diffractometer investigations of silicon crystals with different collimator-analyser arrangements.", Phys. stat. sol. (a), **70**, 497-505, (1982).

Zaumseil, P., Winter, U., Cembali, F., Servidori, M., Sourek, Z., "Determination of dislocation loop size and density in ion implanted and annealed silicon by simulation of triple crystal x-ray rocking curves.", Phys. stat. sol. (a), **100**, 95-104, (1987).

Ziegler, J.F. (editor), *Ion Implantation Science and Technlogy*., Academic Press, Inc., (1988).

TITLE

Surface Characterisation of Semiconductor Materials.

AUTHOR

Linda Hart

INSTITUTION and DATE

University of Warwick

June 1990